

ABSTRACT

Enabling and Directing Real-Time Cognitive Radar Transmitter Optimization

Austin S. Egbert, Ph.D.

Mentor: Charles P. Baylis, Ph.D.

As the available wireless spectrum grows more crowded with increased usage from high bandwidth telecommunications applications, it becomes infeasible for many other users of wireless spectrum to continue operating with static, inflexible methods. Among these users are radar systems, which have historically been allocated large sections of bandwidth. In order to adapt and coexist with new technology in a dynamically managed environment, next generation radars must be able to adjust their spectral configuration in real time. The research presented in this dissertation provides a framework that can be used for determining transmission constraints over both spatial direction and signal frequency. While existing research has demonstrated how to optimize radar transmitters using adjustable amplifier matching networks, such optimizations have not been able to complete quickly enough for use in real-time adaptation. To accelerate these optimizations, this dissertation presents a faster method for evaluating the performance of transmit amplifiers using a software-defined radio (SDR) and a load-pull extrapolation method using deep learning image completion techniques. Additionally, the accelerated optimization technique has been adapted for use

with the pulse-to-pulse waveform agility paradigm of cognitive radars. Finally, the impact on Doppler detection accuracy of modifying the radar transmit chain during a coherent radar processing interval is analyzed, along with techniques for correcting the resulting distortions.

Enabling and Directing Real-Time Cognitive Radar Transmitter Optimization

by

Austin S. Egbert, B.S.E.C.E.

A Dissertation

Approved by the Department of Electrical and Computer Engineering

Kwang Y. Lee, Ph.D., Chairperson

Submitted to the Graduate Faculty of
Baylor University in Partial Fulfillment of the
Requirements for the Degree
of
Doctor of Philosophy

Approved by the Dissertation Committee

Charles P. Baylis II, Ph.D., Chairperson

Robert J. Marks II, Ph.D.

Scott Koziol, Ph.D.

Enrique Blair, Ph.D.

Jill Klentzman, Ph.D.

Accepted by the Graduate School
December 2021

J. Larry Lyon, Ph.D., Dean

Copyright © 2021 by Austin S. Egbert

All rights reserved

TABLE OF CONTENTS

LIST OF FIGURES	vii
LIST OF TABLES	xi
ACKNOWLEDGMENTS	xii
ATTRIBUTIONS	xiii
CHAPTER ONE	1
Introduction.....	1
CHAPTER TWO	7
Dynamic Approach for Determining Spatial-Spectral Transmission Constraints.....	7
2.1 <i>Motivation and Background</i>	7
2.2 <i>Original Framework</i>	9
2.3 <i>Spatial Dimension</i>	11
2.4 <i>Projection to Fewer Dimensions</i>	12
2.5 <i>Waveform Optimization Results</i>	14
CHAPTER THREE	28
Real-Time RF Device Performance Evaluation using Software-Defined Radios	28
3.1 <i>Motivation</i>	28
3.2 <i>Review of the State-of-the Art</i>	29
3.3 <i>SDR-based RF Performance Measurements</i>	30
3.4 <i>Pulsed Waveform TX/RX Synchronization</i>	35
3.5 <i>Load-Pull Demonstration</i>	35
CHAPTER FOUR.....	40
Real-Time Independent Optimization of Cognitive Radar Transmit Amplifier.....	40
4.1 <i>Cognitive Radar Overview and Problem Description</i>	40
4.2 <i>Software-Defined Radar (SDRadar) Overview</i>	43
4.3 <i>Adapting Gradient Methods to Cognitive Radar</i>	48
4.4 <i>Algorithm Description</i>	56
4.5 <i>Experimental Results</i>	75

CHAPTER FIVE	82
Partial Load-Pull Extrapolation via Deep Image Completion	82
5.1 Motivation	82
5.2 Extrapolation Method	85
5.3 Simulated Linear Load-Pull Extrapolation	91
5.4 Measured Non-Linear Device Load-Pull Extrapolation	95
CHAPTER SIX.....	108
Effects of Impedance Tuning on Range-Doppler Processing.....	108
6.1 Background.....	108
6.2 Proposed Theory of Adaptive Component Doppler Shifts.....	110
6.3 Range-Doppler Processing During Impedance Tuning	111
6.4 Direct Measurements of Impedance Tuning Doppler Shift	114
6.5 Distortion Analysis and Correction Process	120
CHAPTER SEVEN	130
Conclusions and Future Work	130
BIBLIOGRAPHY.....	135

LIST OF FIGURES

Figure 2.1. Example Latham-style dynamic spectral mask	11
Figure 2.2. Example of a generated spatial-spectral constraint map	13
Figure 2.3. Geographic scenario for spatial and spectral regulation simulation.....	16
Figure 2.4. Generated spectral mask dictating radar waveform spectral requirements	17
Figure 2.5. Ambiguity function (template and realized) for a range radar response profile.....	19
Figure 2.6. Range ambiguity function result for ideal 30° beam at 60°	21
Figure 2.7. Spectral mask for results of Figure 2.6.....	21
Figure 2.8. Range ambiguity function result for ideal 30° beam at 0°	22
Figure 2.9. Spectral mask for results of Figure 2.8.....	23
Figure 2.10. Depressions ambiguity function result for ideal 30° beam at 135°	24
Figure 2.11. Spectral mask for results of Figure 2.11.....	24
Figure 2.12. Simulated gain pattern for helix antenna.....	25
Figure 2.13. Range ambiguity function result for helix antenna at 45°	26
Figure 2.14. Spectral mask for results of Figure 2.13.....	26
Figure 2.15. Range ambiguity function result for helix antenna in relaxed environment at 45°	27
Figure 2.16. Spectral mask for results of Figure 2.15.....	27
Figure 3.1. Flowchart for calculation of average RF output power with SDR.....	32
Figure 3.2. Flowchart for calculation of spectral mask compliance with SDR	34
Figure 3.3. Flowchart for latency calibration in pulse measurement systems	36

Figure 3.4. Image of second-generation evanescent-mode cavity tuner.....	37
Figure 3.5. Output power contours for standard and custom load-pull systems.....	38
Figure 3.6. Spectral mask compliance contours for custom load-pull system.....	39
Figure 4.1. SDRadar system architecture block diagram	46
Figure 4.2. Deployable SDRadar system block diagram.....	47
Figure 4.3. SDRadar system block diagram for circuit optimization experiments.....	47
Figure 4.4. Comparison of average performance and average gradient optimization objectives	52
Figure 4.5. Illustration of gradient search candidate selection process	59
Figure 4.6. Waterfall plot of RFI pattern with optimal measurement window of 20	61
Figure 4.7. Search end locations with RFI pattern of Figure 4.6.....	62
Figure 4.8. Final search powers with RFI pattern of Figure 4.6.....	63
Figure 4.9. Search durations with RFI pattern of Figure 4.6	64
Figure 4.10. Correlation of measurement utilization ratio and search time with RFI pattern of Figure 4.6.....	66
Figure 4.11. Waterfall plot of RFI pattern with optimal measurement window of 40	67
Figure 4.12. Correlation of measurement utilization ratio and search time with RFI pattern of Figure 4.11.....	67
Figure 4.13. Flowchart of the dynamic measurement window selection process	70
Figure 4.14. Correlation of earth mover’s distance and output power improvement.....	74
Figure 4.15. Probability distribution of time interval between RFI pattern transitions.....	76
Figure 4.16. SDRadar transmit frequency utilization over time.....	78
Figure 4.17. Percent increase in maximum detectable range from circuit optimization ...	79
Figure 4.18. Normalized earth mover’s distance during circuit optimization	80
Figure 4.19. Dynamic measurement window during circuit optimization	81

Figure 5.1. Illustration of partial load-pull extrapolation objective.....	83
Figure 5.2. Illustration of the function of the generator and discriminator networks.....	86
Figure 5.3. Illustration of the image completion search process	86
Figure 5.4. WGAN-GP critic network topology network.....	88
Figure 5.5. WGAP-GP generator network topology network	88
Figure 5.6. Linear load-pull extrapolation results with 0.5 mask	92
Figure 5.7. Linear load-pull extrapolation results with 0.3 mask	93
Figure 5.8. Linear load-pull extrapolation results with 0.1 mask	94
Figure 5.9. Generic process diagram for circuit optimization using load-pull extrapolation	96
Figure 5.10. Extrapolation circuit optimization results at 2.0 GHz.....	98
Figure 5.11. Extrapolation circuit optimization results at 2.7 GHz.....	99
Figure 5.12. Extrapolation circuit optimization results at 4.0 GHz.....	100
Figure 5.13. Power loss and search duration for extrapolation circuit optimization	101
Figure 5.14. Early convergence of extrapolation circuit optimization	103
Figure 5.15. Comparison of elapsed times for the load-pull extrapolation search and gradient algorithm.....	104
Figure 5.16. Power error statistics for non-linear load-pull extrapolations	105
Figure 5.17. Load impedance error statistics for non-linear load-pull extrapolations.....	106
Figure 6.1. First-generation evanescent-mode cavity tuner.....	112
Figure 6.2. Power-added efficiency contours of MWT-173 device	113
Figure 6.3. Doppler and range detection distortions while tuning.....	114
Figure 6.4. Tuner transmission phase profile while tuning	115
Figure 6.5. Estimated instantaneous Doppler shift while tuning.....	116

Figure 6.6. Down-conversion frequency shift measurement block diagram	117
Figure 6.7. Time-domain frequency shift measurements while tuning	119
Figure 6.8. Comparison of frequency-domain and time-domain Doppler shift measurements.....	119
Figure 6.9. Propagation error due to linear phase shifts	124
Figure 6.10. Matched filter responses for varying constant phase offsets.....	125
Figure 6.11. Comparison of matched filter phase response with tuner phase profile.....	127
Figure 6.12. Fourier transform of matched filter phase response and tuner phase profile	128
Figure 6.13. Per-pulse matched filter target detection results	129

LIST OF TABLES

Table 3.1. Comparison of Standard and SDR-Based Load-Pull System Measurements...	39
Table 4.1. Gradient Search Parameters.....	59
Table 4.2. Dynamic Measurement Window Parameters	69
Table 4.3. Step Size Convergence Parameters.....	72
Table 4.4. SDRadar EMD Test Waveform Characteristics	73
Table 4.5. 0.1 EMD Threshold Characteristics.....	74
Table 5.1. Dataset S-Parameter Generation Bounds.....	89
Table 5.2. Linear Load-Pull Extrapolation Performance – Predicted Peak Statistics	94
Table 5.3. Non-Linear Load-Pull Extrapolation Performance – Predicted Peak Statistics.....	107

ACKNOWLEDGMENTS

I would like to sincerely thank my advisor Dr. Charles Baylis as well as Dr. Robert Marks for their guidance and advice over the past several years, as well as my family for their continued love and support. In addition, I would like to thank the former and current students in our research group for providing the foundation upon which much of this work rests and for continuing to build upon these developments in the future. Many thanks to Purdue University for developing the impedance tuner technologies that enabled many of the contributions in this work. I would also like to thank the many friends and family who have graciously endured my long-winded ramblings while working through difficult problems, especially my parents Clark and Ann Egbert, my sister Caylee Egbert, and my friends Zach and Luci Hays and Jackson Henry. Finally, I would also like to thank and acknowledge Lawrence Cohen, John Clark, Anthony Martone, Kelly Sherbondy, and Ben Kirk for their assistance, collaboration, and guidance on much of this work, as well as the many other students, researchers, and developers who contributed to the SDRadar platform in Chapter Four.

Please note that this dissertation includes work funded by the National Science Foundation (Grant No. ECCS-1343316) and the Army Research Laboratory (Grant No. W911NF-16-2-0054). The views and opinions expressed do not necessarily represent the opinions of the U.S. Government.

ATTRIBUTIONS

This work would not be possible without the collaboration of many of my fellow colleagues. You will find references to the primary published works represented in this dissertation at the start of each chapter. Detailed information regarding the contributions of others for each of these works is as follows:

The underlying work for Chapter Two was coauthored with Casey Latham, Charles Baylis, and Robert J. Marks. Casey Latham provided the initial dynamic spectral mask method that was adapted for spatial-spectral use in this chapter and an illustration of a mask generated with his method (Figure 2.1). Drs. Baylis and Marks provided general advisement and guidance throughout the work.

The underlying work for Chapter Three was coauthored with Benjamin H. Kirk, Charles Baylis, Anthony Martone, and Robert J. Marks. Dr. Kirk offered guidance with the use of the software-defined radio platform used by this work. Drs. Baylis, Martone, and Marks provided general advisement and guidance throughout the work.

The underlying works for Chapter Four were coauthored with Adam Goad, Charles Baylis, Benjamin H. Kirk, Robert J. Marks, and Anthony Martone. Adam Goad provided assistance in the application of the earth mover's distance and key insights into the difference between averaging techniques demonstrated in Figure 4.4. Dr. Kirk provided the SDRadar platform used in this work and contributed figures outlining the structure and operation of the platform. Drs. Baylis, Marks, and Martone provided general advisement and guidance throughout the work.

The underlying work for Chapter Five was coauthored with Anthony Martone, Charles Baylis, and Robert J. Marks. Drs. Baylis, Marks, and Martone provided general advisement and guidance throughout the work.

The underlying work for Chapter Six was coauthored with Kyle Gallagher, Benjamin H. Kirk, Mark Kozy, Anthony Martone, Charles Baylis, and Robert J. Marks. Mark Kozy and Drs. Gallagher and Kirk assisted in the collection and processing of the range-Doppler measurements in Figure 6.3. Drs. Martone, Baylis, and Marks provided general advisement and guidance throughout the work.

CHAPTER ONE

Introduction

In 2009, then-Federal Communications Commission (FCC) chairman Julius Genachowski stated, “I believe that the biggest threat to the future of mobile in America is the looming spectrum crisis” [1]. The crisis he foresaw was an inability to provide enough spectrum for future wireless telecommunications applications and systems, such as for fifth-generation wireless (5G) technology. At the time, mobile data usage was expected to grow from 6 PB/mo in 2008 to 400 PB/mo in 2013. More recently, Ericsson has estimated that global mobile data usage will reach 226 EB/mo in 2026 [2]. To address this lack of spectrum availability, the National Broadband Plan of 2010 directed the FCC to auction off several regions of spectrum that had been previously allocated to other uses [3], and proposals of new reallocations are under continued development [4]. While these auctions have helped to alleviate spectral pressure, the auction and reallocation process takes several years to complete, limiting this solution’s usefulness to situations where the need for spectral shuffling can be recognized in advance.

It is important to note that spectral auctions alone do little to provide a long-term solution to spectral congestion, as recognized by the President’s Council of Advisors on Science and Technology (PCAST) in 2012 [5]. While PCAST argued that auctions of federal spectrum were unsustainable due to cost, time, and disruption of government missions, the issues do not stop there. In fact, as long as intermittent or infrequent spectrum applications (including various military and aerospace systems) exist, long-

term, static allocations are fundamentally incompatible with the need for high spectrum utilization (ratio of occupied spectrum to total spectrum). Under the traditional approach for spectrum allocation, spectrum utilization studies reveal that high-population areas such as New York City, Chicago, or Dublin often only utilize 13-17% of the available spectrum at peak times [6-8]. The utilization within a given band often reflects the nature of the applications assigned to that band. For instance, McHenry [6] shows that TV bands have utilization up to 77%, cellular bands have utilization up to 46%, and various radar or aerospace application bands have utilization between 0.2 and 5%. Clearly, not all wireless applications are equal in terms of spectrum utilization. However, traditional application-based spectrum allocation, which assigns specific portions of the spectrum for specific uses, ignores this utilization disparity. As a result, some bands face overcrowding while others are severely underused by comparison.

A more efficient approach for spectrum management involves the use of dynamically allocating spectrum resources “on the fly” based on the users’ needs within a given geographic region. Various approaches for spectrum management exist in the literature, addressing the benefits and challenges faced in alternate arrangements [9-13]. Some of these approaches have begun to see real-world application under the Citizens Broadband Radio Service (CBRS) [14], with additional spectrum sharing options currently under consideration as part of America’s Mid Band Initiative [15]. With the introduction of phased array antenna technology, additional control over transmission direction enables additional dimensions of spectral control, further aiding the potential for efficient use of spectrum resources [16-20]. Chapter Two of this dissertation presents an approach for determining acceptable transmission power densities in both frequency and

spatial angle for use in a dynamic spectrum allocation system, given knowledge of the current spectral environment.

In order to take full advantage of the flexibility afforded by a dynamic allocation system, devices must be able to reconfigure themselves for efficient operation in the available bands in a timely manner. For high-power applications such as radar, this reconfiguration requires optimization of the system's transmit chain for optimal performance at the selected frequency. Previous work has been done to develop optimization algorithms [21-24] for radar transmit amplifiers using adjustable load impedance tuners [25-26], but the measurement techniques used fall short of real-time operation, with individual measurement sets requiring multiple seconds to complete. Active load-pull systems have demonstrated significant improvements in tuning time [27], but they are not practical for use in deployed, high-power systems. Meanwhile, software-defined radios (SDRs) have been used to demonstrate some measurement techniques [28-29]. Chapter Three demonstrates how SDRs can be used to greatly accelerate the measurement process for some additional common amplifier performance metrics and, when combined with the impedance tuner of [26], vastly reduce the time required for complete device load-pulls compared to traditional passive load-pull systems.

Even with these improvements, high-power, mechanically actuated impedance tuners are not able to operate quickly enough to provide optimal performance for cognitive radars, which can craft unique radar pulses designed to fit in the existing spectral environment. Typically, a radar's pulse repetition interval (PRI) may range from 10 μ s to 100 μ s, while the fast impedance tuner of [26] takes 40 ms to 100 ms per tuning

operation. As a result, such tuners can only be used to optimize the average performance of such radars over the course of many pulses. Chapter Four of this dissertation demonstrates how existing circuit optimization techniques can be adapted for average performance and how the optimal averaging length can be determined on-the-fly. The end result is a band-agile, cognitive radar that is able to intelligently alter its transmit amplifier's load impedance in real-time to maximize its average transmit power during active spectral adaptation, enabling detection of farther radar targets.

One disadvantage of the implemented approach is that the majority of transmit configurations (combination of transmit frequency, bandwidth, and waveform) considered during optimization must be evaluated at multiple impedances during each search iteration. While the optimization adjusts the measurement period to better meet this condition, the vast majority of measurements will likely provide duplicate information. As many transmit configurations exhibit similar impacts on the transmit amplifier (such that they could be treated as identical during the search process), it is likely possible to group several such configurations, greatly reducing the number of measurements required during optimization. However, it is difficult obtain enough information during the optimization process to act on this assumption and correctly group like configurations. Given the regular nature of amplifier performance contours on the Smith Chart, it is possible to use partial knowledge of the circuit performance associated with a given transmit configuration to extrapolate a more complete understanding that can be used to find transmit configurations with identical performance characteristics. Chapter Five of this dissertation introduces how deep learning and generative adversarial networks (GAN) can be used to apply image completion to partial load-pull information.

These completion techniques may be able to improve the responsiveness of future cognitive radar circuit optimization efforts, and they can be used on their own as a circuit optimization algorithm as well as to jump-start initialization of other algorithms or accelerate load-pull measurements by greatly reducing the number of evaluated impedances required to produce accurate load-pull contours, with as few as six measurements being required in many cases.

It is important to note that although cognitive radars can adapt their transmissions for their environment, such reconfiguration conflicts with many radar applications that utilize multiple transmit/receive cycles using the same transmit waveform (coherent processing). Under traditional coherent radar signal processing, any changes made to the transmit characteristics of the radar will negatively impact the ability to accurately discern information about the sensed environment, as the assumptions underlying coherent processing techniques are violated by the changing transmission. Kirk [30] has examined the impacts of varying waveform definitions on the quality of range-Doppler processing and introduced correction methods for dealing with the resulting distortions. Similarly, Chapter Six of this dissertation examines the effects of varying load impedance on range-Doppler processing and presents methods to mitigate these effects. Chapter 7 provides some conclusions, re-summarizing the contributions of this work and recommendations for future research.

Altogether, this dissertation presents significant progress in enabling and directing real-time cognitive radar optimization. As discussed, direction of the cognitive radar itself can be improved through the presented dynamic spatial-spectral constraint analysis method. Likewise, optimization is enabled by the introduction of faster measurement

techniques using SDRs and deep image completion, an analysis of and mitigation process for distortions in radar processing caused by adaptive transmit hardware, and new methods for improving the average radar performance during live spectrum adaptation, culminating in the first demonstration of real-time circuit optimization of a cognitive radar transmit amplifier.

CHAPTER TWO

Dynamic Approach for Determining Spatial-Spectral Transmission Constraints

The work presented in this chapter has been published in: [31] A. Egbert, C. Latham, C. Baylis, and R. J. Marks, "Multi-dimensional coexistence: Using a spatial-spectral mask for spectrum sharing in directional radar and communication," *2018 Texas Symposium on Wireless and Microwave Circuits and Systems (WMCS)*, 2018, pp. 1-6, doi: 10.1109/WMCaS.2018.8400641. © 2018, IEEE.

2.1 Motivation and Background

As discussed in Chapter One, traditional, static spectrum management techniques are ill-suited for several types of spectrum applications [6-8], and many dynamic spectrum allocation techniques have been proposed. Zhao has summarized these alternative methods within three categories: dynamic exclusive use, open sharing models, and hierarchical access models [9]. Under dynamic exclusive use, traditional, static allocation is expanded to permit spectrum owners to sell and trade their exclusive spectrum rights with other users as desired, especially on a much shorter basis and along much more finely divided spatial areas than with traditional allocation. At the opposite extreme, open sharing models build upon the success of unlicensed bands with WiFi, Bluetooth, etc., permitting sharing among many spectral users within a band without the need for exclusive licensing. Finally, the hierarchical access model bridges the prior categories, allowing primary users of a band to obtain spectral rights while also allowing other secondary users to transmit in-band in such a way to limit interference to primary users.

As an example, the FCC's Citizens Broadband Radio Service (CBRS) has implemented a 3-tier hierarchical access model within the 3.55-3.7 GHz band [14]. Within this system, incumbent users (i.e., pre-existing band occupants) retain full rights to the band at all times. However, other users may also operate within the band, guided by a central Spectrum Access System (SAS). The SAS collects geolocation information of non-incumbent users to within ± 50 m horizontal and ± 3 m vertical and assigns spectrum usage on a dynamic basis, avoiding interference to incumbent users. These other users are required to adapt their spectral usage within 60 s of commands provided by the SAS. Additionally, non-incumbent users are permitted to purchase priority access for a band, for which they will receive preferential allocation from the SAS over other non-incumbent, general users.

Prior to the development of the CBRS and its concept of an SAS, Latham demonstrated an adaptive technique for spectrum allocation that, similar to an SAS, generates dynamic spectral transmission limits given knowledge of location and interference power limits of neighboring receivers [13]. However, such an approach goes beyond the aims of an SAS (which still attempts to reserve the use of specific frequencies for specific users in a geographic area) by permitting overlapping access to bands by various users under the condition that these users do not interfere with each other.

In dealing with the increasingly crowded spectral environment, any additional degrees of freedom for operation that enable finer control over transmission at the device level also enable more precise management from a spectral allocation standpoint, allowing the available spectrum to be used more efficiently. To this end, Drozd discusses the concept of a "transmission hypercube" consisting of various dimensions of

transmission freedom that can be used for spectrum allocation, including the traditional management dimensions of time and frequency, as well as less developed dimensions of direction, code, and polarization [32].

With the introduction of electrically steerable multiple-element phased array antenna systems, the ability to control the direction of transmission is becoming more common. Specifically, such systems can be used at the millimeter-wave transmission frequencies of fifth-generation (5G) wireless systems, allowing 5G devices to share available spectral resources more efficiently [16]. Given this flexibility, a dynamic approach based on the real-time position of devices within a given band can be used to fully utilize the additional freedom afforded by spatial transmission control. Such an approach has previously been expected for use by 5G systems in both microwave and millimeter-wave bands [9]. This chapter presents a method that allows for the generation of specific transmission constraints based on the current spectral environment and desired transmission signal or spatial pattern.

2.2 Original Framework

The work in this chapter extends the dynamic spectral mask generation established by Latham [13] to also include the spatial domain. Latham's original framework utilizes information gathered about other spectrum users within the surrounding environment to generate a spectral mask for transmission, assuming an omnidirectional radiation pattern. The required information includes the operating frequencies of the devices, the maximum interfering spectral power density that can be tolerated by each device, and the transmission path loss between each device and the

transmitter being regulated. For a simplified model (ignoring effects such as multi-path transmission), the Friis transmission equation

$$P_r = \frac{G_t G_r \lambda^2}{(4\pi R)^2} P_t \quad (2.1)$$

can be used to determine the power received by a specific device (P_r) when the transmitter radiates power P_t , where G_t and G_r are the transmitter and device receiver antenna gains, λ is the receiver's operating wavelength, and R is the distance from the transmitter to the receiver. In [13], both G_t and G_r were assumed to be unity, indicating ideal omnidirectional antennas at both the transmitting and receiving devices. In practice, real antenna gains can be included if known.

Rearranging (2.1) to solve for P_t and assuming omnidirectional antennas provides the relation

$$P_t = \frac{(4\pi R)^2}{\lambda^2} P_r, \quad (2.2)$$

where P_t now represents the amount of power that can be transmitted before power P_r is available at the receiving device. Given the desirable maximum allowable interference power density for a device as P_r , the maximum allowable transmit power is P_t . This maximum allowable transmit power can then be used to generate a spectral mask specific to the current environment at a given point in time. Continued monitoring of the environment enables the creation of a dynamic, time-varying spectral mask. In [13], the spectral mask is generated from the constraints produced by (2.2) by searching for the widest frequency gap between two constraints for use as the center of the mask and then linearly connecting the remaining constraints. An example of a spectral mask generated by this approach is shown in Figure 2.1.

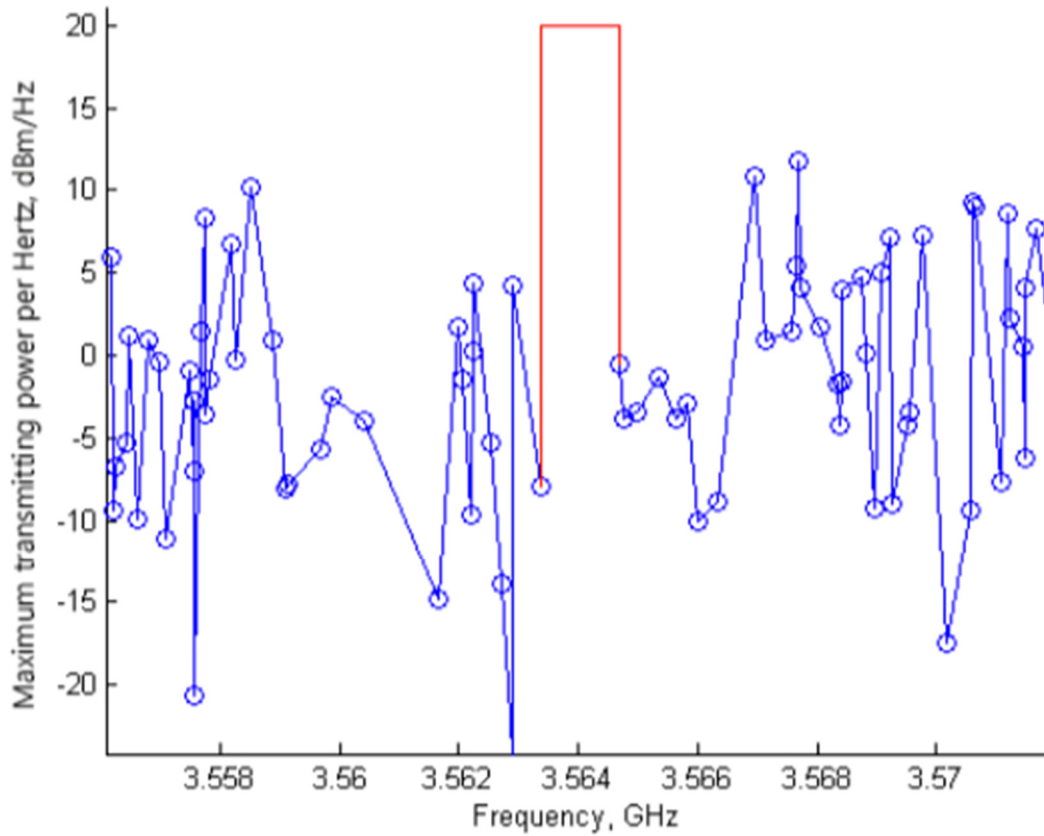


Figure 2.1. Example dynamic spectral mask generated using the approach of Latham [13]. © 2016, IEEE.

2.3 Spatial Dimension

The original framework introduced in [13] can be extended to include spatial degrees of freedom by modifying the definition of the maximum allowable interference power P_r for each device. Beginning with (2.1), maximum transmitted power constraints can be determined for each receiver in a known environment in $\frac{W}{Hz}$. Note that as these are constraints are spectral power densities, they are not able to dictate spatial constraints. However, a joint spatial-spectral density can be generated for a planar environment by assuming point receivers and an omnidirectional antenna transmission pattern ($G_t = 1$ for

all directions), dividing the result by 2π to produce a spatial angular density. This results in a maximum allowable interference power density for each device in $\frac{W}{Hz \cdot rad}$. The set of all of these device constraints is indexed as $P_r(f, R, \phi)$, where f is the receiver operating frequency, R is the distance between the receiver and constrained transmitter, and ϕ is the azimuthal direction of the receiving device from the transmitter with respect to a predetermined reference direction.

Based on these device-dictated constraints, a spatial-spectral constraint map can be generated by choosing the most restrictive constraint for each frequency in each direction. In other words, if two devices exist in the environment at the same direction and frequency, the device with the most severe constraint will be chosen. The resulting constraint map is

$$P_t(f, \phi) = \min_{0 \leq R \leq \infty} \left[P_r(f, R, \phi) \frac{(4\pi R)^2}{2\pi G_r \lambda^2} \right], \quad (2.3)$$

where $P_t(f, \phi)$ describes the allowable transmitted spatial-spectral power density in each direction, ϕ , at each frequency, f . An example of this constraint map structure is shown in Figure 2.2. A system is considered in compliance with this constraint map as long as the transmission power density at each frequency and direction is lower than the constraint map. For frequency or direction combinations where no constraint exists, no limit is placed on transmit power density.

2.4 Projection to Fewer Dimensions

Often, either the transmission pattern or transmission waveform spectrum are predetermined and fixed. In these cases, the spatial-spectral constraint map can be projected onto solely the spatial or spectral domain.

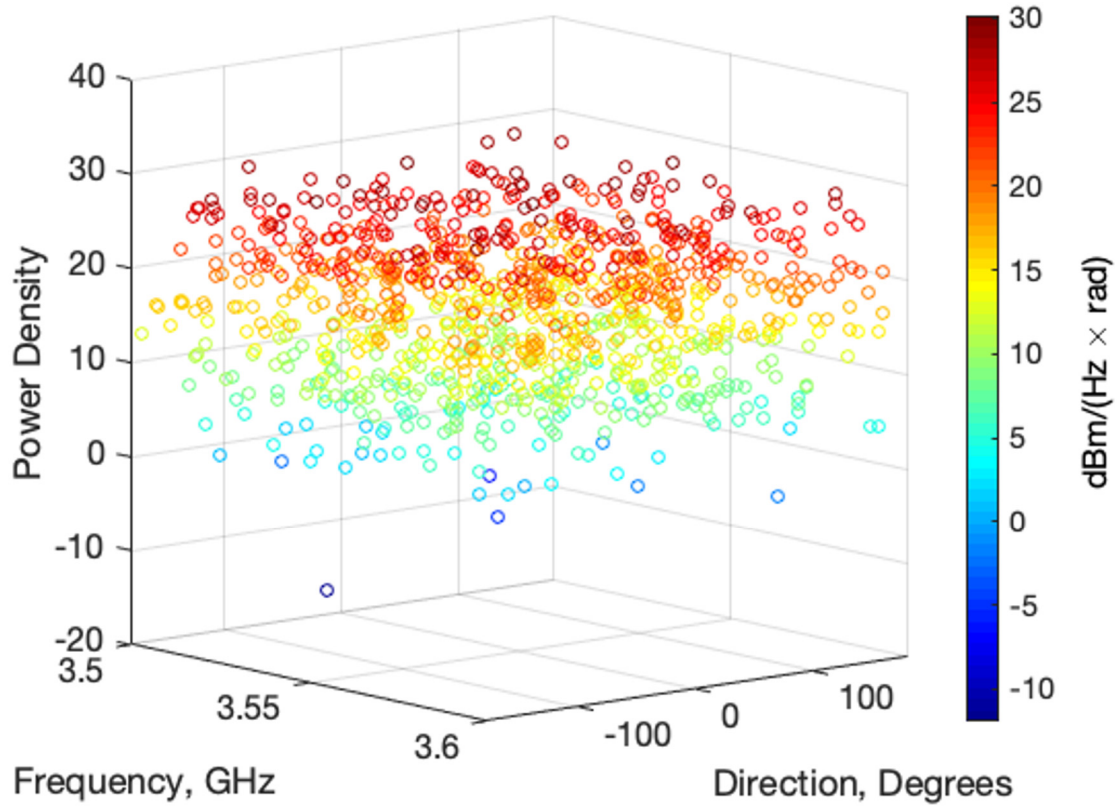


Figure 2.2. Example of a generated spatial-spectral constraint map for 1000 devices within 1km of a hypothetical beamforming radar system. © 2018, IEEE.

2.4.1 Spectral Constraint Map

Given a known system transmission pattern, the gain of the pattern in each direction can be applied to the existing constraint map as a weight on the constraint. The resulting spectral constraint map is

$$S_t(f) = \int_0^{2\pi} \min_{0 \leq \phi \leq 2\pi} \left[P_t(f, \phi) \frac{1}{G_t(\phi)} \right] d\phi, \quad (2.4)$$

where $S_t(f)$ is the permissible transmission spectral power density at a given frequency in $\frac{W}{Hz}$, and $G_t(\phi)$ is the present arbitrary antenna transmission pattern.

Note that the loss of a dimension of freedom necessitates choosing the most restrictive constraint in each direction for a given frequency. However, by accounting for the actual transmission gain in each direction, this projection results in a precise allocation of transmittable power, allowing for more freedom than what is offered by traditional spectrum allocation, which does not vary with transmission direction.

2.4.2 Spatial Constraint Map

Just as for the spectral constraint map, a known signal spectrum can be applied as a weight on the existing constraint map. In this case, the resulting constraint map is

$$Q_t(\phi) = \int_{f_1}^{f_2} \min_{f_1 \leq f \leq f_2} \left[P_t(f, \phi) \frac{1}{|X(f)|} \right] df, \quad (2.5)$$

where $Q_t(\phi)$ is the permissible transmission spatial power density in a given direction in $\frac{W}{rad}$, the signal bandwidth is limited to $f_1 \leq f \leq f_2$, and $|X(f)|$ is the normalized signal spectrum (signal spectrum divided by the chosen maximum transmit power density, both in $\frac{W}{Hz}$). This results in the same loss of a dimension as the spectral mask, but also allows the spatial transmission pattern to be tuned to provide the best flexibility given the fixed signal spectrum.

2.5 Waveform Optimization Results

To demonstrate the capabilities of the spatial-spectral constraint map, the Alternating Projections-based ambiguity function waveform optimization algorithm of Eustice [33] was adapted to use a spectral mask generated by the method described in the previous section. This algorithm can generate a radar waveform with the desired ambiguity function and spectral and energy constraints by continually projecting the signal onto the classes of signals meeting each objective until convergence is reached.

Two different scenarios are considered: one with an ideal, uniform, steerable antenna, and another with a simulated helix antenna transmission pattern. Unless otherwise noted, the presented results use the same sample environment as described in the next section.

2.5.1 Simulation Environment

Figure 2.3 shows a spatial simulation scenario, constructed in MATLAB, that considers a single beamforming radar and 1000 receiving devices operating between 3.5 and 3.6 GHz. The transmitter is assumed to be at the origin of the plane. If the locations of the receivers are known, as well as the frequency, antenna gain, and maximum tolerable received interference spectral power density for each receiver, then the transmitter can adjust its configuration to ensure that it does not interfere with any of the receivers. Such information might be provided by a wireless network carrier or a SAS as used by CBRS. For this experiment, the receivers and transmitter are both assumed to be stationary, although velocity could easily be added to the receivers in the simulation if known. Finally, the receiver antenna gains are assumed to be unity.

Additionally, the simulated radar has a maximum transmission spectral power density of $60 \frac{dBm}{Hz}$ and uses 20 MHz of reconfigurable bandwidth within the 3.5 to 3.6 GHz range, which has been chosen as it includes frequencies that have been allocated for sharing between radar and wireless communications. Note that these system parameters have been chosen arbitrarily for demonstration purposes and could be substituted with those of an existing system. The spatial-spectral constraint map generated for this environment is shown in Figure 2.2.

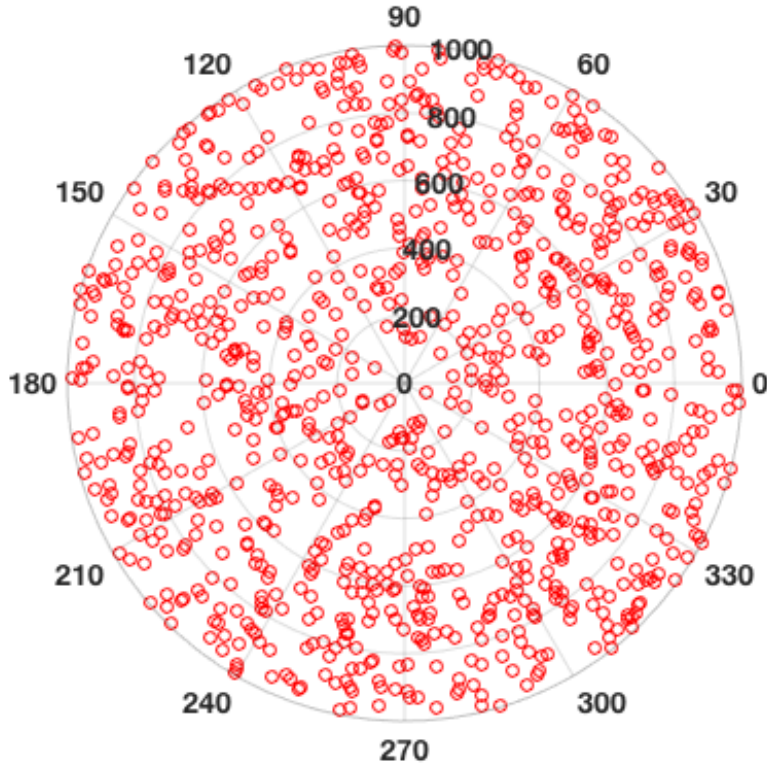


Figure 2.3. Geographic scenario for spatial and spectral regulation simulation with 1000 handset devices (radial dimension in meters, angular dimension in degrees). © 2018, IEEE.

2.5.2 Spectral Mask Generation

Because the radar in this simulation does not have complete freedom to alter its transmission pattern, the spatial-spectral constraint map from (2.3) is used to generate a spectral constraint map through the application of the system’s transmission pattern, $G_t(\phi)$. The resulting spectral constraint map can be transformed into a more traditional mask over a continuous domain by allowing for the maximum transmission power density where no constraint exists. Additionally, each receiver in this scenario is assumed to have a 1 MHz operating bandwidth in which interference can be received. As the radar operates over 20 MHz within a 100 MHz band, the widest gap in frequency between two

constraints is chosen to center the radar waveform. Other methods could also be used to choose the spectrum, such as optimizing the overall total transmit power available within the band, which can be more useful in extremely crowded scenarios. This process results in a notched spectral mask of the type shown in Figure 2.4. This notched approach results in more relaxed constraints in instances with a sparse environment due to the limited frequency range that a given device constraint is able to dictate, compared to the approach of Latham [13], as demonstrated in Figure 2.1.

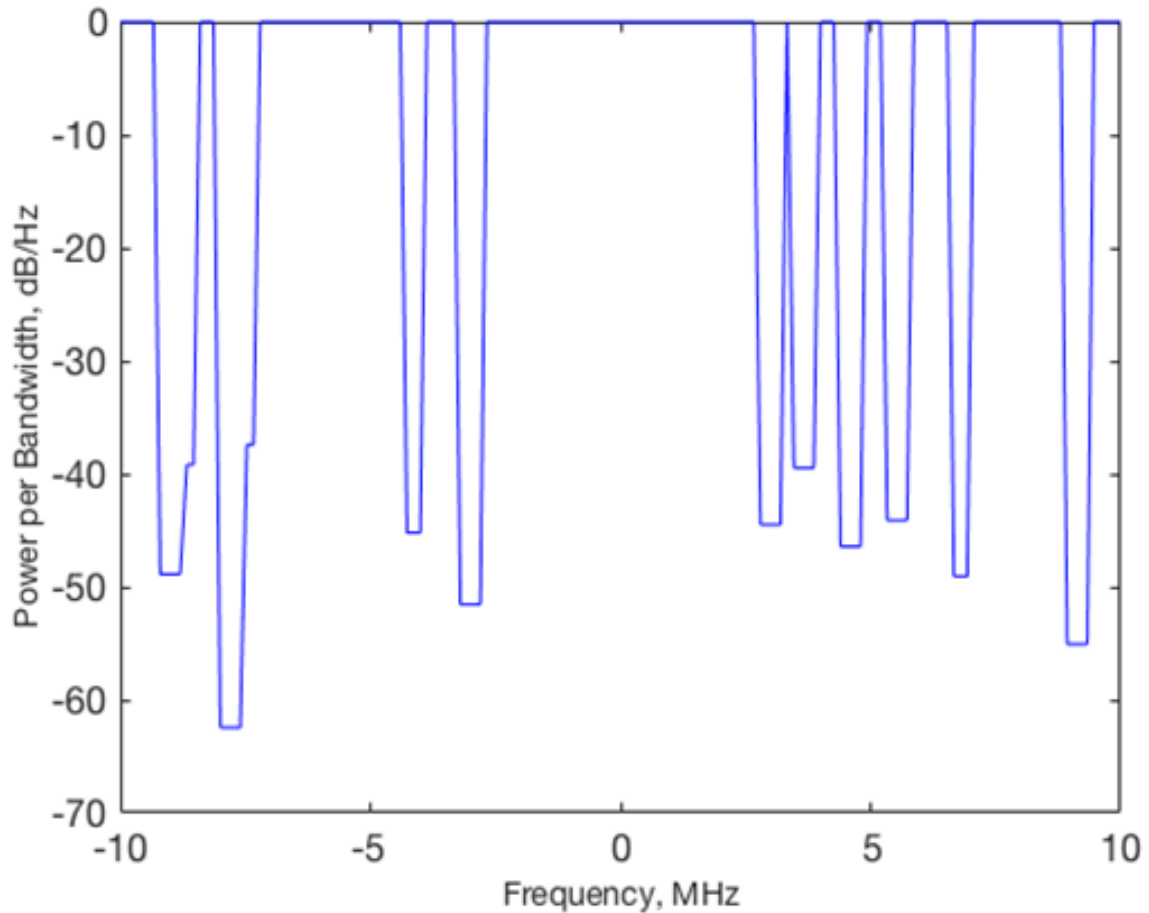


Figure 2.4. Generated spectral mask dictating radar waveform spectral requirements. © 2018, IEEE.

2.5.3 Radar Waveform Optimization

Using the generated spectral mask, a transmit waveform is synthesized that will attempt to provide desired ambiguity function properties, as dictated by an ambiguity template, while not violating the generated mask. The ambiguity function of a given signal $x(t)$ describes the output of the radar correlation process with time delay τ and Doppler shift u , and is denoted as

$$\chi_x(\tau, u) = \int_{-\infty}^{\infty} x(t)x^*(t - \tau)e^{-j2\pi ut} dt. \quad (2.6) [33]$$

An example of an ambiguity function is shown on the right side of Figure 2.5. The shape of a signal's ambiguity function indicates the range and Doppler resolution that can be achieved when detecting a target. For example, a radar intended primarily for range detection would benefit from an ambiguity function with a narrow ridge running along the Doppler axis at $\tau = 0$, allowing multiple objects located at similar distances from the radar to be discernible as separate, distinct targets. The range radar ambiguity template used for this work is shown on the left side of Figure 2.5.

Given a template of the desired ambiguity function $M(\tau, u)$ and required spectral mask $S_t(f)$, the process described in [33] can be used to produce a signal meeting both conditions. This approach projects the current signal iteration onto signals that meet the given ambiguity template and signals that meet the spectral mask in an alternating fashion. These projections are performed respectively via the following:

$$\chi_{x,n+1}(\tau, u) = \begin{cases} \chi_{x,n}(\tau, u) \frac{M(\tau, u)}{|\chi_{x,n}(\tau, u)|}, & |\chi_{x,n}(\tau, u)| > M(\tau, u) \\ \chi_{x,n}(\tau, u), & |\chi_{x,n}(\tau, u)| \leq M(\tau, u) \end{cases} \quad (2.7)$$

$$X_{n+1}(f) = \begin{cases} S_t(f), & X_n(f) > S_t(f) \\ X_n(f), & X_n(f) \leq S_t(f) \end{cases} \quad (2.8)$$

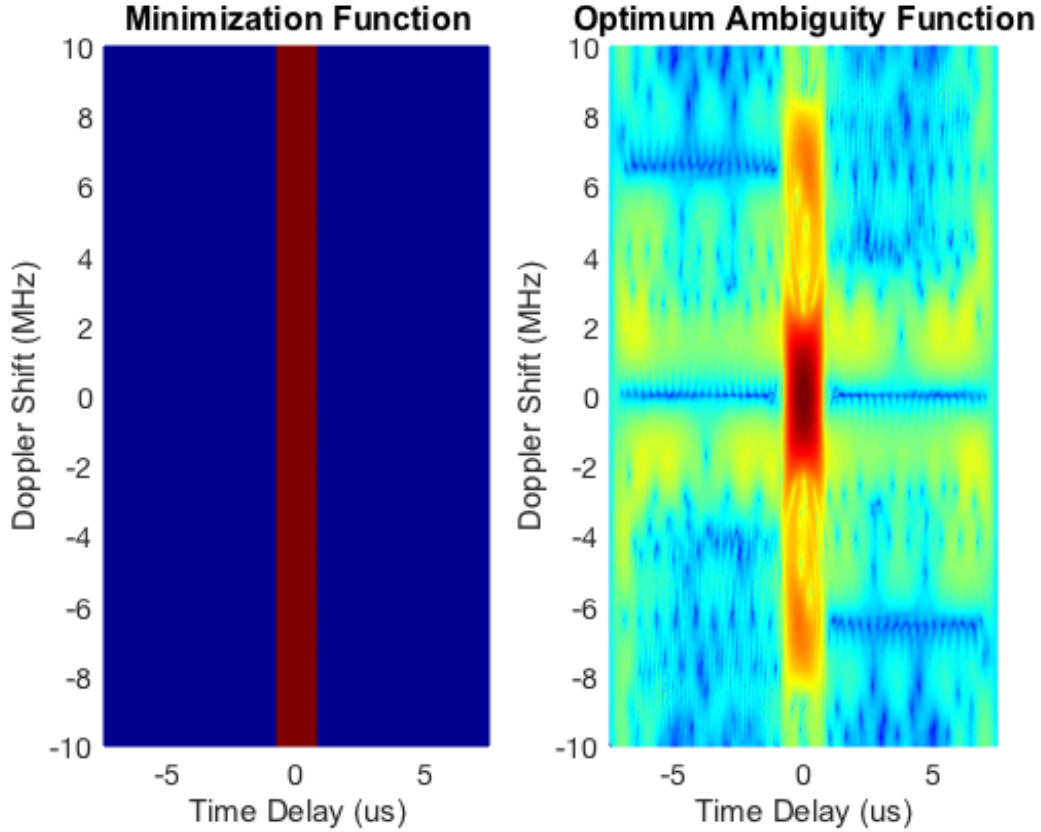


Figure 2.5. Ambiguity function template for range radar (left) and realized ambiguity function (right). © 2018, IEEE.

In order to use these projections, the signal must be converted to and from the different domains dictated by the respective constraint sets. For the first projection, inversion of the current 2D ambiguity function iteration $\chi_{x,n}(\tau, u)$ to a corresponding 1D time-domain waveform $x_n(t)$ is performed via an approach using weighted combinations of 1D projections of $\chi_{x,n}(\tau, u)$, described in [33]. For the second projection, the time-domain waveform $x_n(t)$ and its spectrum $X_n(f)$ are Fourier transform pairs, $x_n(t) \Leftrightarrow X_n(f)$.

Repeated iterations of these projections will eventually converge to a fixed signal (in the event both constraints are able to be met simultaneously), or a cycle between two

signals that meet one constraint, but not the other (referred to as a limit cycle). In this scenario, the ambiguity template projection is treated as a goal, while the spectral mask is treated as a requirement. Because of this, the chosen waveform will always be selected immediately after a spectral mask projection to ensure spectral compliance, possibly sacrificing some performance with respect to the ambiguity template.

2.5.4 Results - Ideal Antenna

An ideal, steerable transmission antenna that radiates coherently within an adjustable beam width in the azimuthal plane is considered. The gain of this antenna is

$$G_t(\phi) = \begin{cases} \frac{2\pi}{|\phi_2 - \phi_1|}, & \phi_1 \leq \phi \leq \phi_2 \\ 0, & \text{otherwise} \end{cases} \quad (2.9)$$

where ϕ_1 and ϕ_2 are the angular edges of the steerable transmission beam in radians. For this experiment, the antenna beamwidth is chosen to be 30° , and the transmission direction is swept over the environment of Figure 2.3.

Figure 2.6 shows the results of the waveform optimization when the antenna beam is centered at 60° . Figure 2.7 shows the generated spectral mask and the corresponding synthesized signal spectral power density. These figures indicate the optimization can achieve the desired ambiguity function while avoiding interference with any of the surrounding devices in the environment.

As the beam is steered, devices will enter and exit the beam path, which changes the permitted interference power per bandwidth at each transmission frequency and reshapes the spectral mask. If the radar waveform optimization is run continuously, the waveform can be updated as the beam is steered to different directions.

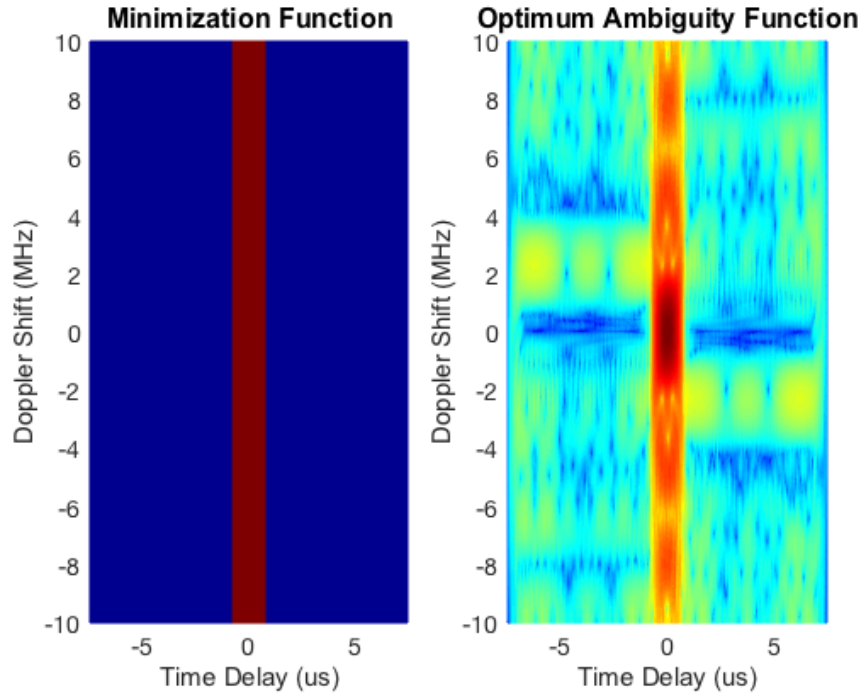


Figure 2.6. Ambiguity function minimization template (left) and resulting ambiguity function (right) for the optimized waveform for a uniform beam centered at 60° with a beamwidth of 30° . © 2018, IEEE.

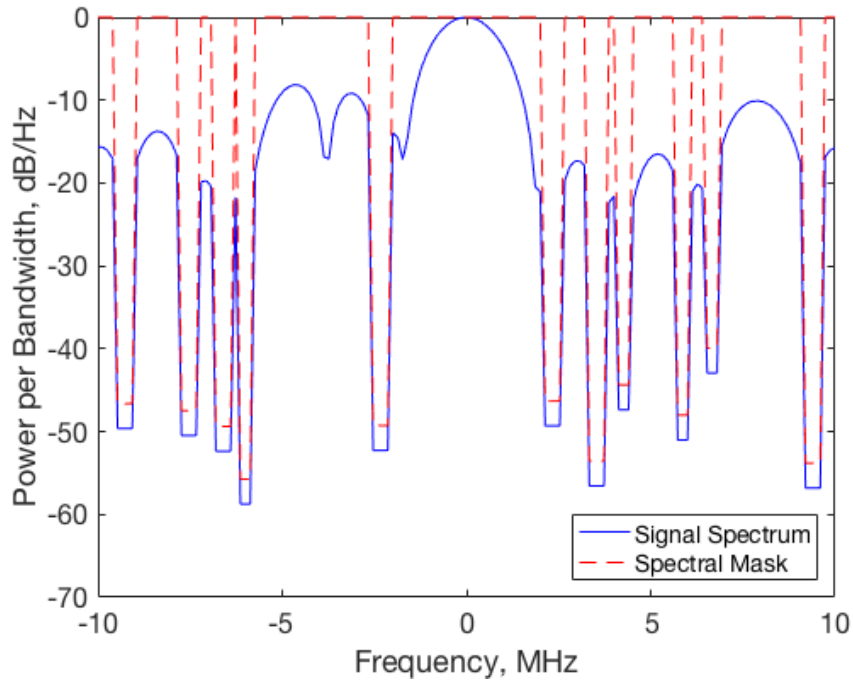


Figure 2.7. Spectral mask and resulting optimized waveform centered at 3.47 GHz for a uniform beam centered at 60° with a beamwidth of 30° . © 2018, IEEE.

Figure 2.8 shows the range radar minimization template, along with the optimized ambiguity function for a beam centered at 0° and a beamwidth of 30° . Figure 2.9 shows the resulting optimized waveform's spectrum with the new spectral mask. The waveform optimization compensates to still create a waveform with the widest possible bandwidth, while meeting the interference-imposed requirements on the transmit spectrum.

Other ambiguity minimization templates may also be used with the generated mask. Figures 2.10 and 2.11 show the optimization results for an arbitrary “depressions” ambiguity template (named for the circular depressions imposed on the template) with the transmission beam steered to 135° .

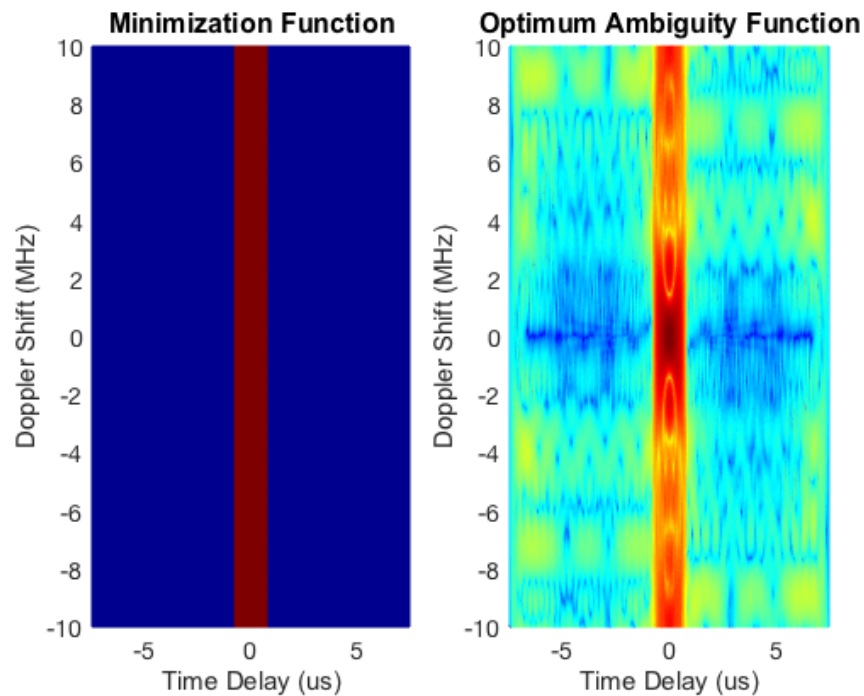


Figure 2.8. Ambiguity function minimization template (left) and resulting ambiguity function for the second range radar optimization, centered at 0° . © 2018, IEEE.

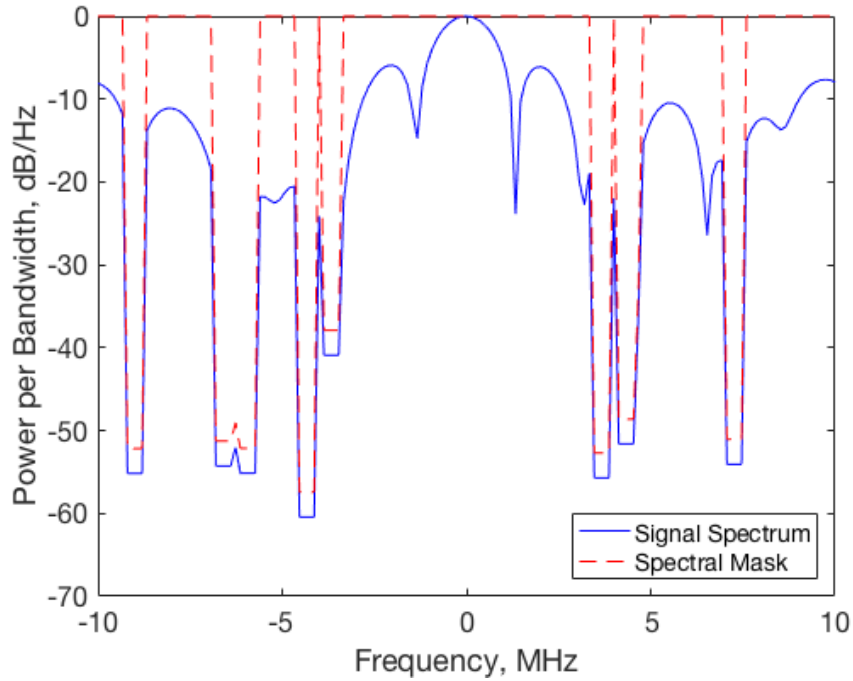


Figure 2.9. Spectral mask and resulting optimized waveform centered at 3.52 GHz for a beam centered at 0° with a beamwidth of 30° . © 2018, IEEE.

2.5.5 Results - Helix Antenna

A more realistic, simulated helix antenna is considered, in lieu of the ideal beam of the previous section. The simulated antenna gain is shown in Figure 2.12 with maximum transmission gain of 13.2 dBi. This antenna is used for additional range radar optimizations, with the results shown in Figures 2.13 and 2.14.

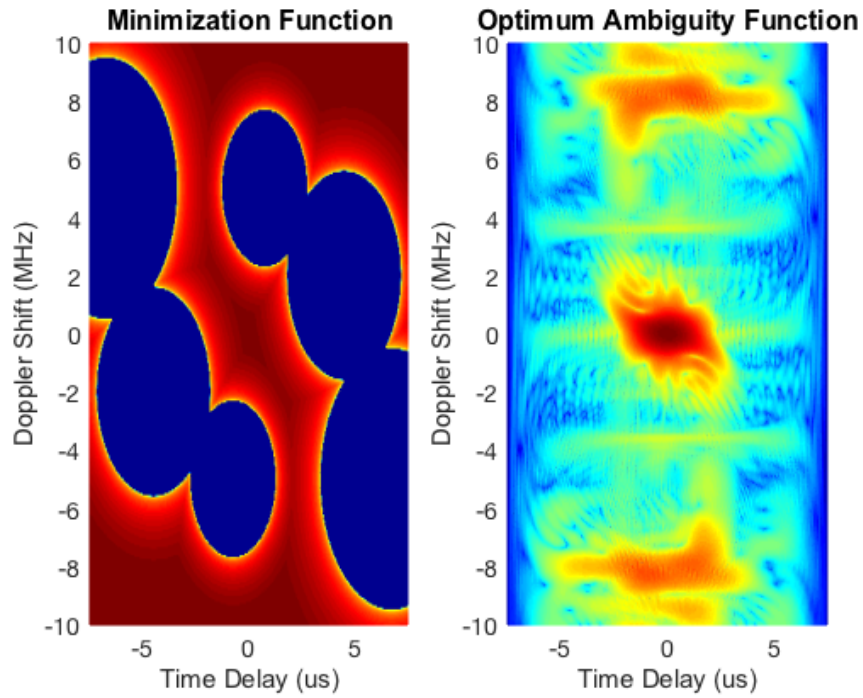


Figure 2.10. Depressions ambiguity function minimization template (left) and resulting ambiguity function for the alternating-projections optimization, centered at 135° . © 2018, IEEE.

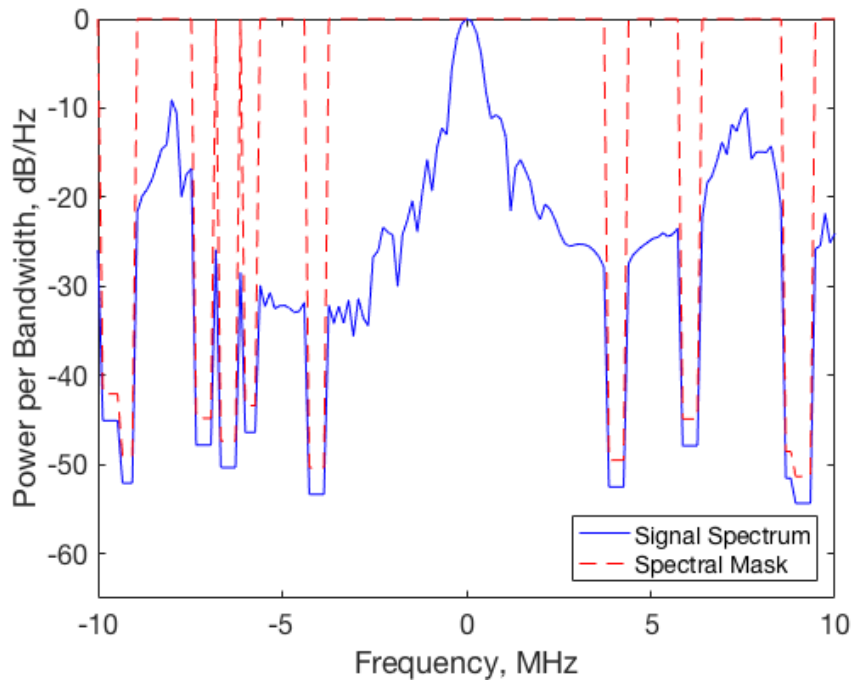


Figure 2.11. Spectral mask and resulting optimized depressions waveform centered at 3.53 GHz for a beam centered at 135° with a beamwidth of 30° . © 2018, IEEE.

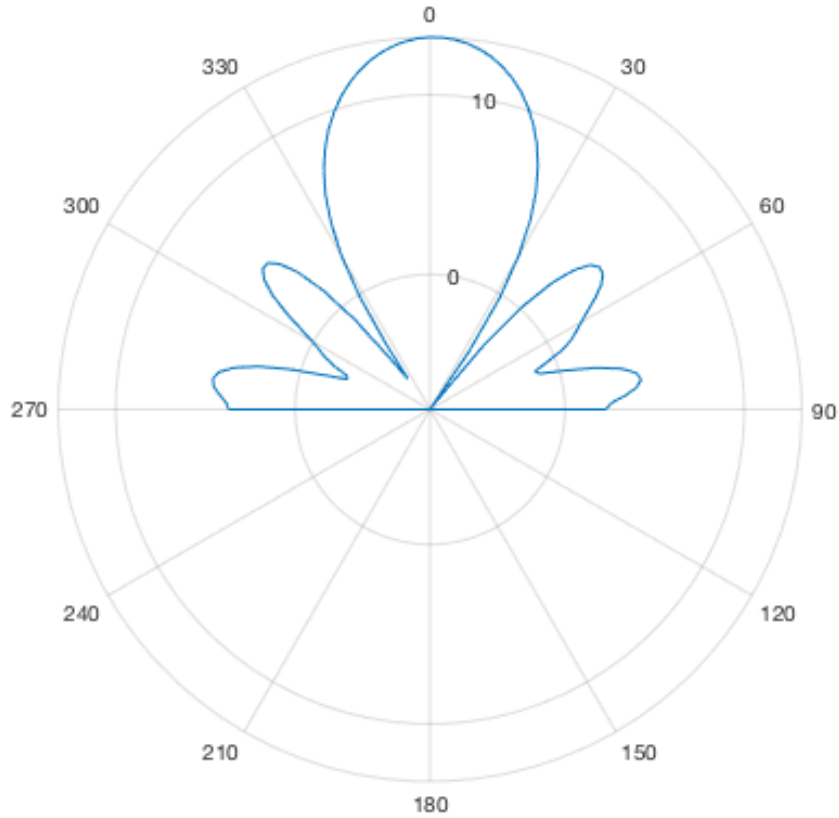


Figure 2.12. Simulated helix antenna gain pattern in azimuth plane (direction measured in degrees), with maximum gain of 13.2 dBi. © 2018, IEEE.

In this case, the fixed helix antenna pattern results in too strict of an environment to properly generate a range radar. This is exacerbated by choosing the widest constraint gap for the center frequency as it results in a large center peak, which results in a rather narrow-band waveform that is more optimized for Doppler resolution. Choosing a center frequency that allows for a more uniform distribution of bandwidth would improve the range performance of the algorithm. Additionally, if fewer constraining devices are in the surrounding area, or if the transmission pattern is adjusted to mitigate the effect on closer or more sensitive receivers, a more acceptable ambiguity result can be achieved. Results with only 300 receiver devices are shown in Figures 2.15 and 2.16. This optimization provides outcomes more similar to those achieved by the uniform beam.

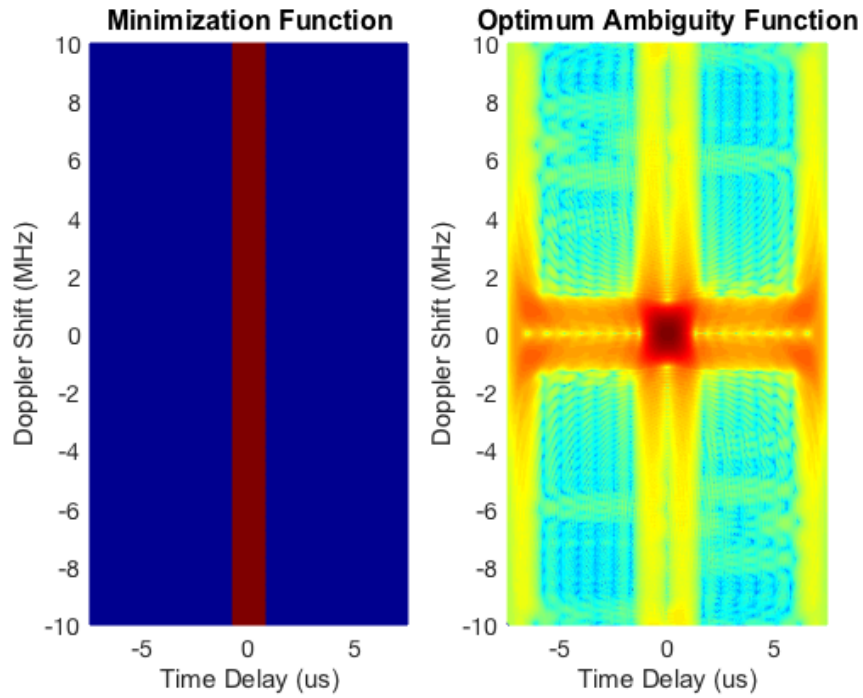


Figure 2.13. Range radar ambiguity function minimization template (left) and resulting ambiguity function for the alternating projections optimization with the helix antenna pattern turned to face 45°. © 2018, IEEE.

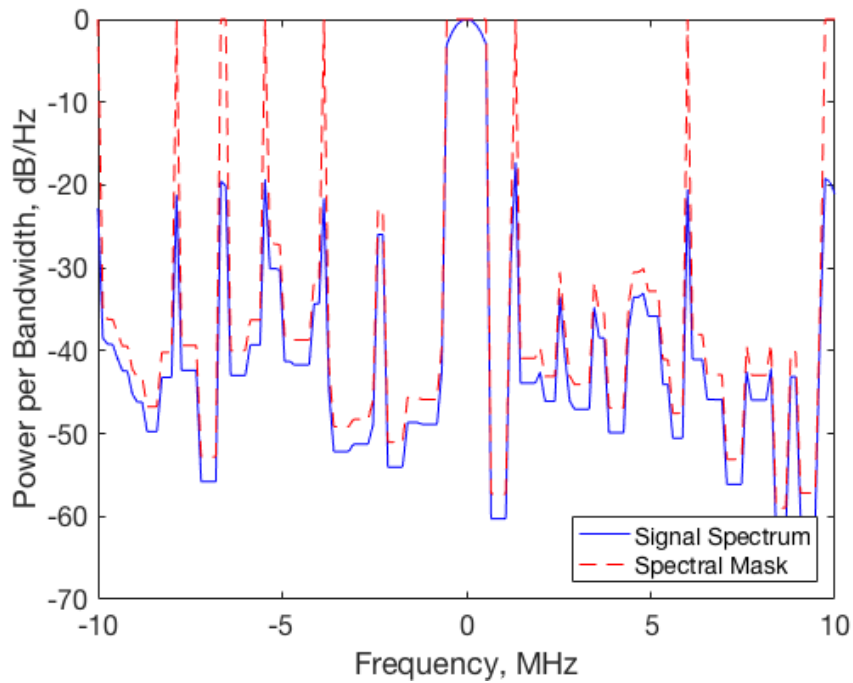


Figure 2.14. Spectral mask and resulting optimized range radar waveform centered at 3.57 GHz for the helix antenna pattern centered at 45°. © 2018, IEEE.

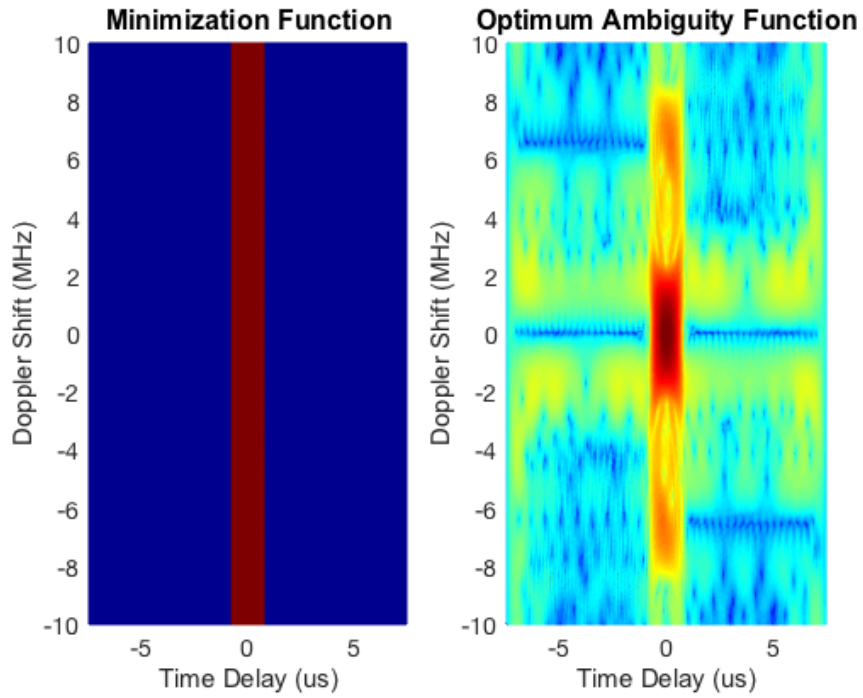


Figure 2.15. Range radar ambiguity function minimization template (left) and resulting ambiguity function for the alternating- projections optimization in a 300 receiver environment with the helix antenna pattern turned to face 45° . © 2018, IEEE.

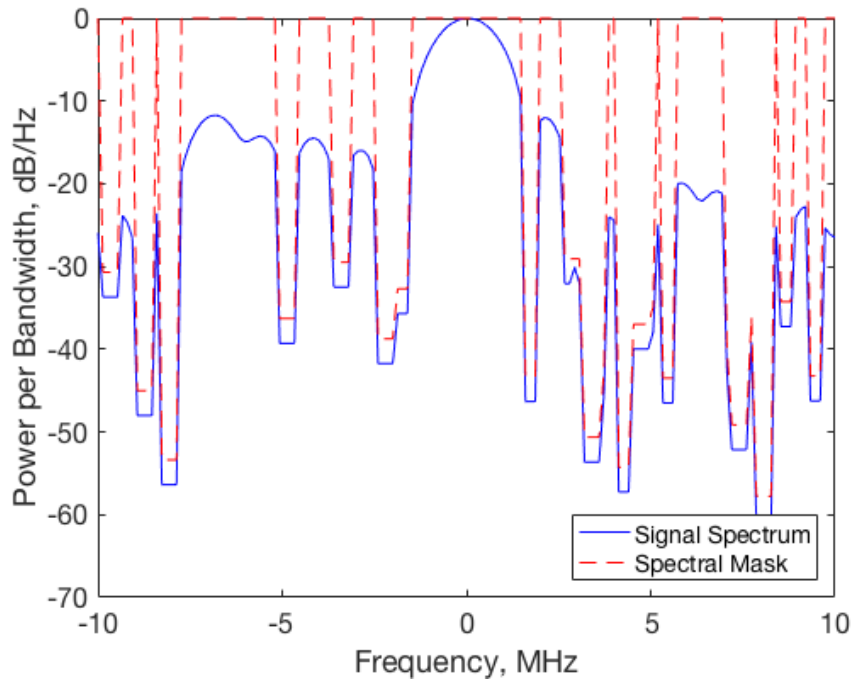


Figure 2.16. Spectral mask and resulting optimized range radar waveform at 3.48 GHz for the helix antenna pattern aimed at 45° in a 300 receiver environment. © 2018, IEEE.

CHAPTER THREE

Real-Time RF Device Performance Evaluation using Software-Defined Radios

The work presented in this chapter has been published in: [34] A. Egbert, B. H. Kirk, C. Baylis, A. Martone and R. J. Marks, "Fast Software-Defined Radio-based System Performance Evaluation for Real-time Adaptive RF Systems," *2020 95th ARFTG Microwave Measurement Conference (ARFTG)*, 2020, pp. 1-4, doi: 10.1109/ARFTG47271.2020.9241369. © 2020, IEEE.

3.1 Motivation

By their nature, adaptive RF systems require some type of performance feedback loop in order to obtain the optimal performance. While a system could be precharacterized to determine the optimal configuration in advance for a variety of scenarios, such an approach severely limits the degree of adaptation that is possible. As an example, it would be extremely impractical to attempt to precharacterize all the possible solutions to the scenario presented in Chapter Two, as there is tremendous freedom in the degree of severity and location of the constraints alone.

Since precharacterization is not feasible, the optimal configuration must be found through some type of search process, necessitating the use of live performance feedback. The time required to determine the current performance of a system is one of the primary limiting factors on how fast and responsive an adaptive system can be; other factors include the component reconfiguration latency (e.g., how quickly can an impedance tuner adjust its impedance) and the computational requirements of the optimization algorithm. The objective of this chapter is to provide fast evaluation of an amplifier's performance for use in real-time circuit optimization.

3.2 Review of the State-of-the Art

Traditional RF test benches using standard bench-top measurement equipment (signal generators, power meters, spectrum analyzers, and load-pull systems, both passive and active) can provide excellent accuracy when evaluating the performance of an RF system, but they are either too slow, too large, or otherwise ill-suited for use in a real-time adaptive system. While active load-pull systems in particular are able to achieve fast measurement speeds (with Roblin demonstrating full load-pulls in 10 ms [27]), they are an inappropriate choice for deployed systems (especially high-power systems) as they rely on the injection of specific active signals to modulate the presented impedance. Such injected signals must be on the order of the amplified signal to evaluate the full range of impedances, and the required excitation signals conflict with the need to transmit a desired signal through the system. Passive load-pull systems do not share this issue, but they are much too slow when used with traditional equipment, as demonstrated later in this chapter.

Meanwhile, many cognitive and adaptive radio and radar platforms are controlled by a software-defined radio (SDR), including the Software-Defined Radar (SDRadar) system, which is described in detail in Chapter Four. Performing measurements directly with an SDR platform that is likely already a major component of a system can reduce cost and size, thereby eliminating the need for additional measurement equipment.

The use of SDR technology for evaluating the performance of an RF system has been demonstrated for some metrics. For instance, Tendürüs has demonstrated the use of SDRs for evaluating an RF device's adjacent channel power ratio (ACPR, a measure of spectral spreading commonly used to evaluate device linearity) when transmitting

orthogonal frequency division multiplexing (OFDM) signals [28]. Though not evaluating a device under test (DUT), Jordbru has demonstrated the use of SDRs for environmental RF energy detection using both off-the-shelf and custom SDR designs [29]. Additionally, Andrich has analyzed the accuracy of SDR measurements for evaluating the performance of high precision clocks [35].

This chapter goes beyond the existing work in SDR measurements by demonstrating the accuracy and speed of two additional performance metrics (microwave transmit power and spectral mask compliance) using the Ettus X310 SDR, including a technique for calibrating the signal processing and propagation delays in the measurement chain, permitting reliable measurement of pulsed waveforms. Combined with high-speed impedance tuners, the new measurement processes demonstrate significant speed improvements over passive load-pull systems, reducing the per-impedance evaluation time for transmit power by 97% and providing a measurement framework capable of real-time evaluation of a transmit-chain reconfigurable amplifier.

3.3 SDR-based RF Performance Measurements

When using this SDR for measurement purposes, the process begins by acquiring the raw in-phase and quadrature (IQ) voltage samples of the complex baseband signal for evaluation. These samples are passed through the SDR's on-board field-programmable gate array (FPGA) in a streaming fashion for additional processing, with the specific processing dependent on the type of measurement being performed. Note that multiple, parallel measurement processing pipelines can parse the incoming data simultaneously, allowing for fast, efficient calculation of multiple performance metrics. Additionally,

processing the signal on the FPGA reduces the communication overhead required to transfer the data to the host computer, as only the final result must be transferred.

3.3.1 RF Power

Using this raw IQ data, the average RF output power of a 50 Ω system can be determined by computing the average of the root-mean square voltages of each IQ sample as discussed in [36]:

$$P_{out} = \frac{1}{N} \sum_{n=1}^N \frac{(I_n U)^2 + (Q_n U)^2}{2(50)}, \quad (3.1)$$

where P_{out} is the measured average RF power over N samples at the SDR's loopback measurement port in watts, I_n and Q_n are the instantaneous IQ samples in raw analog-to-digital converter (ADC) units, U is the conversion factor between ADC units and volts, and 50 represents the system reference impedance of 50 Ω .

When performing this calculation using the SDR, the ADC conversion factor U , dependent on the exact system configuration (including front-end amplifier gains and ADC settings), may not be readily known. This conversion factor can be factored out of the calculation of P_{out} on the FPGA and applied later if desired, which is the approach taken in this chapter with the demonstrated system. In this case, the simplest calculation (in units-squared) sufficient to determine relative performance of different configurations of a real-time adaptive system performance is

$$P_{rel} = \frac{1}{N} \sum_{n=1}^N (I_n^2 + Q_n^2). \quad (3.2)$$

If exact knowledge of the system's performance is desired, this intermediate calculation can be transferred to the host computer and converted to peak volts-squared:

$$P_{out} = U^2 P_{rel}. \quad (3.3)$$

Conversion to watts can be obtained by also dividing by twice the system reference impedance, returning to the form of (3.1). Further conversion to dBm and reference plane de-embedding can also be computed using regular methods. This process is illustrated in Figure 3.1 for the custom load-pull system presented in this chapter, with an intermediate LabVIEW driver handling communication between the SDR and a custom MATLAB load-pull bench control engine.

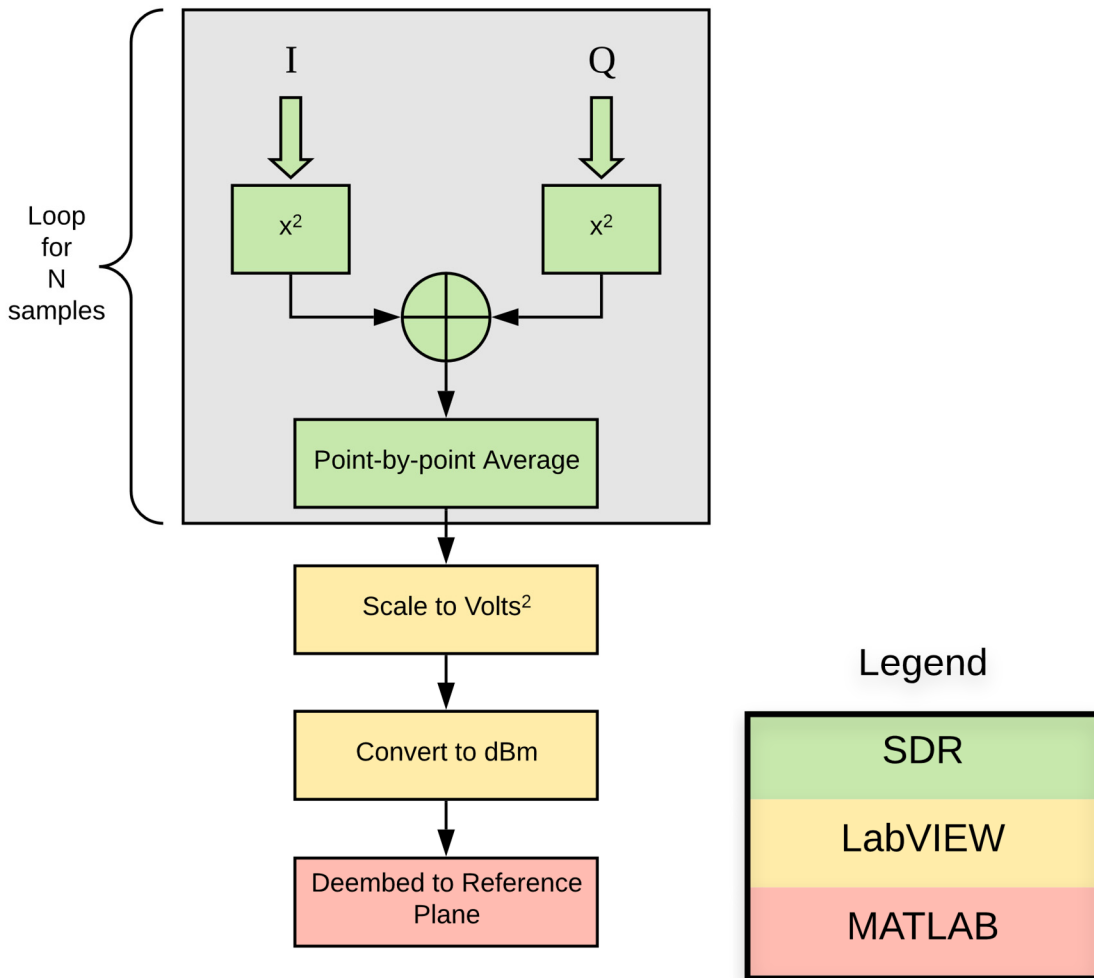


Figure 3.1. Flowchart for calculation of average RF output power over N samples for a custom load-pull system. © 2020, IEEE.

For high-accuracy power measurements, the reported values can be calibrated by measuring a known reference signal at various power levels with both a traditional, calibrated RF power meter and the SDR prior to system deployment. A correction table is created from these measurements, based on the difference between the measured value and the known reference value. This correction table can be applied to provide an accurate value for each SDR power measurement.

3.3.2 Spectral Mask Compliance

Spectral mask compliance can be determined by comparing a normalized received signal's spectrum to a predefined mask using the S_m metric of Fellows [37]:

$$S_m = \max_{f_m} (S(f_m) - M(f_m)), \quad (3.4)$$

where $S(f)$ and $M(f)$ are the normalized amplitude of the signal spectrum and the predefined spectral mask, both measured in dB, and f_m indicates all frequencies outside the main transmit band. As performed in regulatory measurements, the maximum in-band power is fixed at 0 dBc, and the mask is applied relative to the maximum in-band power. Here, values of S_m less than 0 dB indicate compliance with the spectral mask, while values of S_m greater than 0 dB indicate a violation of the spectral mask (transmission exceeding the allowed mask power outside of the permitted transmit band).

Because of the computational complexity of logarithms and exponentials on an FPGA, it is more efficient to use linear units (rather than dB) during the FPGA calculations, with conversion to dB performed later on the host computer if desired. As with power measurements, it is also beneficial to use raw ADC values during the calculations. Additionally, rather than normalizing the measured spectrum by dividing each sample by the maximum spectrum value, it is best to scale the normalized mask

definition up to match the maximum value of the waveform spectrum because of the lower computational complexity and latency of multiplication compared to division on FPGAs.

Multiple S_m measurements are often needed to achieve consistent measurements due to measurement noise, even with standard bench-top equipment [38]. Rather than averaging multiple spectrum measurements for each S_m calculation, resource usage on the FPGA can be minimized by calculating S_m for each spectrum measurement and averaging multiple S_m results. Accuracy of each spectrum measurement using an SDR can be ensured through the application of IQ imbalance corrections [39]. This approach is illustrated in Figure 3.2.

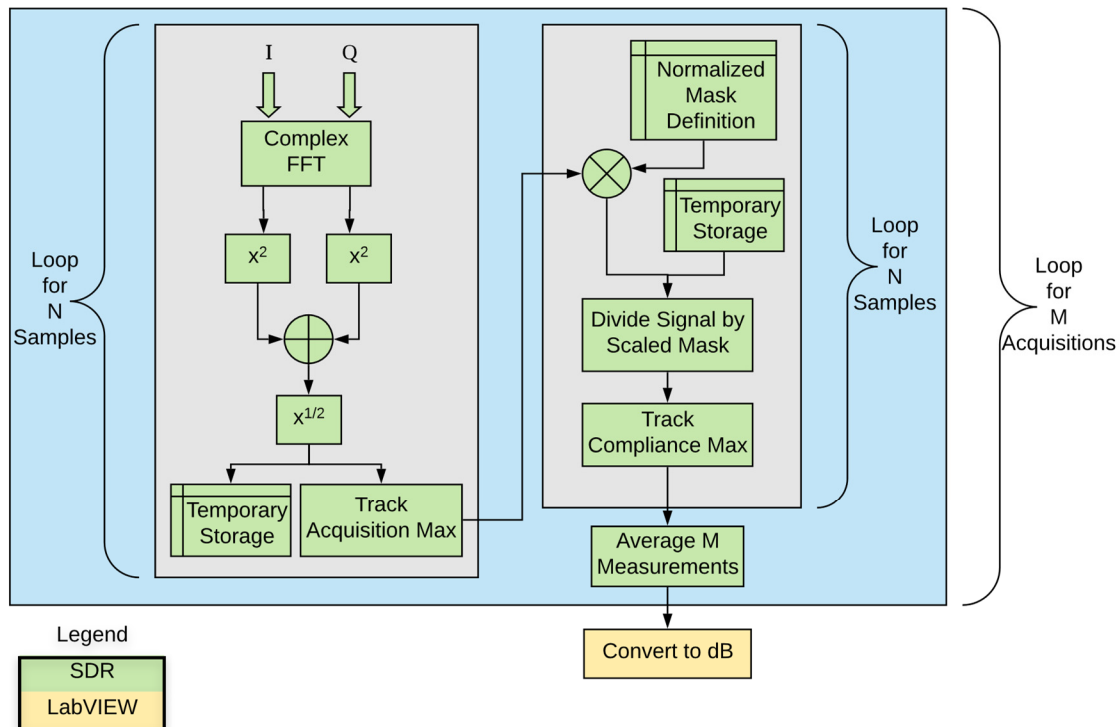


Figure 3.2. Flowchart for calculation of spectral mask compliance over N samples and M acquisitions for a custom load-pull system. © 2020, IEEE.

3.4 Pulsed Waveform TX/RX Synchronization

To apply the power and spectrum measurement techniques of this chapter to a real-time adaptive pulsed RF system (such as the radar transmitter in Chapter Four), the measurement period must consistently align with the transmission period, accounting for latency between transmission and signal observation due to signal processing and propagation (TX/RX latency). This latency may vary according to changes in the signal path due to varying test environments (cables, adapters, etc.) or system parameters that affect the rate of signal processing (sample rate, on-board FPGA clock speed, etc.).

Continuously monitoring the received signal and triggering measurements when a specified power threshold is exceeded is not sufficient, as variations in output waveform amplitude levels resulting from reconfiguring the load impedance can result in inconsistent latency measurements. Instead, the system's TX/RX latency can be evaluated on the first transmission cycle and applied as a delay to each transmission cycle. The latency should be determined using an initial system configuration with a known receive power threshold. This process is illustrated in Figure 3.3.

3.5 Load-Pull Demonstration

These measurement techniques have been tested in a load-pull context, where multiple load impedances are presented to a DUT to characterize the effect of load impedance on performance. A state-of-the-art system using Maury Microwave's Automated Tuner System software with standard RF bench-top equipment (Keysight Technologies signal generator and power meter/sensor) and a Maury Microwave passive automated load-pull tuner serves as a baseline for comparison. The novel SDR-based system utilizes an Ettus X310 SDR with UBX-160 RF daughtercards and the second-

generation 90 W evanescent-mode cavity-based impedance tuner of Semnani [26], shown in Figure 3.4. All load-pull measurements were performed with a 60 MHz linear frequency modulated (LFM) chirp waveform centered at 3.3 GHz transmitted through a Skyworks 65017-70LF InGaP packaged amplifier with an input power of 3 dBm and an amplifier bias voltage of 7 V.

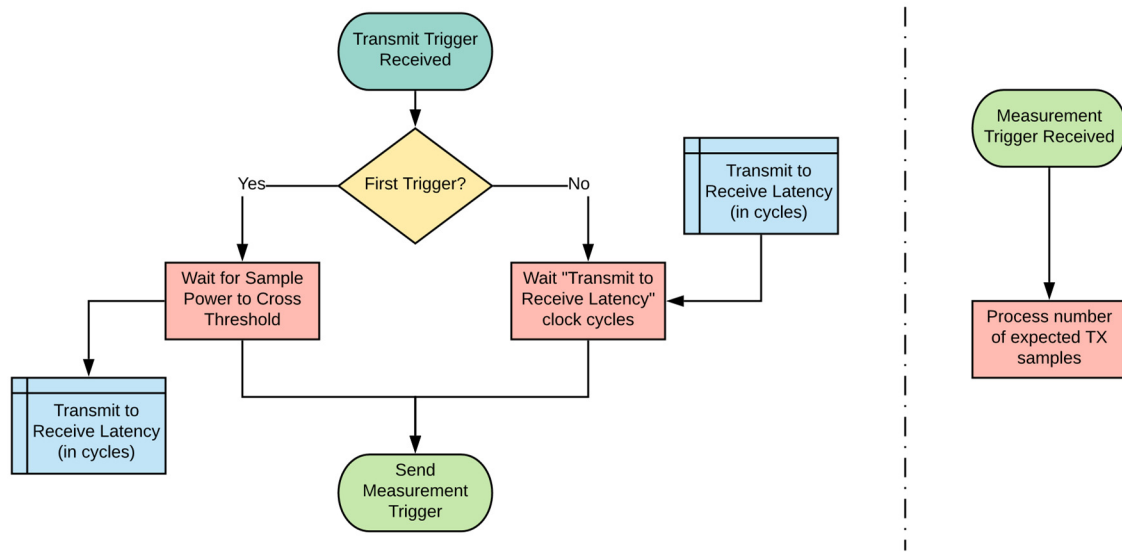


Figure 3.3. Flowchart for latency calibration in pulsed measurement systems. © 2020, IEEE.

Load-pull contours of the resulting RF output power measurements using both systems are presented in Figure 3.5. Table 3.1 compares the number of evaluated impedances and the time required for each system to complete the load-pull, as well as the maximum performance and corresponding load impedance according to each system. Comparison of the resulting contours and optimum impedances reveals good agreement between the two platforms. Furthermore, the SDR system evaluates each impedance in roughly 3% of the time needed for the traditional system due to significantly faster tuning times (roughly 30-100 ms vs 3-5 s) and reduced equipment communication overhead.

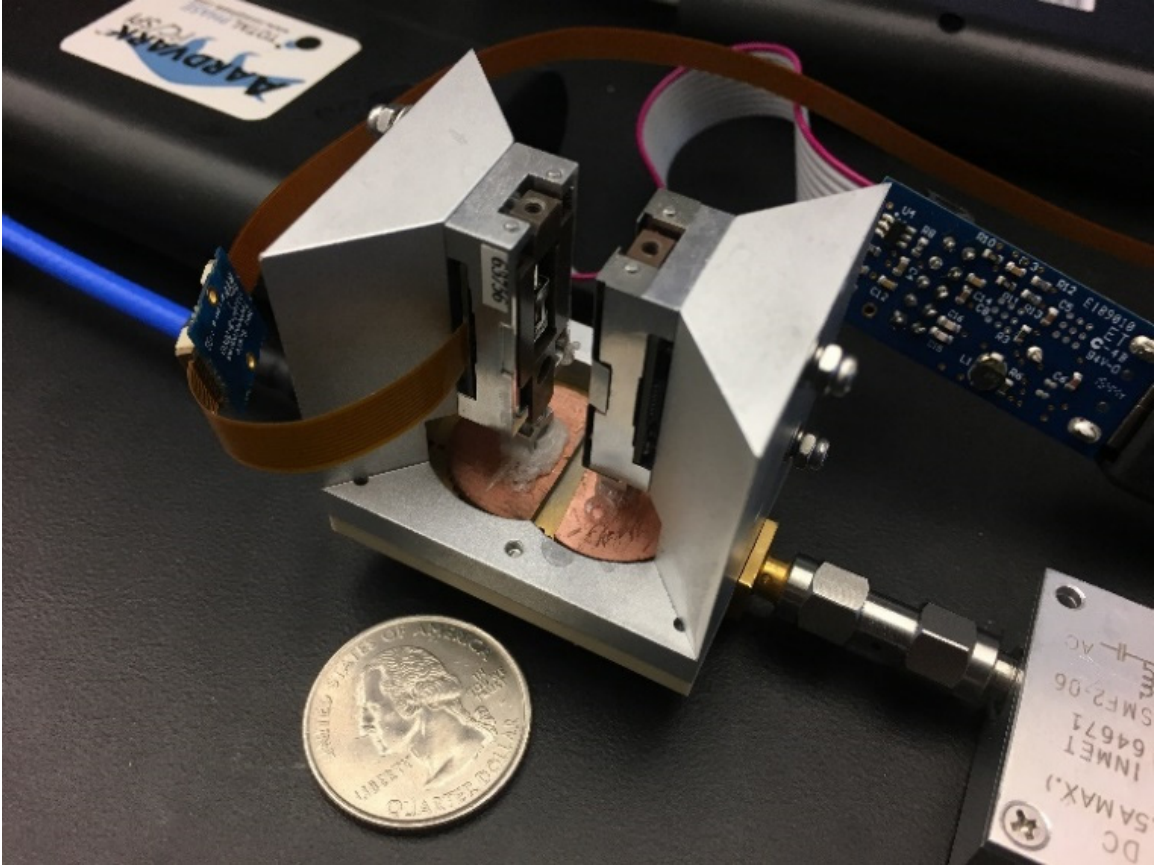


Figure 3.4. Second-generation evanescent-mode cavity tuner of [26]. Impedance adjustments are performed by raising and lowering the discs connected to the linear actuators. The extension lengths of the actuators are described by the parameters n_1 and n_2 .

Although the Maury load-pull system does not provide built-in support for spectral mask compliance measurements, a load-pull of S_m using the cavity tuner and SDR is included in Figure 3.6 to demonstrate the SDR platform's capabilities. The time required for this load-pull was 38.3 s for 246 evaluated points, or 156 ms per point.

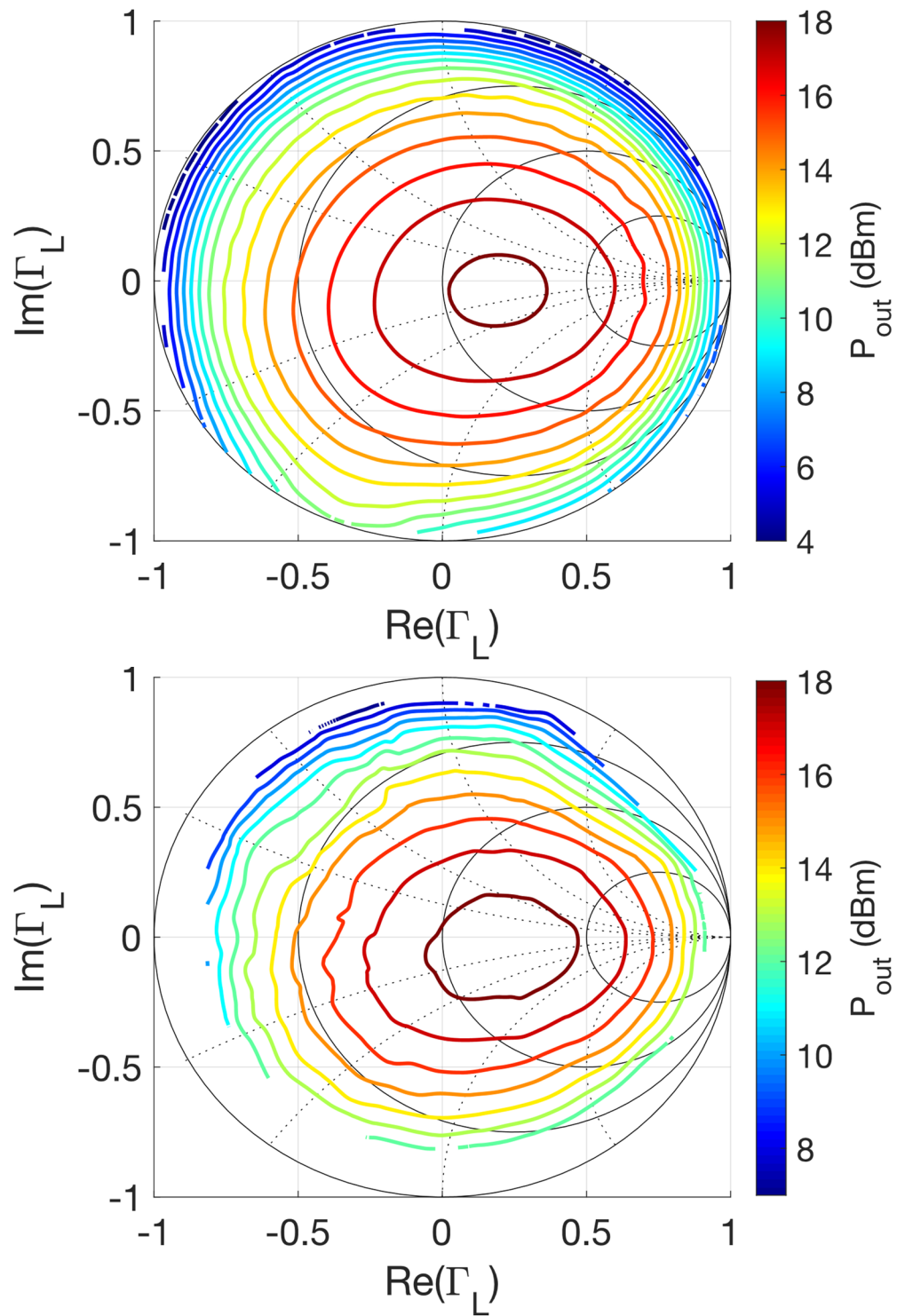


Figure 3.5. Load-pull of RF output power using the baseline system (top) and the SDR-based system (bottom). Contours have 1 dB spacing ranging from 4-18 dBm (top) and 7-18 dBm (bottom). © 2020, IEEE.

Table 3.1. Comparison of Standard and SDR-Based Load-Pull Systems for RF Output Power Evaluation

Load-Pull System	Points Measured	Time Elapsed (s)	Max P_{out} (dBm)	Γ_L at Max P_{out}
Standard	160	759.9	18.19	$0.1881\angle -9.28^\circ$
SDR-Based	246	38.4	18.42	$0.2393\angle -10.84^\circ$

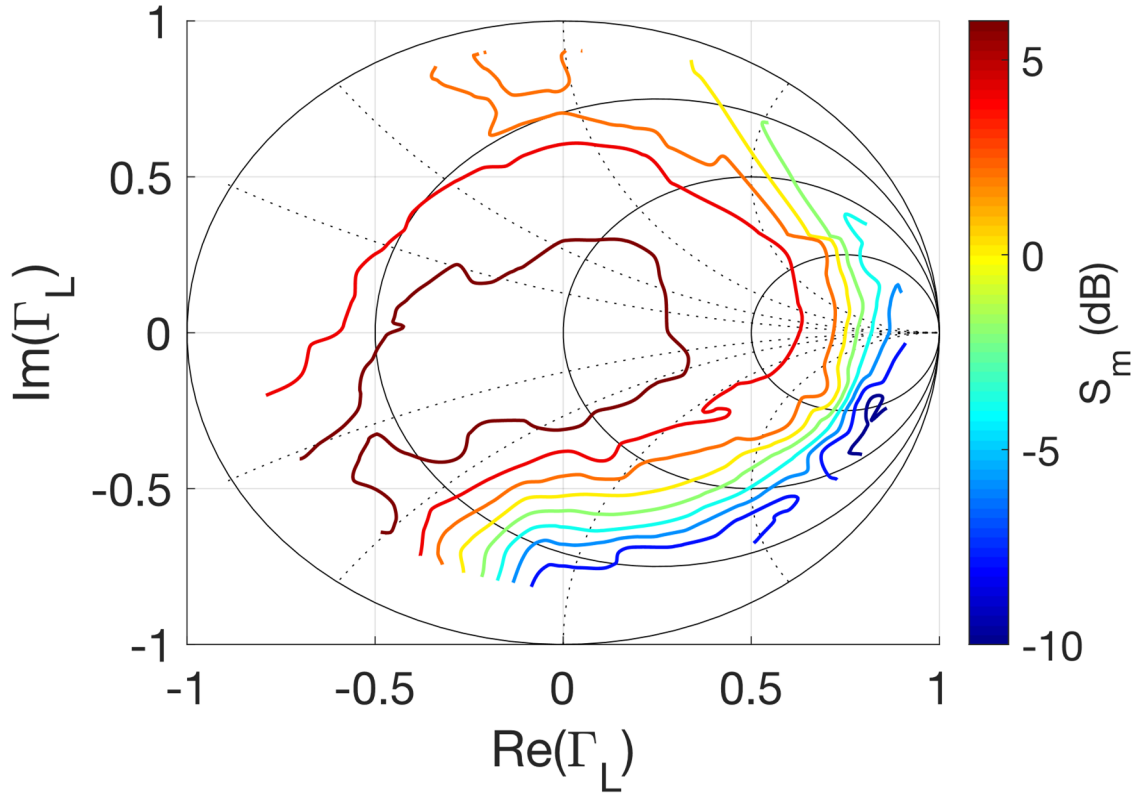


Figure 3.6. Load-pull of spectral mask compliance using an SDR-based RF load-pull system. Contours for $S_m = -10$ dB to $+6$ dB are shown with 2 dB spacing. © 2020, IEEE.

This real-time SDR measurement platform enables the use of live performance evaluation in a deployed, adaptive RF system. The approaches shown in this chapter provide the measurement foundation for the adaptive cognitive radar transmit amplifier presented in Chapter Four.

CHAPTER FOUR

Real-Time Independent Optimization of Cognitive Radar Transmit Amplifier

Portions of the work presented in this chapter have been published in: [40] A. Egbert, A. Goad, C. Baylis, R. J. Marks and A. Martone, "Detecting Potential Performance Improvements in Cognitive Radar Systems," *2021 IEEE Radar Conference (RadarConf21)*, 2021, pp. 1-5, doi: 10.1109/RadarConf2147009.2021.9455339. © 2021, IEEE.

The remainder has been accepted for publication in: [41] A. Egbert *et al.*, "Continuous Real-Time Circuit Reconfiguration to Maximize Average Output Power in Cognitive Radar Transmitters," accepted for publication in *IEEE Transactions on Aerospace and Electronic Systems*, July 2021.

4.1 Cognitive Radar Overview and Problem Description

To further relieve the spectral congestion described in Chapter One, the United States has begun to open certain bands for spectrum-sharing. Under spectrum sharing, multiple categories of users are permitted to operate in a given portion of the spectrum, typically with one group being designated as the primary user. For example, 100 MHz of mid-band spectrum from 3450-3550 MHz, previously allocated to radar, has been re-allocated for sharing with 5G wireless communications as the primary user through America's Mid-Band Initiative [42], with some restrictions to protect remaining incumbent federal users [15]. The increasingly congested, spectrum-sharing environment in which modern radar systems must operate requires radars that can change operating frequencies quickly over significant bandwidth while maintaining good performance. The challenges posed by such a dynamic spectral environment can be intelligently navigated by cognitive radars.

According to Martone, Haykin, and Griffiths, a cognitive radar, by definition, must contain intelligent signal processing, information feedback, and the capability to adapt its waveform [43-45]. One such radar is the Software Defined Radar (SDRadar) platform presented by Kirk [46-48]. In cognitive radars, the perception-action cycle (PAC) is often used to form the decision processes. The radar senses the spectrum and the frequencies of interferer operation (perception), then modifies its transmission to achieve coexistence with other radio-frequency devices (action) [30, 47-51]. As part of its perception, a cognitive radar may also employ spectral prediction to determine spectrum usage by potentially interfering devices, allowing the radar to anticipate and respond to upcoming changes rather than merely react after the fact [52-53].

In the radar's transmit power amplifier (PA), the output power is dependent on the load impedance provided to the active device [54] as well as the radar's transmit configuration (center frequency, bandwidth, and waveform) [55]. To maximize the radar's detectable range, impedance tuning can be performed on the PA in real-time. Tuning of a narrow-band matching network provides the potential for higher gain compared to a fixed, broadband matching network due to the theoretical gain-bandwidth tradeoff described by the Bode-Fano Criterion [56-58]. Many approaches for impedance optimization have been explored in the literature, including: locating constant power contours and proceeding towards increased performance [59], fitting measured data to an equation and solving for the optimal value [60], genetic algorithms controlling a hybrid varactor/MEMS switch tuner [61], and alternatively searching for optimal reflection phase and gradually increasing reflection magnitude [62]. However, Barkate has

demonstrated that gradient-based methods perform well for real-time circuit optimization when compared with other typical algorithms [63].

Previously, Dockendorf and Alcalá-Medel have used the first- and second-generation high-power evanescent-mode cavity tuners of Semnani [25-26] to demonstrate a fast gradient-based search algorithm for maximizing the PA's PAE while meeting spectral compliance, and they have shown that a software-defined radio can be used to control impedance tuning in similar applications using earlier versions of the techniques of Chapter Three [24, 64-65]. These works have demonstrated optimization times on the order of 1-10 s. However, although the measurement process has been significantly streamlined using the processes and techniques of Chapter Three, the fastest tuning times for the cavity tuner of [26] are between 30 and 50 ms for one tuning operation, which is much longer than the pulse repetition interval (PRI) of most radars (often less than 1 ms). As such, within the time required to perform even a single impedance tuning operation, a cognitive radar is likely to alter its transmit configuration multiple times. To allow the radar to adapt freely from pulse to pulse, an approach must be devised that will allow optimization while the underlying system is modifying its configuration independently of the impedance tuning process. Note that faster components and measurements alone are not sufficient to overcome these issues, as discussed later in Section 4.3.1 and Chapter Seven.

To independently optimize a time-varying system (such as a cognitive radar), several complications must be addressed. Because the optimal circuit configuration will necessarily change over time, continual monitoring and re-optimization is required. While gradient algorithms have been adapted to perform continuous tracking of time-

varying optima [66-67], they require that the system remains time-invariant during individual gradient evaluations, which would limit the adaptation rate of the cognitive radar. To overcome this limitation, multiple transmit configurations must be considered simultaneously and optimized in aggregate. An earlier version of the algorithm discussed in this chapter uses a method that evaluates the gradient of several configurations simultaneously [68], but this method does not directly optimize average system performance. Alternatively, the scalarization technique of Miettinen [69] provides a useful framework that can be adapted to evaluate the average performance of the time-varying system, which is used in this chapter. However, the length of time required to accurately evaluate system performance must be addressed in both of these approaches, as recognized by McBride [70].

To address the problems facing impedance tuning within a cognitive radar context as described in this section, this chapter presents a modified gradient search algorithm that maximizes the cognitive radar PA's average output power and corresponding maximum detectable range over a dynamic measurement period during active spectral adaptation as performed by the SDRadar platform. This algorithm consists of four individual algorithms: the primary average performance gradient search (Section 4.4.1) and supplementary algorithms that optimize search parameters controlling the averaging period (Section 4.4.2), search step size and convergence (Section 4.4.3), and search activation in response to changes in the cognitive radar's behavior (Section 4.4.4).

4.2 Software-Defined Radar (SDRadar) Overview

While the techniques presented in this work can be adapted to many cognitive radar systems, this chapter demonstrates its approach using an extended version of the

Software-Defined Radar (SDRadar) platform of Kirk [30, 47-48]. As alluded to in Chapter Three, the SDRadar platform is built using an Ettus X310 SDR with two UBX-160 RF daughterboards in conjunction with a host computer system. As used in this chapter, the SDRadar monitors its current 100 MHz operating band and reacts to interference in its band by selecting the largest unoccupied portion of the spectrum to use for radar operations. This adaptation occurs for each transmitted radar pulse. A block diagram of this system outlining the separation between SDR and host computer functionality is shown in Figure 4.1; modifications made as part of the work in this chapter are outlined in green and discussed throughout this section.

While the original SDRadar system was designed to operate for a finite period of time (up to a few seconds) with all collected data being stored for additional evaluation and processing offline, this work necessitated adjusting the system to operate indefinitely by streamlining the data processing, migrating much of the cell-averaging constant false-alarm rate (CA-CFAR) processing to the graphics processing unit (GPU), and discarding older collected data over time.

Additionally, band-hopping capability has been introduced to the SDRadar for use in instances where the current 100 MHz band does not provide sufficient open spectrum for operation. If the SDRadar detects that the largest unoccupied portion of its current band is narrower than a specified threshold, it will randomly switch to one of its other permitted 100 MHz bands, sampled without replacement until the list is exhausted.

To perform real-time PA optimization, an external transistor with an adjustable load impedance tuner (labeled as Z_L in Figure 4.1) and a coupled loopback connection to a separate SDRadar receive channel has also been included. This loopback connection

enables evaluation of the output power of the amplified SDRadar system using the pulsed waveform power measurement process described in Chapter Three. The hardware block diagram for a deployable SDRadar system is shown in Figure 4.2.

Unless otherwise noted, all tests in this chapter are performed on live hardware using the configuration of Figure 4.3 with a Microwave Technologies MWT-173 field-effect transistor (FET) as the amplifier with $V_{DS} = 4.5$ V, $V_{GS} = -1.4$ V, and $P_{in} = 14$ dBm. The load impedance presented to the transistor is controlled using the second-generation evanescent-mode cavity tuner of Semnani [26]. The SDRadar is configured to operate with a PRI of 409.6 μ s and pulse length of 10.24 μ s (2048 samples at a sample clock rate of 200 MSa/s), with allowed operation bands of 100 MHz centered at 3.1, 3.2, 3.3, 3.4, and 3.5 GHz and a band hopping threshold of less than 10 MHz of contiguous unoccupied spectrum. For test purposes, a congested spectral environment is simulated using several sets of pre-generated radio-frequency interference (RFI) loaded onto the SDR and played back using the second transmit channel of the device. RFI transmission is disabled whenever RF power measurements are active to avoid interference from signal coupling in internal components.

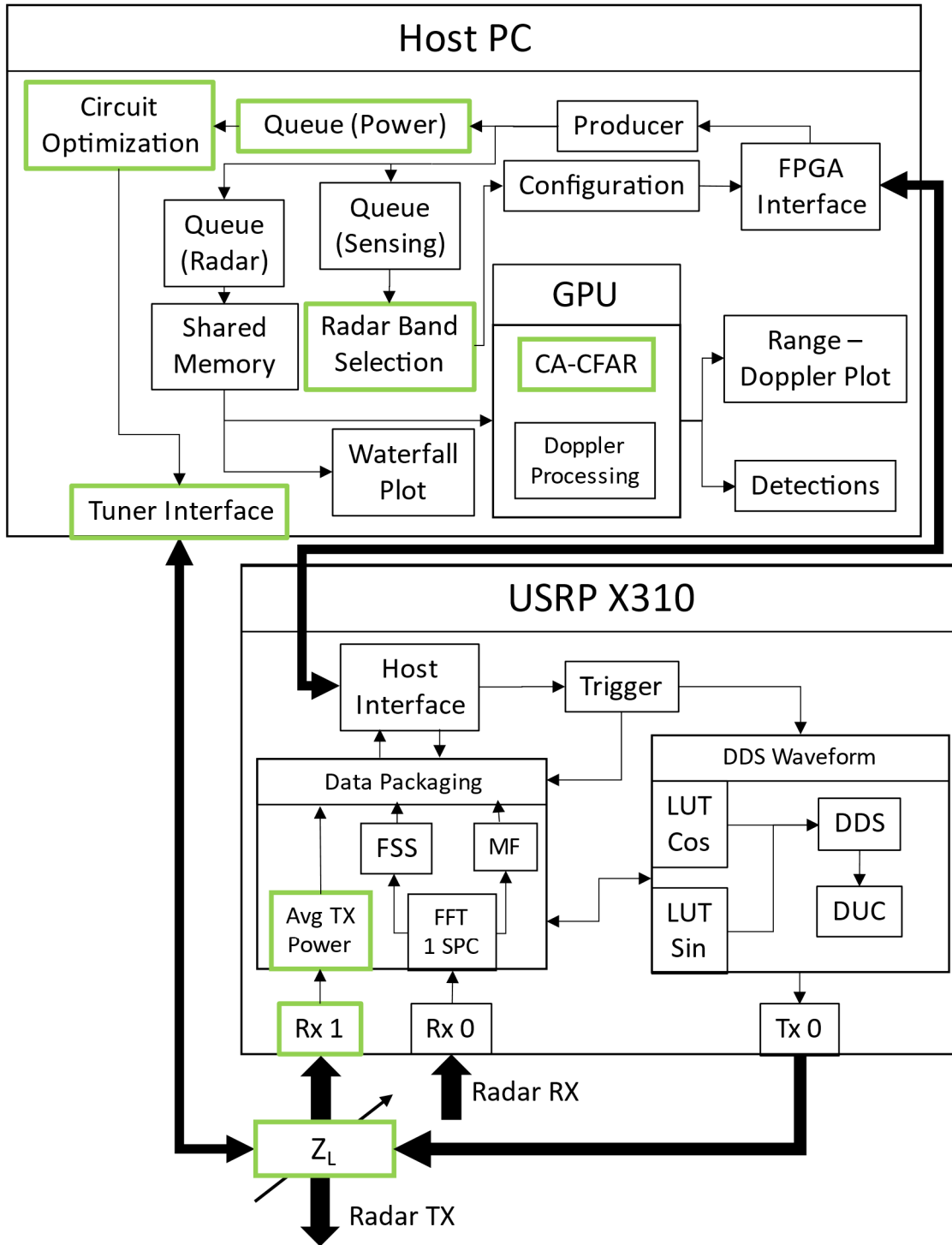


Figure 4.1. SDRadar system architecture using an SDR, host computer, and adaptive transmit amplifier (denoted Z_L). Modifications to the SDRadar architecture of [30] are outlined in green. Figure adapted from [30] with permission. Useful acronyms: fast spectral sensing (FSS) [71], matched filter (MF), look-up table (LUT), direct digital synthesis (DDS), digital upconversion (DUC), fast Fourier transform (FFT), samples per cycle (SPC), cell-averaging constant false alarm rate (CA-CFAR).

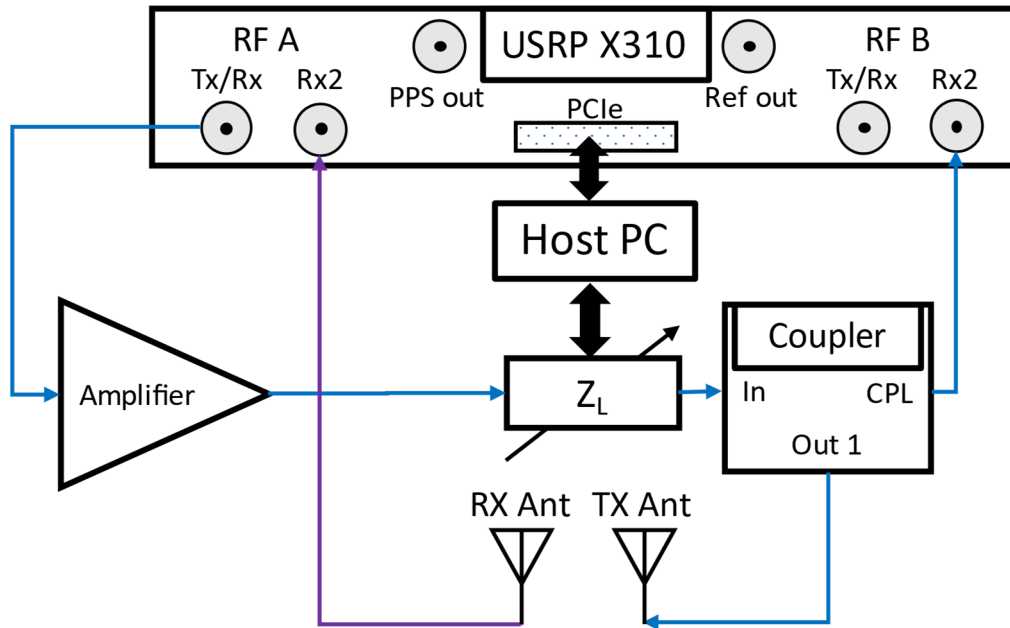


Figure 4.2. Hardware block diagram for a deployed SDRadar system with SDR, host computer, adaptive transmit amplifier, and transmit and receive antennas. SDRadar transmit signal travels along the blue path, while target responses and interference are received through the purple path. Figure adapted from [47] with permission. The coupler connected to RF B Rx2 should be selected such that the loopback power does not exceed the maximum SDR input power of -15 dBm.

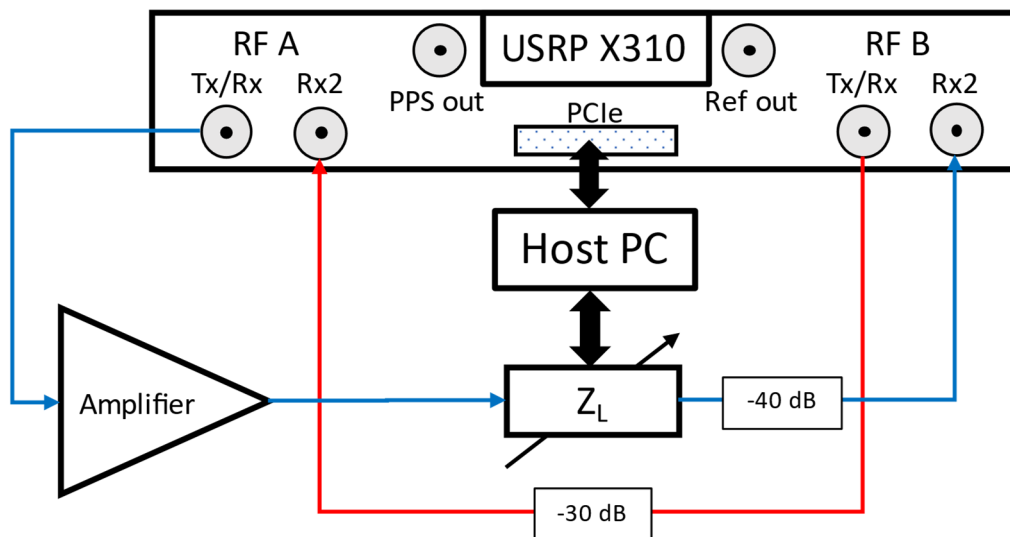


Figure 4.3. Hardware block diagram for SDRadar system testbed with SDR, host computer, and adaptive transmit amplifier. This hardware configuration is used for all tests discussed in this chapter. Synthesized RFI travels along the red path (RF B Tx/Rx to RF A Rx2), while SDRadar transmit signals travel along the blue path (RF A Tx/Rx to RF B Rx2). Figure adapted from [47] with permission.

4.3 Adapting Gradient Methods to Cognitive Radar

Existing approaches for real-time circuit optimization using gradient-based algorithms can optimize an uncharacterized system within a few seconds [24, 65]. However, one common assumption shared by these approaches is that any system parameters outside the control of the optimization algorithm are held static for the duration of the optimization. While some consideration has been given to later system changes after optimization [64], the behavior of a truly adaptive transmitter, which can adjust its transmit configuration on the order of microseconds in response to changes in the spectral environment, has not been addressed. These rapid changes lead to two primary difficulties that must be overcome to apply gradient-based algorithms to truly adaptive systems: acquiring meaningful estimates of the desired system performance metric's gradient and handling instances where the optimal circuit configuration varies over time.

4.3.1 Acquiring Meaningful Gradient Estimates

The success of a gradient search strongly depends on the quality of its gradient estimations. Reliable estimates of the gradient for a given system performance metric can be obtained by evaluating the metric (dependent variable) at various values of load reflection coefficient or load impedance (independent variable). To obtain valid gradient estimations while tuning the impedance, all system parameters (aside from impedance) must be held constant during the set of measurements used to compute the gradient; otherwise, the gradient will not reflect the impact of impedance on performance. This requirement conflicts with the adaptive nature of a cognitive radar, since the radar may vary other system parameters (such as the transmit frequency, bandwidth, and signal

content) during a single gradient estimate, all of which impact the evaluated performance metric and corrupt the observed relationship between performance and impedance. Note that this effect may not necessarily manifest as a change in the optimal impedance. Even in cases where the performance of various signals with respect to impedance differs only by some constant offset (sharing the same optimal impedance, but different performance at that optimum), this constant performance offset can be enough to skew the gradient in the direction that was evaluated while the better performing configuration was active.

The simplest approach to integrate spectral adaptation and circuit optimization is to throttle the rate of spectral adaptation such that the transmit configuration is held constant throughout each gradient evaluation, ensuring performance differences can be attributed solely to changes in impedance. However, such an approach would result in an unacceptable decline in the radar's ability to quickly respond to changes in the available spectrum, as it is no longer permitted to adapt the radar's transmission during measurements for a gradient estimation, even if the chosen pulse is no longer ideal for the current spectral environment.

Alternatively, given a PRI that is substantially longer than the transmission duration and a sufficiently fast impedance tuner, one might attempt to optimize the transmit circuitry for each pulse in loopback. By using a switch, the transmit antenna would be disconnected during the interval in which the receiver is gathering and assessing the radar returns, allowing a full optimization utilizing multiple performance evaluations of the next pulse to be performed prior to transmission. Unfortunately, impedance tuning technology capable of handling the high power required of a radar transmitter that can also adjust multiple times over the course of a single PRI is not yet

available. Additionally, optimizing in loopback during the “off” times of the radar negatively affects the power efficiency of the system, as the power used during optimization must be dissipated through non-transmissive means. Finally, this non-transmissive “dummy load” must itself be an adaptive component capable of emulating the antenna’s impedance; if not, then the impacts of the antenna on system performance are absent during the optimization process, defeating the purpose of the optimization. Without this adaptive dummy load, a tuner able to adapt once per PRI could be used in conjunction with a system that manages multiple simultaneous individual optimizations, each intended for a specific, unique transmit configuration, updating the optimization’s status when each configuration is utilized and subsequently evaluated.

Given the state-of-the-art high-power impedance tuner used for the experiments in this paper, a single impedance tuning operation requires approximately 30 ms. Assuming the PRI of 409.6 μ s used in this work and permitting the radar to adapt on a pulse-to-pulse basis, over 70 changes in transmit configuration can occur during a single impedance tuning operation, with many more changes over the course of a full optimization (which requires multiple tuning operations).

Instead, each gradient estimation must be performed while accounting for the impacts of other changes to the system, isolating the relationship between impedance and performance. By evaluating the performance metric multiple times at each sampled impedance and tracking when each transmit configuration was used for transmission, the search can account for the performance impacts of each configuration and estimate the relationship between impedance and performance for the current set of transmit

configurations. Throughout this chapter, the number of performance evaluations per impedance is referred to as the measurement window.

An existing approach using this philosophy computes independent gradients for each available transmit configuration and combines the direction of these gradients in a weighted fashion based on the relative occurrences of the configurations, with configurations that are used more frequently having more influence on the result [77]. Unfortunately, this (average gradient) method ignores the relative magnitude and slope of each configuration's performance contours, producing an optimization result that minimizes the weighted distance from the optimum impedances of the various transmit configurations, rather than maximizing the overall average performance, as illustrated in Figure 4.4. Given this difference, it is recommended to optimize the average performance directly, as demonstrated in Section 4.4.1.

In order to evaluate average performance, it is necessary to establish what period of time should be considered during each iteration, which was not addressed by [77]. This requires careful consideration of how the chosen measurement window for averaging will impact the performance of the search algorithm, especially as the cognitive radar's adaptation (and thus optimal averaging window) varies for different environments. If the measurement window is too small, it will not be possible to establish consistent performance weights for each configuration across each impedance. If the measurement window is too large, the search will be slower and less responsive to changes in the cognitive radar's behavior. These impacts and an approach for selecting the optimal measurement window mid-optimization are evaluated later in Section 4.4.2.

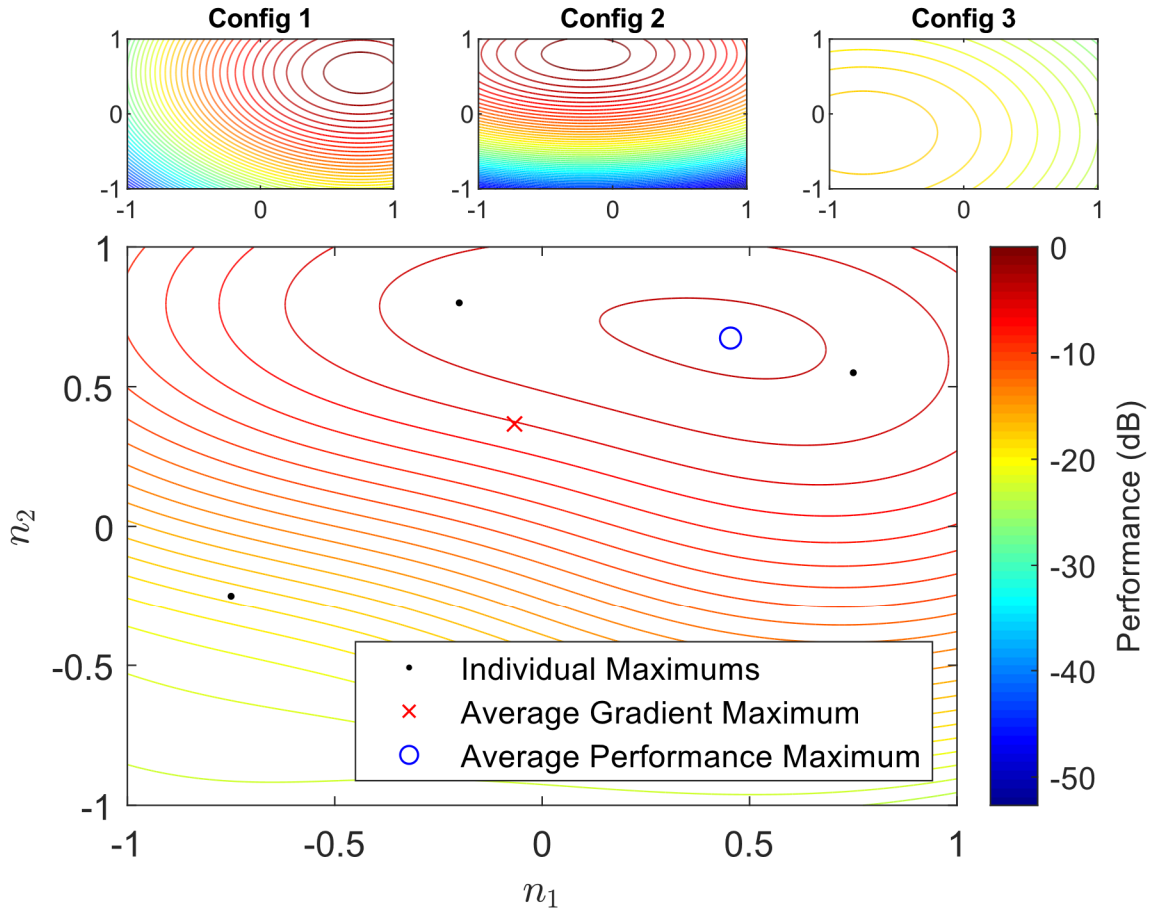


Figure 4.4 Performance contours associated with three hypothetical cognitive radar transmit configurations (top) and their average performance contours assuming equal probability of evaluating each configuration (bottom). Contours are drawn in 1dB increments, and the same scale is used for all contours. The maximum performance for each configuration, as well as the maximums attainable by the average gradient [77] and average performance approaches are indicated.

4.3.2 Time-Varying Optimal Circuit Configuration

While very rapid, frequently recurring transmit adaptations are handled by the proposed averaging approach, more infrequent variations that result in significant shifts in the optimal circuit configuration can impact the search algorithm over longer time periods. Gradient searches typically operate to convergence; that is, the algorithm has some step size that is decremented over time until the search attempts to decrease its step size below the specified lower limit. When the step size reaches this limit, a final

optimum value is selected, as implemented in many existing circuit optimization algorithms [24, 55, 64-65, 68, 72]. These algorithms lack a method for initiating additional optimization in response to changes to the optimal circuit configuration.

Alternate approaches for gradient-based optimization addressing time-varying performance contours exist under the umbrella of online optimization, such as the works of Mokhtari [66] and Dixon [67]. In those approaches, the gradient algorithm attempts to track a time-varying optimal solution with the least amount of error possible. Like other gradient algorithms, those assume each individual gradient evaluation is performed on a fixed set of performance contours and, if adapted to use the averaging technique of this chapter, could be applied to a cognitive radar.

However, those methods have some disadvantages when applied to cognitive radars. Generally, these algorithms are most effective if changes in the optimal solution are relatively continuous or smooth. For a cognitive radar, it is expected that the optimal solution following a change in operating band will often be uncorrelated to the previous optimal solution, as these changes will be driven by the external spectral environment. Additionally, in situations where the optimal configuration temporarily becomes static, (such as in the absence of interfering devices), gradient calculations would continue to be performed unnecessarily. In a physical system, this requires adjusting the system away from the optimal impedance, resulting in an undesirable loss of performance during the gradient measurement period.

Instead, when possible, it is preferable to converge to a fixed solution and wait for any changes to the cognitive radar's behavior that would suggest a need to resume the optimization process. To determine when a previous optimum configuration is no longer

applicable to the current environment, some portion of the cognitive radar's configuration or performance must be monitored for variation over time. While the radar's output power could be monitored for changes in performance, the radar may transition to a state where the current output power remains the same, but additional power could be obtained by reoptimizing for the new configuration. Instead, the technique of this chapter monitors the frequencies utilized by the cognitive radar, as this directly represents the current configuration.

For behavior monitoring purposes, the current utilized transmit frequencies are represented as a one-dimensional histogram, where bin height represents how often each frequency was utilized by recently transmitted waveforms. For consistency across varying bandwidths, this histogram is translated into a probability mass function (PMF) by dividing the weight of each element by the L1 norm of the distribution. Metrics for comparing such functions are common, including the Kullback-Leibler (KL) divergence [73], root-mean-square deviation (RMSD) [74], and earth mover's distance (EMD) [75]. The selected metric can then be correlated with potential power improvement, and a threshold can be used to specify when the radar should be reoptimized.

KL divergence, as defined by (4.1), is widely used in information theory to measure the relative entropy between two distributions [73]. However, this is not a true metric; that is, $D_{KL}(P||Q)$ is not necessarily equal to $D_{KL}(Q||P)$. Additionally, it can be non-finite when the two distributions contain different zero-valued entries, such as when the distributions do not overlap, as is often the case for utilized transmit frequencies distributions (especially following large shifts in frequency utilization).

$$D_{KL}(P||Q) = \sum_{n=1}^N P_n * \log\left(\frac{P_n}{Q_n}\right) \quad (4.1)$$

The RMSD metric, as defined by (4.2), does provide a true metric. However, it too is not ideal for this application, as it also is not able to provide information about non-overlapping distributions.

$$RMSD(P||Q) = \sqrt{\frac{\sum_{n=1}^N (P_n - Q_n)^2}{N}} \quad (4.2)$$

The EMD is a useful metric for comparing utilized frequency distributions. Originally proposed by Rubner [75] as a metric for determining the similarity of images, the EMD is analogous to the minimum amount of physical work required to transform one distribution into the other, and it provides a true metric when applied to normalized distributions. Given one-dimensional histograms with uniform bin width, the EMD can be computed as the sum of the absolute value of the cumulative sum of the differences between the distributions. For ease of thresholding in this application, knowledge of the possible transmit frequency range is used to normalize the EMD with respect to the max possible EMD, resulting in the final computation:

$$EMD(P, Q) = \frac{1}{N-1} \sum_{n=1}^N \left| \sum_{i=1}^n P_i - Q_i \right|, \quad (4.3)$$

where P and Q are one-dimensional PMFs of N bins. Unlike KL divergence and RMSD, EMD can represent the absolute distance between non-overlapping distributions. This ability is a requirement for any metric that is used, as this separation reflects the magnitude of a given frequency shift, which is the feature of interest for this work. Specific details of how this distance metric is utilized during optimization is discussed later in Section 4.4.4.

However, monitoring for changes after convergence does not address the difficulties that arise if the optimal configuration changes while the gradient-based

algorithm is still active. Consider a scenario where the algorithm has nearly converged to a solution, but the optimal solution suddenly moves to the other side of the search space. In this situation, the algorithm's current small step size will cause the algorithm to progress very slowly to the new solution, resulting in poor responsiveness to the change in radar transmission. To mitigate the impact of this situation, the algorithm can be permitted to reconsider its decision to decrease its step size, and instead increase the step size if it determines it is no longer near the current optimal solution. Specifics of this approach are discussed later in Section 4.4.3.

4.4 Algorithm Description

4.4.1 Average Performance Gradient Search

A gradient search is performed to maximize the output power of the amplifier, where estimates of the performance gradient with respect to the independent variables are used to guide the search process. In this work, the independent variables are the positions, labeled n_1 and n_2 , of the movable discs atop two resonant cavities in the second-generation evanescent-mode cavity tuner of Semnani [26] depicted in Figure 3.4. The values of n_1 and n_2 are specified in 0.5 μm increments from the highest position.

The gradient search is similar to the search approach presented by Baylis [72], with two differences: (1) the search is applied in the (n_1, n_2) plane, adjusting the fundamental control elements of the tuner, rather than a characterized optimization of load reflection coefficient Γ_L , and (2) the performance metric is the average output power over recent transmit configurations weighted based on the relative frequency of

occurrence of each configuration, rather than the measured output power of a single transmit configuration.

First, the tuner is set to its initial candidate (n_1, n_2) value, and the output power is evaluated N times, dictated by the current measurement window. This set of measurements typically includes multiple transmit configurations. Next, the tuner is moved to the nearest neighbor to the right, located at $(n_1 + D_n, n_2)$, where D_n is the candidate-neighbor distance. (The values of gradient search algorithm parameters used in this work, including D_n , are included in Table 4.1.) The output power is evaluated again using the same process as at the candidate impedance. This is repeated for the neighbor above the candidate point at $(n_1, n_2 + D_n)$, as shown in Figure 4.5(a). Any measurements from transmit configurations that were not encountered at each of the three points are not usable and are discarded; they cannot be used with the averaging method described below.

Using the power values measured at the candidate and the two nearest neighbors, the average power of the K usable configurations can be evaluated at each point as:

$$\bar{P}(i) = \sum_{k=1}^K w_k \frac{1}{M_{k,i}} \sum_{m=1}^{M_{k,i}} P(k, m, i), \quad (4.4)$$

where $P(k, m, i)$ is the m^{th} observed power (in watts) at the i^{th} gradient estimation point (candidate, first/second neighbor) of the k^{th} usable transmit configuration, $M_{k,i}$ is the number of times configuration k was encountered at the i^{th} point, and w_k is the average performance weight assigned to configuration k , as defined by:

$$w_k = \frac{\sum_{i=1}^3 M_{k,i}}{\sum_{\kappa=1, i=1}^{K, 3} M_{\kappa, i}}. \quad (4.5)$$

This process ensures that the average power evaluation for each point can be compared coherently across the three gradient estimation points, as the weighting assigned to each configuration is the same for all three points. Note that the simpler approach of naively averaging the performance obtained at each impedance would incorrectly assume that each configuration is used the same number of times at each impedance. Failure to account for this variance results in a gradient that does not accurately reflect the impact of impedance tuning alone. For instance, if the highest performing configuration was encountered unusually often at the upper neighboring point, the resulting gradient would be skewed upward. Additionally, it is clear from (4.4) that any configurations that are not observed at each impedance must be discarded, as the value of $M_{k,i}$ would be zero for at least one value of i , resulting in an undefined average power. Following this technique, the gradient of the average power can then be estimated as follows:

$$\nabla \bar{P} \approx \hat{n}_1 \frac{\bar{P}(2) - \bar{P}(1)}{D_n} + \hat{n}_2 \frac{\bar{P}(3) - \bar{P}(1)}{D_n}, \quad (4.6)$$

where \hat{n}_1 and \hat{n}_2 are the unit basis vectors defining the (n_1, n_2) search space. The unit vector in the direction of the average power gradient, \hat{P} , gives the direction of steepest ascent for average power:

$$\hat{P} = \frac{\nabla \bar{P}}{\|\nabla \bar{P}\|_2}. \quad (4.7)$$

Following this estimation of the performance gradient, the search proceeds one step distance D_s in the direction of \hat{P} , and the average power value is measured at this new candidate during a complete observation window. This step is shown in Figure 4.5(b). If the average power for the new candidate is higher than for the previous candidate

(computed using new values of w_k that only consider the two candidate points), the process is repeated beginning at the new candidate. If the average power for the new candidate is lower than for the previous candidate, D_s is divided by two, a candidate in the direction of \hat{P} at the new distance D_s is evaluated, and the search continues with a new gradient estimate. The process continues until $D_s < D_r$, the resolution distance.

Table 4.1. Gradient Search Parameters

Parameter	Symbol	Value
Candidate-Neighbor Distance	D_n	5
Initial Step Size	$D_s(0)$	50

If the optimum location changes after D_s is reduced, this reduction may need to be reversed to ensure responsive optimization. Supplementary algorithms for controlling the search size and other parameters are discussed in the next sections.

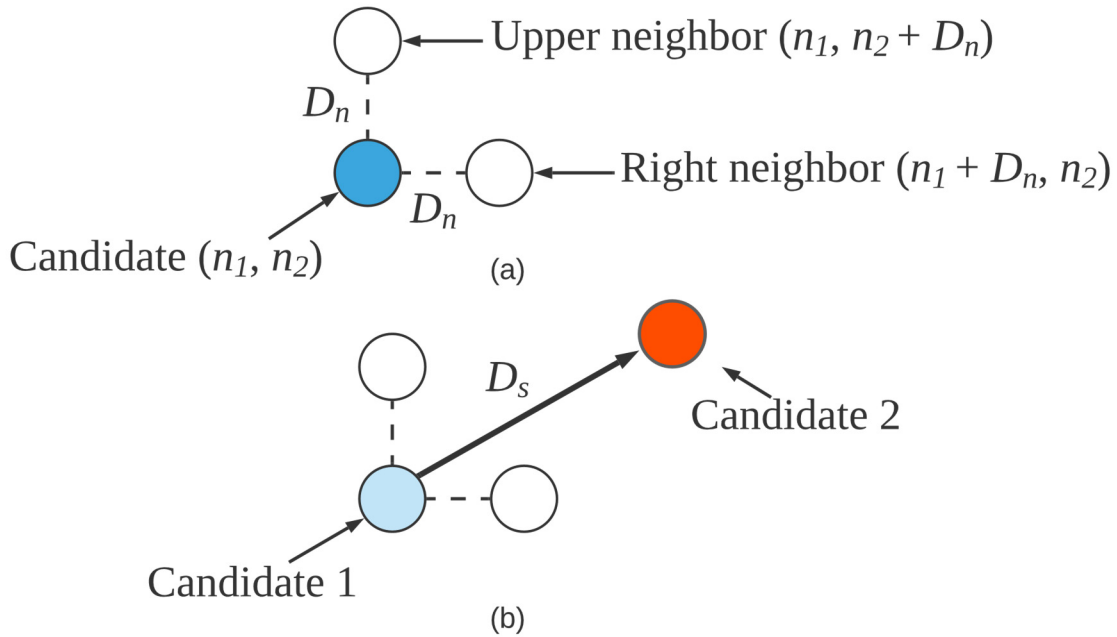


Figure 4.5 (a) Evaluation of neighboring (n_1, n_2) points, (b) location of the next candidate (n_1, n_2) point.

4.4.2 Dynamic Measurement Window

4.4.2.1 *Impact of measurement window on search performance.* As discussed in Section 4.4.1, the average performance gradient search relies on a measurement window parameter N that dictates the number of measurements that are performed at each tested impedance. This parameter impacts the speed at which the algorithm can converge to *any* result, as well as how consistently the algorithm can converge to the *same* result. Additionally, the optimal measurement window is influenced by the current RFI environment and cannot be predetermined.

To investigate the effects of N on the search's behavior, multiple searches were performed under various RFI scenarios at 3.3 GHz for multiple values of N . For each combination of scenario and measurement window, 100 searches were run with starting locations uniformly distributed in a grid throughout the (n_1, n_2) plane.

For the first RFI scenario, the SDRadar is operating in the presence of a tone stepping through a 60 MHz range centered at 3.3 GHz. A spectrogram of this RFI pattern and resulting SDRadar transmit waveforms are shown in Figure 4.6. A load-pull of the average performance using a large measurement window ($N = 300$) is shown as the contours in Figure 4.7. The low values of output power near the top right of the plot are due to the high reflectivity of the impedance tuner in this (n_1, n_2) region.

Search results for this scenario using measurement windows of 15 and 40, as well as a traditional gradient search that does not account for the varying SDRadar center frequency and bandwidth ("Classic Search ($N = 1$)") are shown in Figures 4.7-4.9. Figure 4.8 presents a histogram depicting how many searches obtain final average power values within the bins along the horizontal axis. This plot shows that the standard

gradient search (which is not built to account for the change in transmit frequencies) fails to achieve large power values on multiple occasions, and it even fails to converge to a consistent, poorly performing impedance. Meanwhile, the average search consistently converges near the optimal impedance.

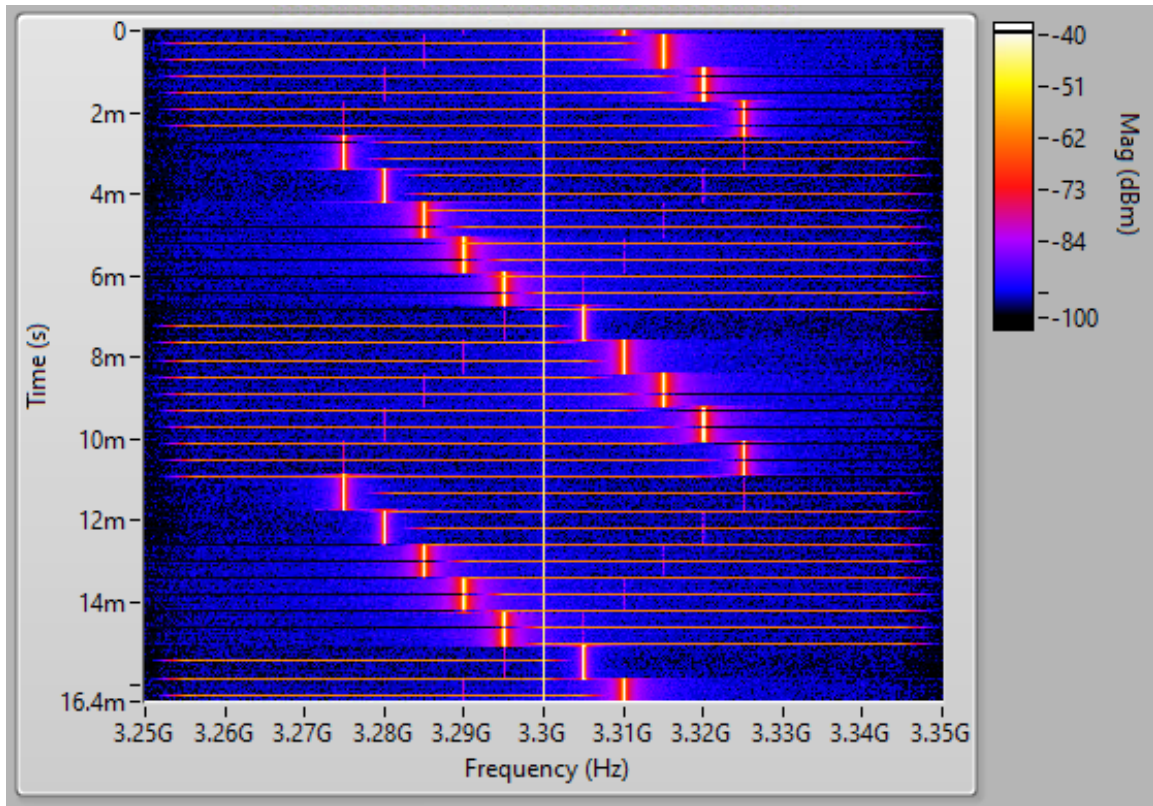


Figure 4.6. Waterfall plot displaying the encountered RFI (stepped tone) and selected SDRadar transmit waveforms (horizontal chirp pulses) over time (vertical axis) and frequency (horizontal axis).

This variation in convergence consistency is also evident in Figure 4.7, which shows the final impedance obtained by each search. Clearly, consistency of the final location is improved by the averaging technique, with the classic search's final impedances widely distributed throughout the search space. The inability of the classic

search to navigate towards the optimum is attributed to the gradient estimation errors introduced by the radar's varying transmit configuration, as previously discussed.

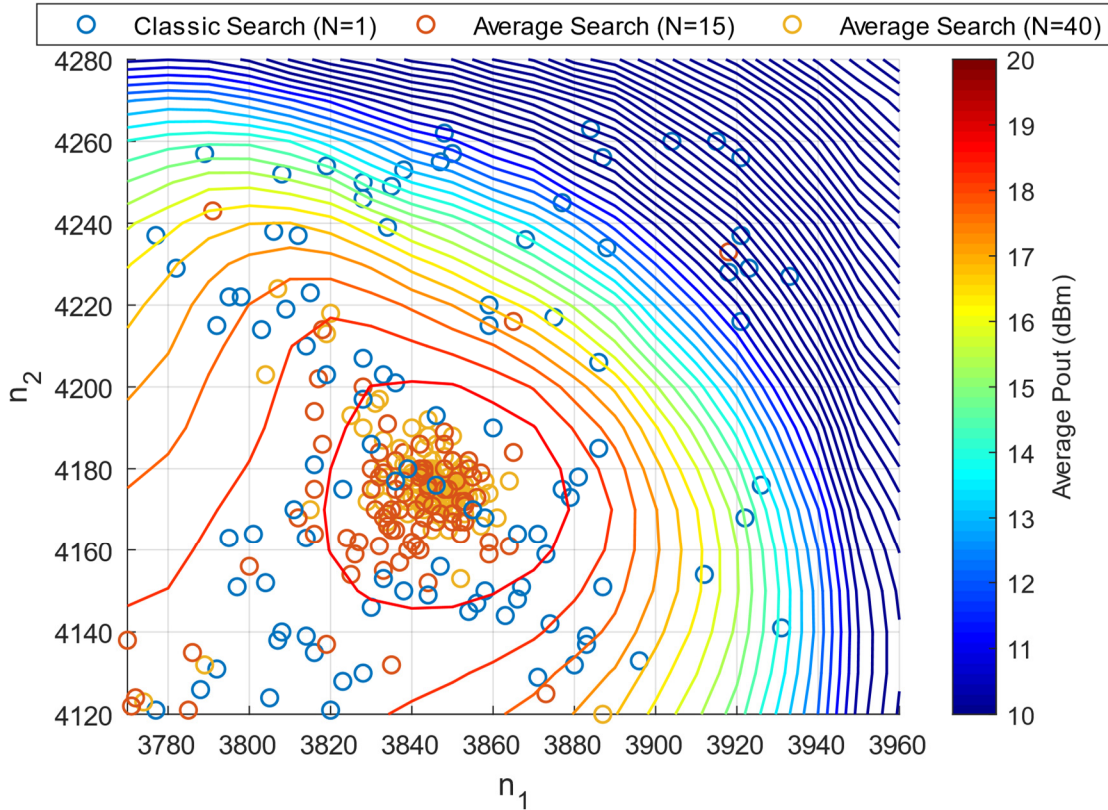


Figure 4.7. Final positions selected by the search algorithm with different measurement windows, shown with average power contours based on the transmit configurations used in Figure 4.6 and $N = 300$ for comparison. The maximum load-pulled average performance (without interpolation) is 19.38 dBm at $(n_1, n_2) = (3850, 4180)$. The classic search is unable to consistently navigate the power contours, resulting in unreliable convergence across the search space.

Figure 4.9 compares the search durations of the classic search and the $N = 15$ and $N = 40$ average performance searches. In addition to gradient estimation errors, the classic search also demonstrates early convergence due to the aggressive step size reductions that occur any time a new candidate impedance is evaluated at a transmit

configuration that provides worse performance than the configuration of the preceding candidate.

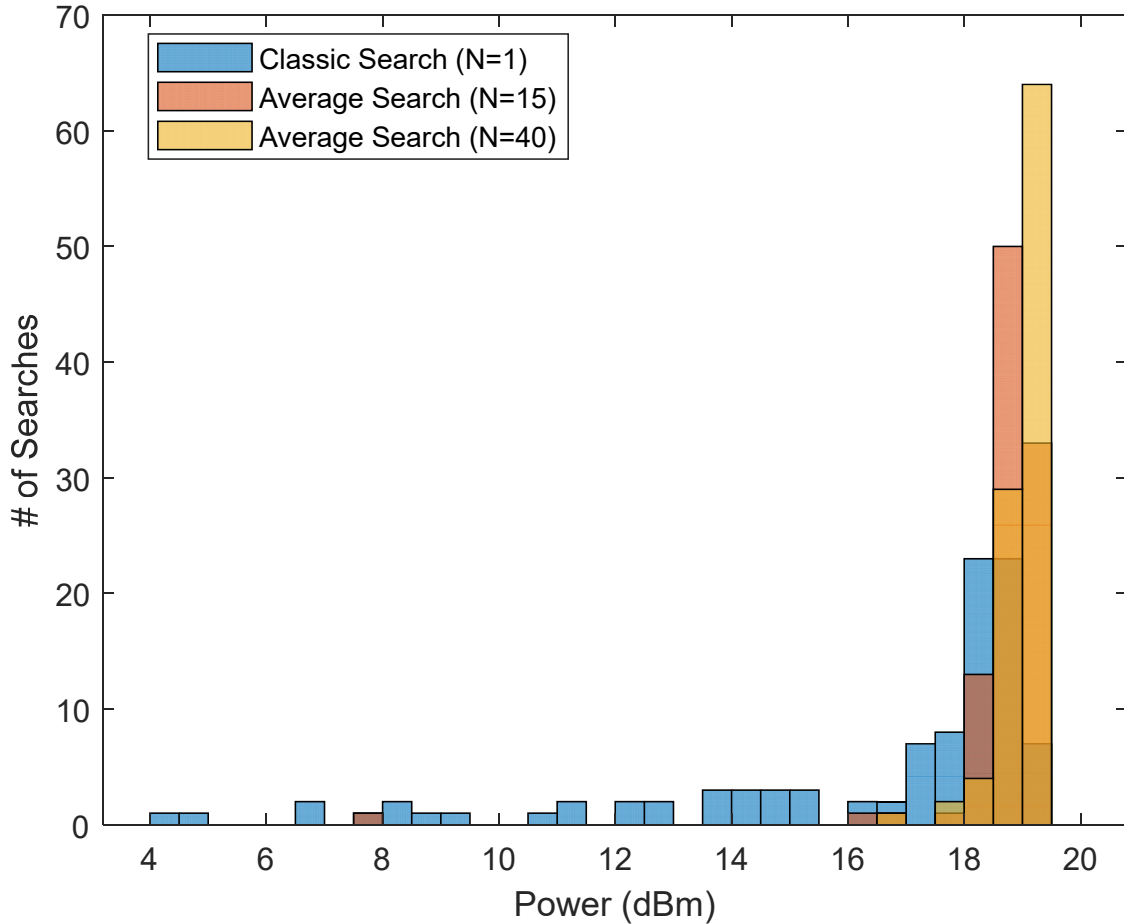


Figure 4.8. Final achieved average RF output power for the classic gradient search, average performance search with $N = 15$, and average performance search with $N = 40$ for the scenario of Figure 4.6. The classic approach is unable to reliably find the optimum performance, with the search convergence criteria quickly being triggered by inconsistencies during candidate point comparisons.

Meanwhile, the average search with $N = 15$ was found to require long convergence times in many cases. This is because the small value of N does not permit successful gradient calculations at many transmit configurations, which in turn results in repeated re-measurements of gradient points to obtain enough information for an average

performance gradient calculation. Additionally, even when a gradient estimate is completed, the underlying average power measurements may not be representative of the true average performance, as transmit configurations that were not observed at all of the required impedances cannot be included in the averaging process, as mentioned during the discussion of (4.4) and (4.5). This can cause the search to step away from the true optimum or traverse the search space in a scattered, inconsistent manner.

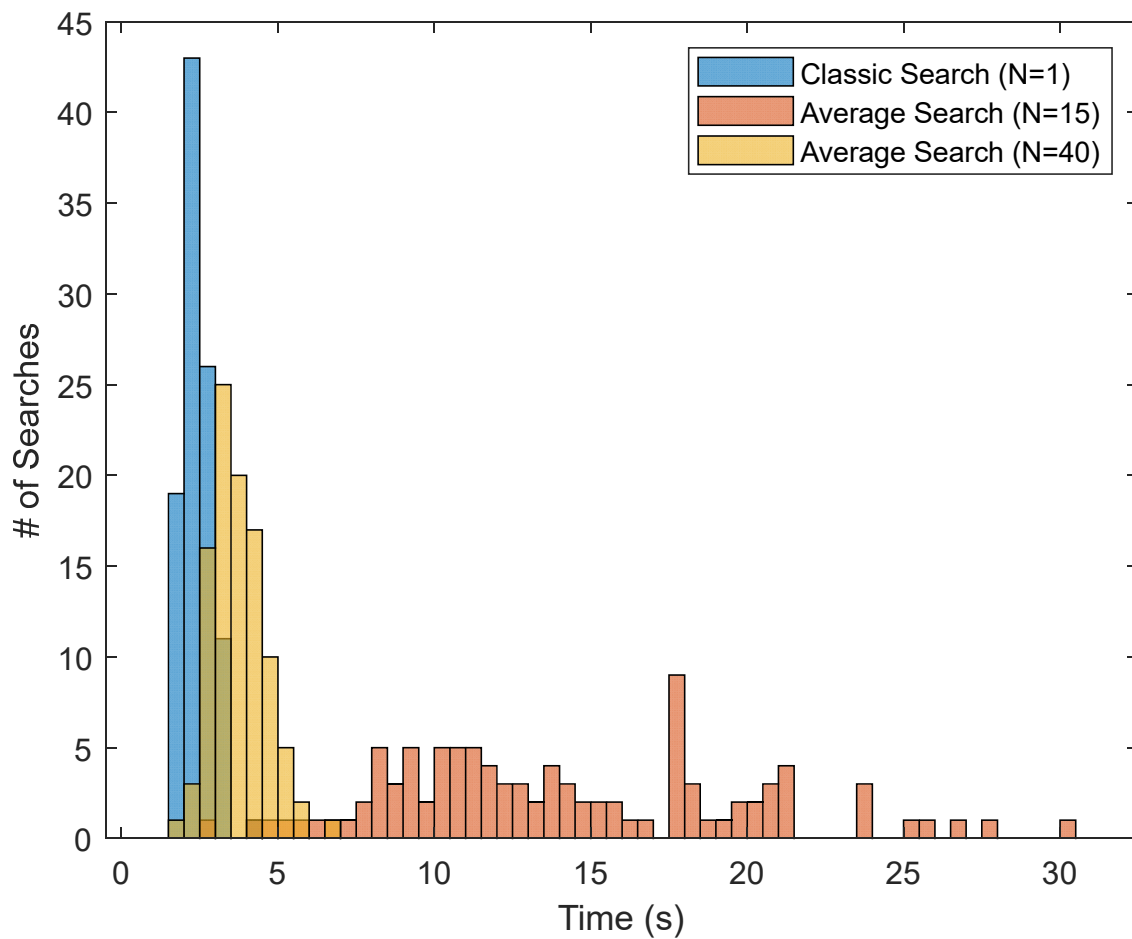


Figure 4.9. Search duration for the classic gradient search, average performance search with $N = 15$, and average performance search with $N = 40$ for the scenario of Figure 4.6. Using a measurement window N that is too small to capture the full selection of transmit configurations results in extremely large measurement times, as the search must repeatedly attempt to gather enough information for each gradient estimate.

These observations suggest the existence of a measurement window “sweet spot,” below which the search time increases dramatically while the convergence consistency declines, and above which the search time increases gradually with diminishing returns on convergence consistency. Once the measurement window is large enough to consistently encapsulate the typical cognitive radar behavior over subsequent measurement intervals, there is nothing to gain from increasing the measurement window.

This measurement window sweet spot can be located by correlating the search time with the number of discarded measurements for each gradient estimate (i.e., measurements associated with configurations that satisfy $M_{k,i} = 0$ for some i). Figure 4.10 shows that the search convergence time is minimized for the RFI scenario of Figure 4.6 when the percentage of measurements utilized by the gradient calculations reaches its peak. This ratio is defined by the equation:

$$U = \frac{1}{3N} \sum_{\kappa=1, i=1}^{K,3} M_{\kappa,i}, \quad (4.8)$$

where $3N$ is the total number of measurements, K is the number of usable configurations, and the summation provides the number of usable measurements. According to Figure 4.10, the search is most efficient for the scenario of Figure 4.6 when the minimum measurement utilization ratio over 100 trials reaches 95% at a measurement window near $N = 20$. This trend indicates that the percentage of measurements utilized by the gradient calculations can be used as a metric to adapt the measurement window in real-time during the search process.

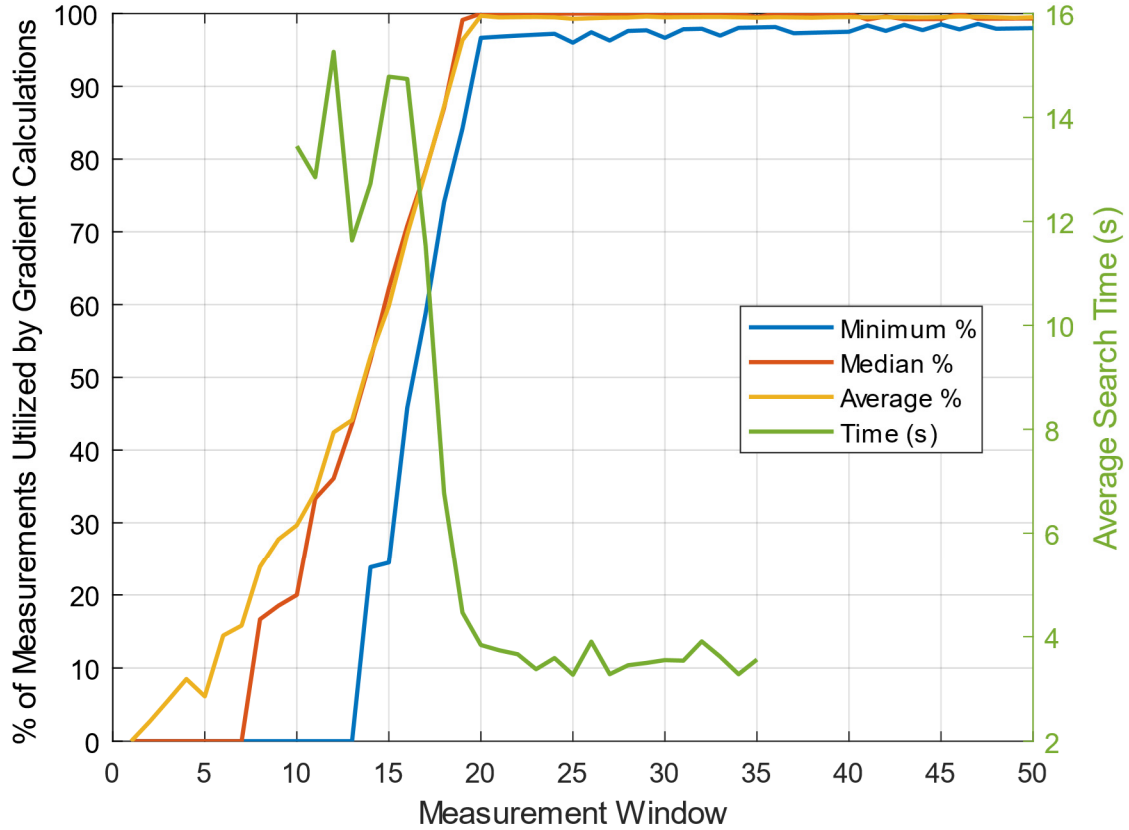


Figure 4.10. Correlation of measurement utilization ratio with search convergence time for the RFI scenario of Figure 4.6. The optimal measurement window for this RFI scenario is around 20, as the minimum utilization ratio begins to saturate around 95%.

Furthermore, additional trials show that the optimal measurement window varies with RFI. To demonstrate, consider the RFI scenario of Figure 4.11. In this situation, the optimal measurement window providing a minimum utilization ratio of 95% is near $N = 40$, with a corresponding minimization in search convergence time, as shown in Figure 4.12. It appears from these two examples that a utilization ratio of 95% is useful to provide convergence as efficiently and consistently as possible.

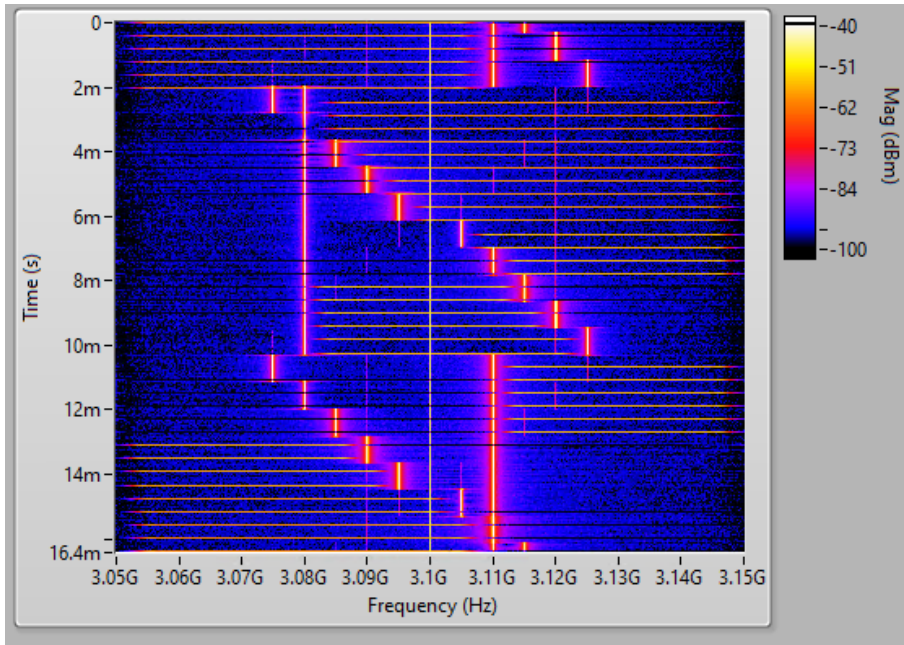


Figure 4.11. Waterfall plot displaying a second RFI scenario and selected SDRadar transmit waveforms over time (vertical axis) and frequency (horizontal axis). This RFI scenario is the scenario of Figure 4.6 with an additional tone hopping between two channels.

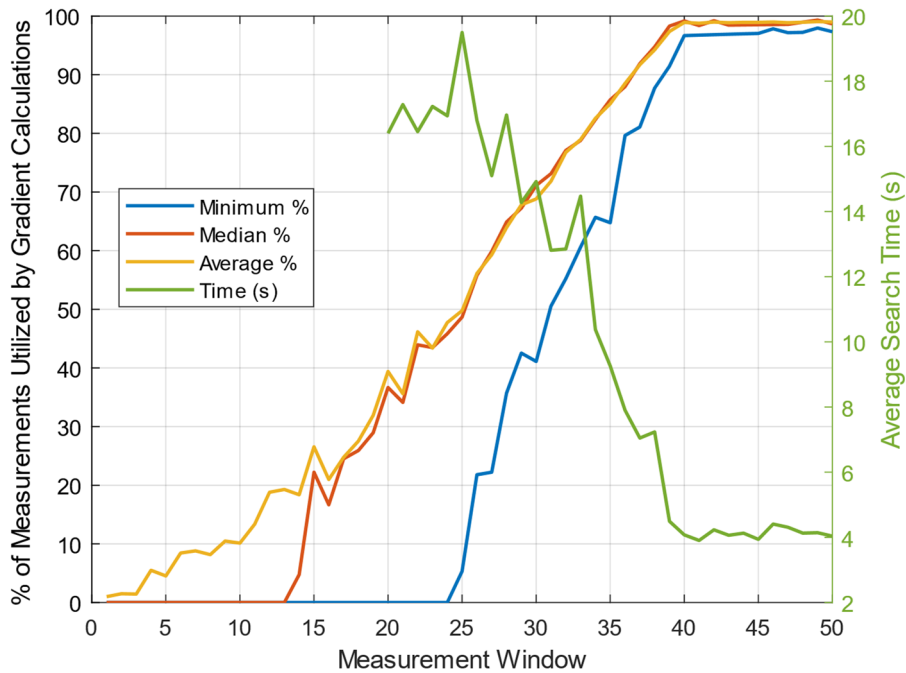


Figure 4.12. Correlation of measurement utilization ratio with search convergence time for the RFI scenario of Figure 4.11. The optimal measurement window for this RFI scenario is around 40, as the minimum utilization ratio begins to saturate near 95%.

4.4.2.2 Iterative optimization of dynamic measurement window. Given the variation in measurement utilization ratio for any fixed measurement window for different RFI scenarios, it is necessary to determine and adjust the measurement window over the course of the optimization process. For best results, the algorithm should seek to maintain a utilization ratio, U , between 93% and 97%. Preference is given to overshooting the optimal measurement window, rather than undershooting, as the increase in search time attributed to undershooting the optimal window is significantly higher than overshooting. As such, this chapter presents a measurement window selection algorithm inspired by the additive increase/multiplicative decrease approach of the Transmission Communication Protocol's (TCP) method of avoiding network congestion by adjusting its congestion window [76], which also incurs asymmetric costs on either side of the optimal window value [77].

The dynamic measurement window selection algorithm utilizes several parameters: the initial window size, the maximum iterative window increase, the target utilization ratio range, and thresholds placed on the number of allowed consecutive iterations that the utilization ratio is allowed to be outside of the target range before adjustments are made. If U is above the target range for more than the allowed period, N is decremented by one until the target utilization ratio is met. This gradual decrement helps to avoid severe performance costs associated with undershooting the target utilization ratio range. If U is below the target range for more than the allowed period, N is incremented at a faster rate, controlled by how far U is below 1 (100 percent), up to the maximum allowed increase. In the case, the new measurement window is described by the following equation:

$$N(n + 1) = N(n) + I_{max}(1 - U(n)), \quad (4.9)$$

where $N(n)$ is the measurement window at iteration n , I_{max} is the maximum allowed window increase, and $U(n)$ is the utilization ratio at iteration n , where $0 \leq U(n) \leq 1$, with 0 indicating all measurements were discarded and 1 indicating that no measurements were discarded. This fast increase allows quick attainment of a range where the optimization can make meaningful decisions about the system's performance.

It is required that the utilization ratio fall outside of the range for multiple consecutive iterations to filter out unnecessary adjustments that would be triggered by anomalies in the utilization ratio. An example of unnecessary adjustments would be adjustments caused by the sudden introduction of a new interferer mid-window whose effects on the cognitive radar's behavior would still be well described by the current window size had the interferer been present for the entire window.

A flowchart of the dynamic measurement window algorithm is included in Figure 4.13, and Table 4.2 describes the algorithm parameters.

Table 4.2. Dynamic Measurement Window Parameters

Parameter	Symbol	Value
Initial Window	N_{init}	10
Maximum Iterative Window Increase	I_{max}	30
Desired Measurement Utilization Range	--	[0.93, 0.97]
Allowed Consecutive Below-Range Iterations	C_B	3
Allowed Consecutive Above-Range Iterations	C_A	3

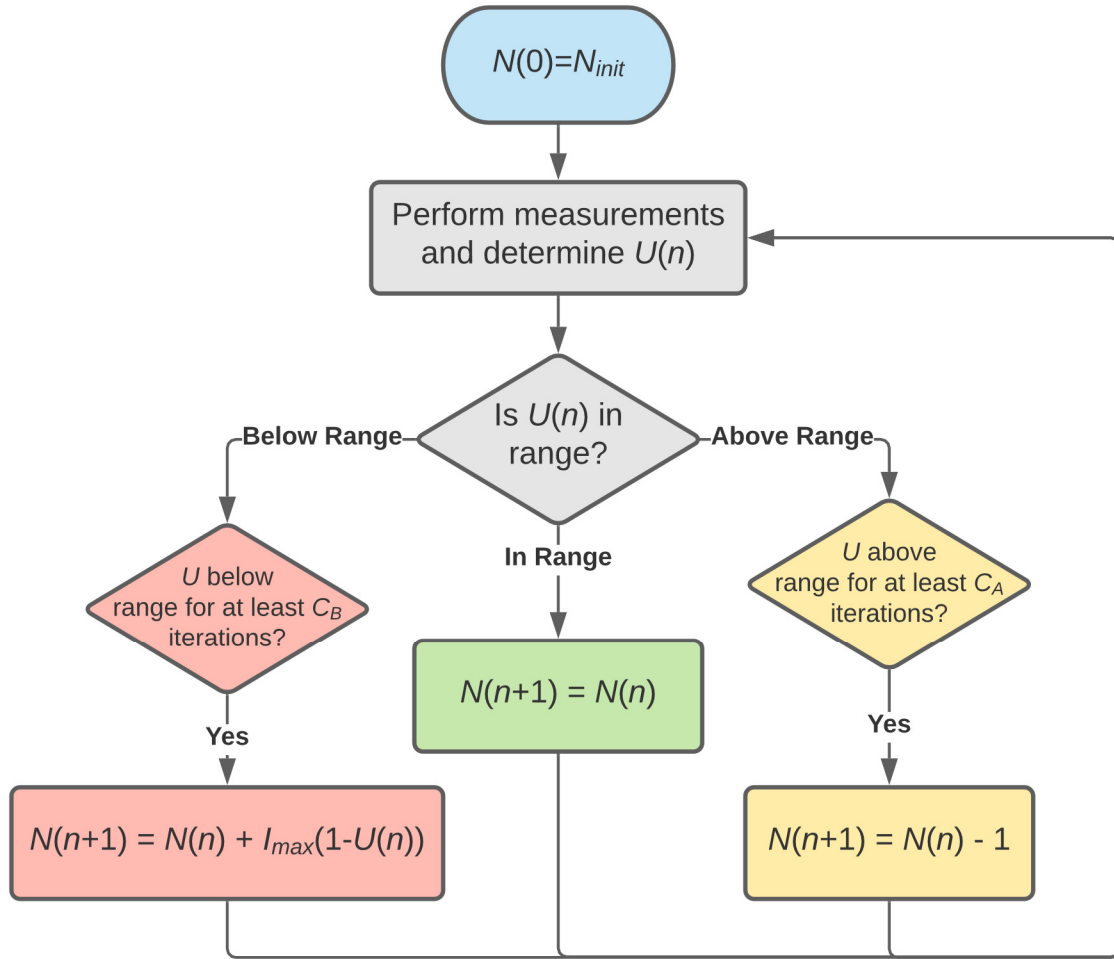


Figure 4.13. Flowchart of the dynamic measurement window selection process.

4.4.3 Step Size Convergence

In typical gradient algorithms, including the ancestors of the method of Section 4.4.1 [24, 55, 64-65, 68, 72], instances where a performance reduction is observed after stepping to the next candidate point cause the step size parameter D_s to be decreased. The assumption underlying this action is that the search has stepped over a point with improved performance; therefore, the optimum lies somewhere between the previous and current candidate points. The remainder of the algorithm functions similar to a binary search, narrowing in on the actual optimal point until the step size falls below a preset

convergence threshold: the resolution distance parameter D_r . This assumption results in desired behavior if the optimal impedance is stationary over time.

However, this stationarity assumption may be violated while optimizing impedance of a cognitive radar transmitter that is quickly changing its transmit configuration. For instance, the radar's configuration may change after the search algorithm has begun to decrement its step size, resulting in a different optimal impedance not necessarily near the current, active impedance. In this situation, the algorithm must increase its step size to quickly reach the new optimum. While momentum-based methods such as classical momentum [78] and Nesterov acceleration [79] are often used in gradient applications for similar effect [80], their benefit for time-varying environments is less certain [81].

Instead, instances where the optimal impedance may have moved can be detected by monitoring how many consecutive steps with improved performance are made after a step size reduction. This trend provides a sense of *performance* momentum, rather than the *trajectory* momentum of other approaches. Assuming halved step sizes, if more than two consecutive steps observe improved performance, then it is expected that the optimal point no longer lies in a region that has been overstepped. In this case, the step size can be doubled. For quick recovery, this doubling action can be repeated until a decrease in performance is observed (indicating overstep and a need to halve the step size) or the maximum allowed step size is reached. To determine search convergence and end the search, the existing minimum step-size threshold technique of [24, 55, 64-65, 68, 72] is used. Parameters related to step size convergence are included in Table 4.3.

Table 4.3. Step Size Convergence Parameters

Parameter	Symbol	Value
Resolution Distance	D_r	5
Maximum Step Size	--	100
Allowed Consecutive Performance Improvements	--	2
Allowed Consecutive Performance Declines	--	0

Note that comparing the average performance between candidate points has the same transmit configuration observation requirements as gradient estimations. That is, at least one transmit configuration must have been observed at both candidate points in order to make a valid comparison. In instances where no valid comparison can be made, the record of consecutive performance improvements and the current step size from the previous step are maintained.

4.4.4 Cognitive Radar Behavior Transition Detection

Once the search algorithm converges, it is necessary to continue monitoring the cognitive radar's behavior for any changes (such as a change in utilized transmit frequency bands) that may appreciably impact the potential performance, warranting re-optimization of the load impedance. As discussed earlier in Section 4.3.2, the EMD is used to quantify the amount of change in the cognitive radar's chosen transmit frequencies over time by producing transmit frequency probability distributions from the transmitted waveforms and evaluating the distance between these distributions.

For demonstration in this chapter, it is desired that an optimization will always be performed when more than 0.5 dB of additional output power is available. Changes in RFI that result in the current impedance obtaining an output power of no worse than 0.5 dB less than the new (unknown) optimum may or may not be subject to optimization.

To determine the EMD threshold that produces this behavior, a selection of 17 SDRadar waveforms distributions (listed in Table 4.4) were optimized, with each chosen to provide a representative sample of the possible SDRadar transmit waveforms. The optimum power and corresponding impedance for each waveform was then determined, and the performance of each waveform’s optimal impedance was evaluated for all other waveforms. In addition, the EMD between each pairing of waveforms was calculated.

Table 4.4. SDRadar EMD Test Waveform Characteristics

Center Frequency (GHz)	Bandwidth (MHz)
3.2105	21
3.2175	35
3.2225	45
3.28	31
3.285	45
3.286	22
3.29	55
3.3	50
3.3	35
3.3	25
3.1	55
3.14	22
3.315	45
3.32	31
3.375	50
3.3825	35
3.3895	21

The footprint of a histogram relating EMD to differences in the performance of optimal impedances is shown in Figure 4.14. Based on the results of Figure 4.14, an EMD threshold of 0.1 ensures that opportunities to obtain more than 0.5 dB of improvement in output power are never ignored (false negative rate of 0). Detailed detection characteristics for this threshold are listed in Table 4.5.

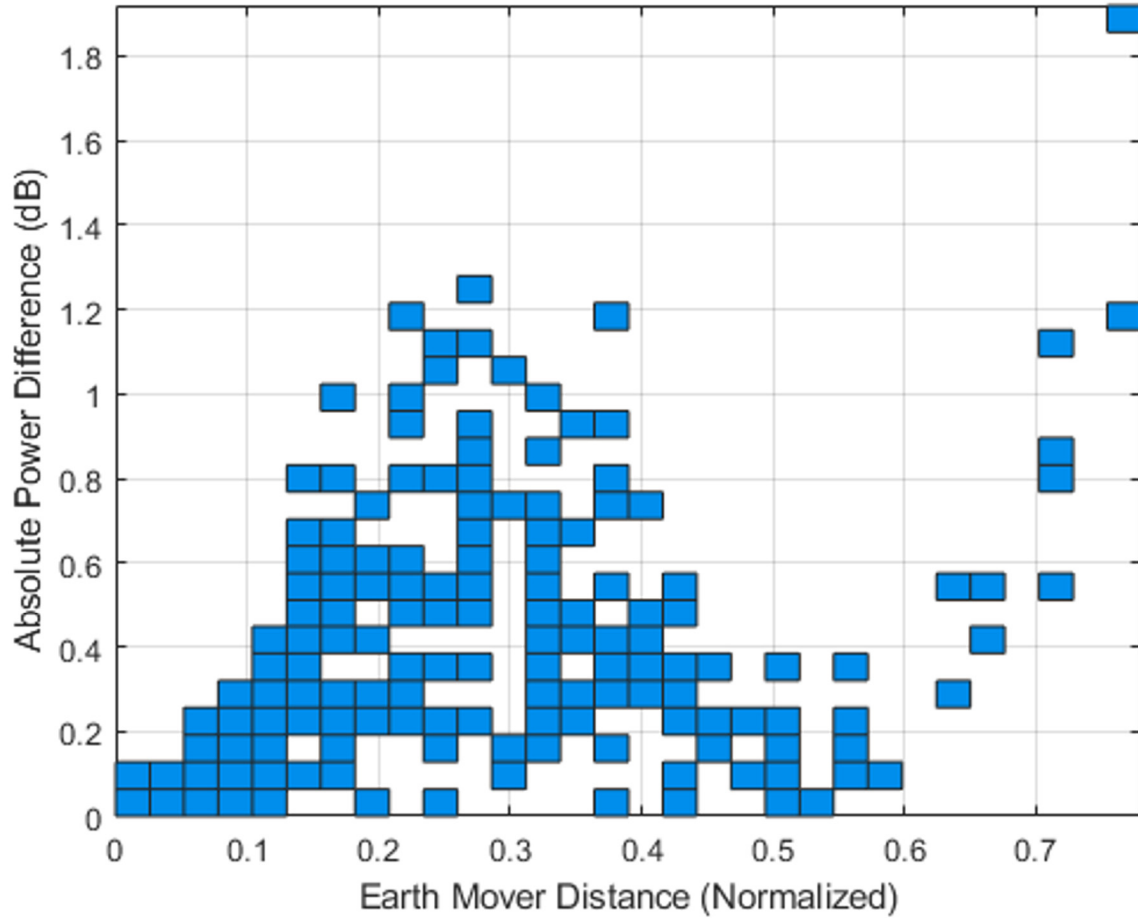


Figure 4.14. Relationship between the EMD of two waveforms and the output power improvement obtained by reoptimizing after a transition between two waveforms. © 2021, IEEE.

Table 4.5. 0.1 EMD Threshold Characteristics (289 Pairings)

Characteristic	Occurrences
False Negatives (Missed >0.5 dB Improvements)	0
False Positives (Utilized <0.5 dB Improvements)	138
True Negatives (Missed <0.5 dB Improvements)	67
True Positives (Utilized >0.5 dB Improvements)	84

Once the search converges, the transmit frequency distribution that was observed during the final measurement window of the search is used to represent the current “optimized” configuration. Afterwards, additional transmit frequency distributions are continually evaluated using the same measurement window, and the normalized EMD

between the current distribution and the optimized configuration is determined. If the current and optimized configurations have a normalized EMD greater than 0.1, then the search algorithm is reactivated to handle the new behavior. Unlike when starting the initial search process, the re-activated search begins with D_s that is one-fourth of the allowed maximum. However, the search can immediately increase the step size if needed. This approach allows the search to more quickly converge if the needed adjustment is small, or to quickly scale up the step size if it is evident that a larger adjustment is needed.

4.5 Experimental Results

4.5.1 Test Configuration

To demonstrate this optimization system, a randomly varying RFI environment was generated and presented to the cognitive radar. The possible RFI patterns were selected to produce a wide variety of distinct SDRadar transmissions (narrow/wideband, with varying offsets from the band center frequency) and optimal measurement windows within a 100 MHz bandwidth. The chosen RFI pattern was switched at random time intervals ranging from 0.5 to 4.5 s, according to the distribution of Figure 4.15. Additionally, the SDRadar operating band hopped across five different operating bands within the United States radar S-band allocation, triggered at randomly varying intervals uniformly distributed from 2 to 25 seconds.

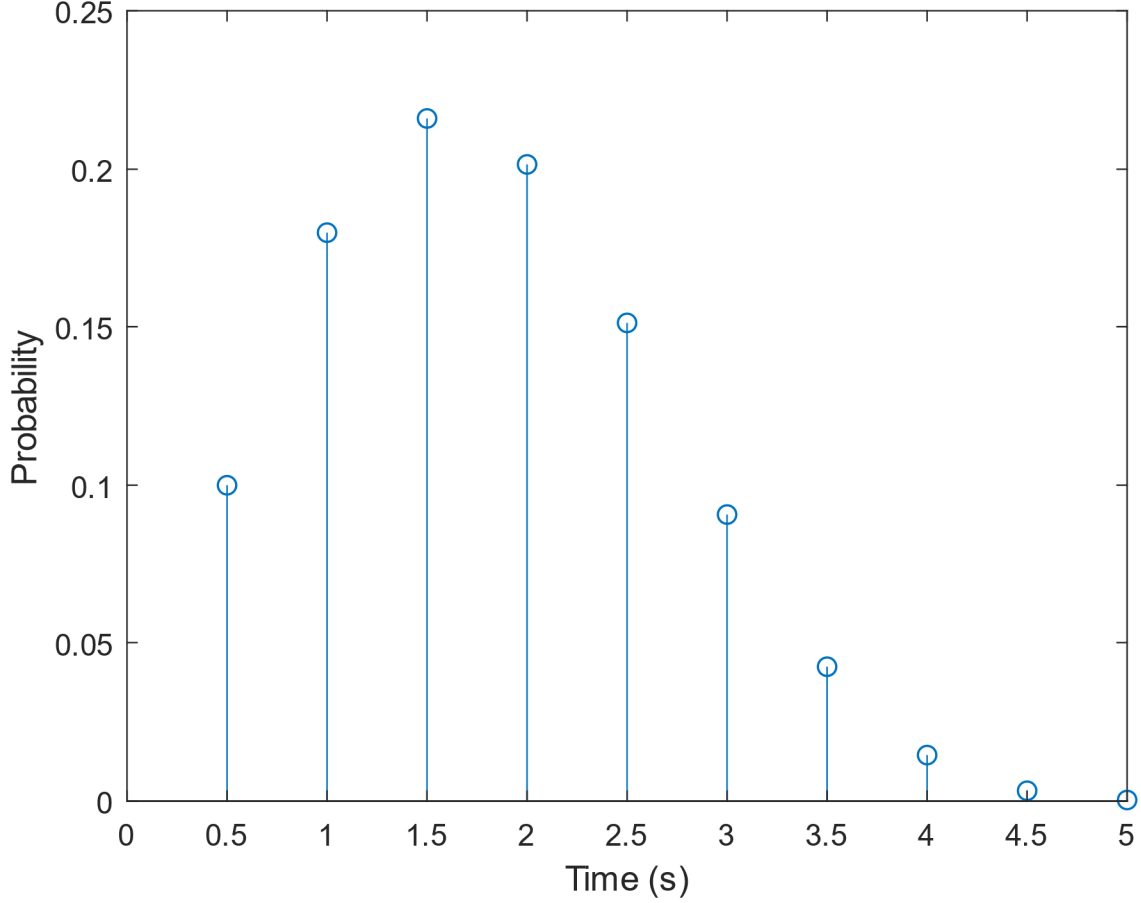


Figure 4.15. Probability distribution of the time interval between RFI pattern transitions, excluding transitions that result in an operating band change. This distribution arises from evaluating if the RFI pattern should be changed every 0.5 s, with the likelihood of a change occurring increasing each time the RFI pattern is not changed. The probability of an RFI change occurring begins at 10% and increases by 10 percentage points each time the RFI pattern is not adjusted, returning to 10% once a change occurs.

Prior to beginning the test, the optimal impedance was predetermined for each of the possible SDRadar operation bands with no RFI present and the radar utilizing the entire 100 MHz band. This was used to define a baseline performance metric:

$$P_{base}(t) = P(Z_{opt,full}(t_{prev}), t), \quad (4.10)$$

where $P(Z, t)$ is the radar output power obtained at time t using load impedance Z and

$Z_{opt,full}(t_{prev})$ is the pre-determined optimal impedance for the previous SDRadar

operation band when no RFI is present. This baseline metric reflects the output power that would be obtained using a fixed transmit amplifier optimized for the previous band. Note that all pre-determined information is used solely for evaluation purposes and is not available to the algorithm under test. The percent improvement in maximum detectable radar range over the baseline performance is computed as:

$$R(t) = \sqrt[4]{\frac{P(t)}{P_{base}(t)}}. \quad (4.11)$$

The optimal impedance was also predetermined for each of the allowed RFI patterns at each operation band. This information was used for post-assessment of algorithm performance through comparison with algorithm results.

4.5.2 Measurement Results

Figure 4.16 shows the SDRadar's chosen transmissions over the course of an experimental period lasting six minutes. These transmissions are represented as a frequency utilization percentage for each measurement window processed during the experiment; that is, frequencies that were used in every transmitted chirp within the algorithm's current measurement window are marked as 100% and frequencies that were never used in any chirp within the window are marked as 0%. This provides an indication of the frequencies that were being evaluated at each search operation (performance or EMD measurement).

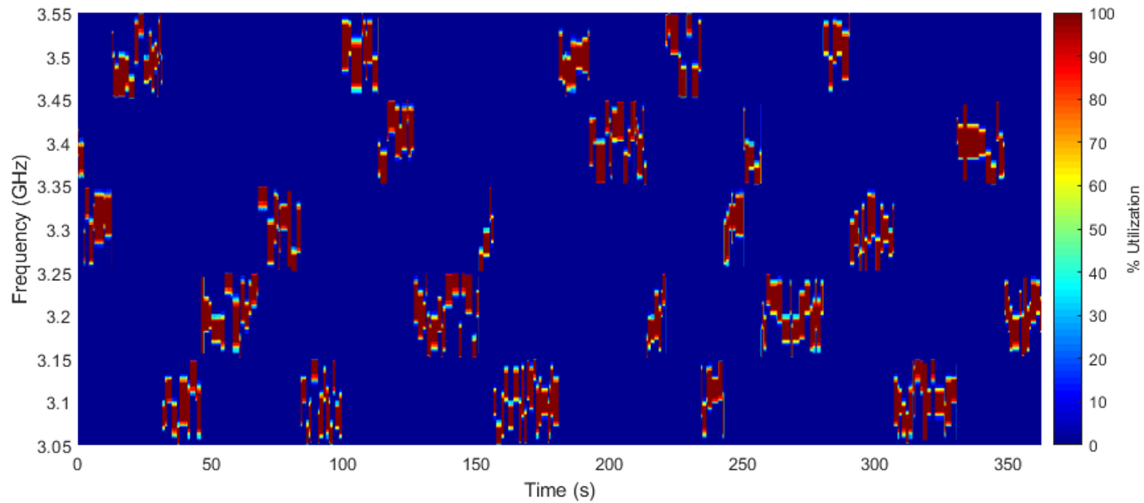


Figure 4.16. SDRadar transmit frequency utilization in response to time-varying RFI. Large jumps correspond to SDRadar operating band changes triggered by insufficient available transmit bandwidth, while smaller variations correspond to minor adaptations to RFI changes within the current operating band.

Figure 4.17 shows the improvement in maximum detectable radar range obtained by the algorithm in comparison to the baseline metric of (4.10), as calculated in (4.11), the maximum improvement that could be obtained, and time periods when the optimization algorithm was active or idle, using the EMD method discussed in Section 4.3.2 and 4.4.4. The EMD values found during the experiment (used to determine when the optimization should become active) are shown in Figure 4.18.

These measurements show that the algorithm is consistently able to find the optimal performance, with some time delay as the algorithm responds to RFI changes, resulting in an average realized performance improvement of 3.29% over the baseline, compared to the optimal improvement of 3.77% on average. The largest possible improvements are associated with transitions from an operating band of 3.5 GHz to 3.1 GHz, where an amplifier optimized for 3.5 GHz would perform quite poorly at 3.1 GHz.

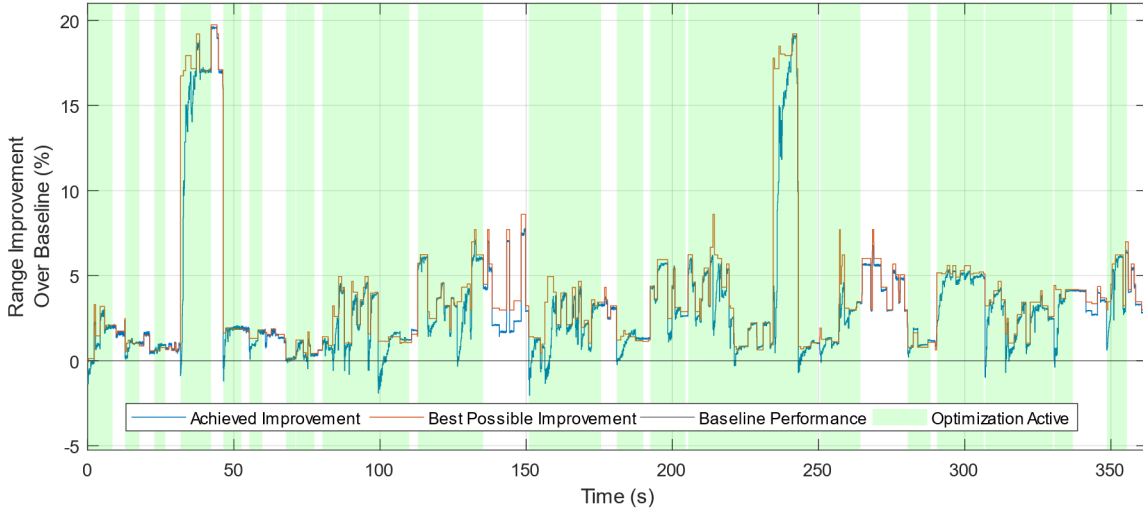


Figure 4.17. Percent increase in maximum detectable radar range obtained by the algorithm (blue) compared to the ideal result (orange). Regions shaded in green indicate periods when the average performance gradient search algorithm was active, while unshaded regions indicate periods when the search converged to a final impedance tuner setting and the optimization is waiting for a significant shift in the utilized frequencies before resuming the gradient search algorithm.

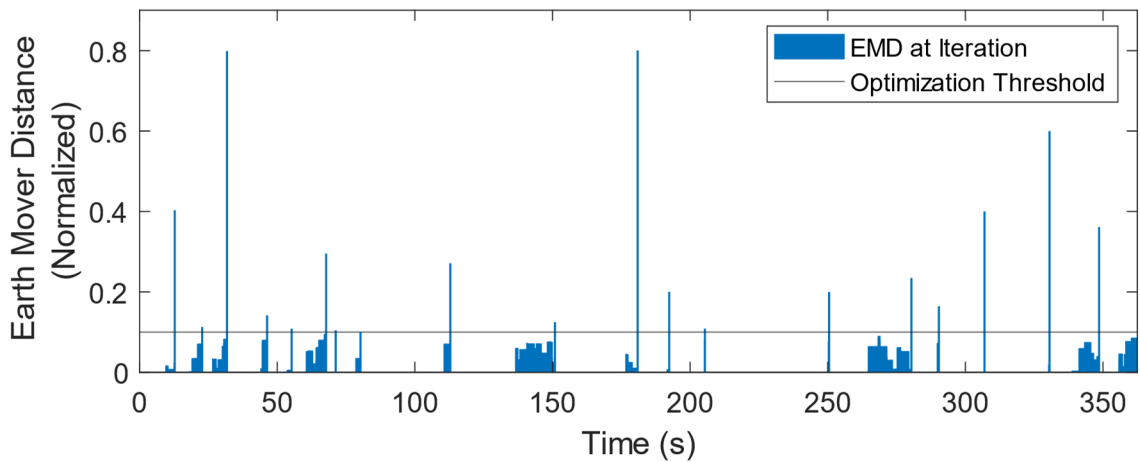


Figure 4.18. Normalized EMD between transmit frequency utilization at previous search convergence and current utilization. Instances where the distance crosses the threshold of 0.1 cause the average performance gradient search algorithm to resume from the current impedance.

In some instances, the algorithm appears to outperform the expected optimal performance, such as at 187 s. However, in these cases the output power observed by the

algorithm differs from the premeasured optimum performance by less than the margin of error that is observed when returning to a certain configuration (< 0.1 dB variation).

These variations are due to changes in temperature and minor inconsistencies in SDR performance when adapting to various frequent bands.

In other instances, the algorithm obtains performance below the expected baseline performance. The lesser deficits are also attributed to small power differences below the margin of error. Larger deficits are due to the impedance being optimized for the specific circumstances prior to the band hop, while the baseline metric assumes no RFI. In these cases, it is possible for the more specific optimized impedance to perform worse at the new operating band than the baseline impedance.

Finally, the measurement window used by the algorithm throughout the experiment is shown in Figure 4.19. These results demonstrate that the dynamic window algorithm correctly chooses sudden, significant window increases when necessary, along with gradual decreases when it is clear that the window can be reduced without degrading the search algorithm's performance.

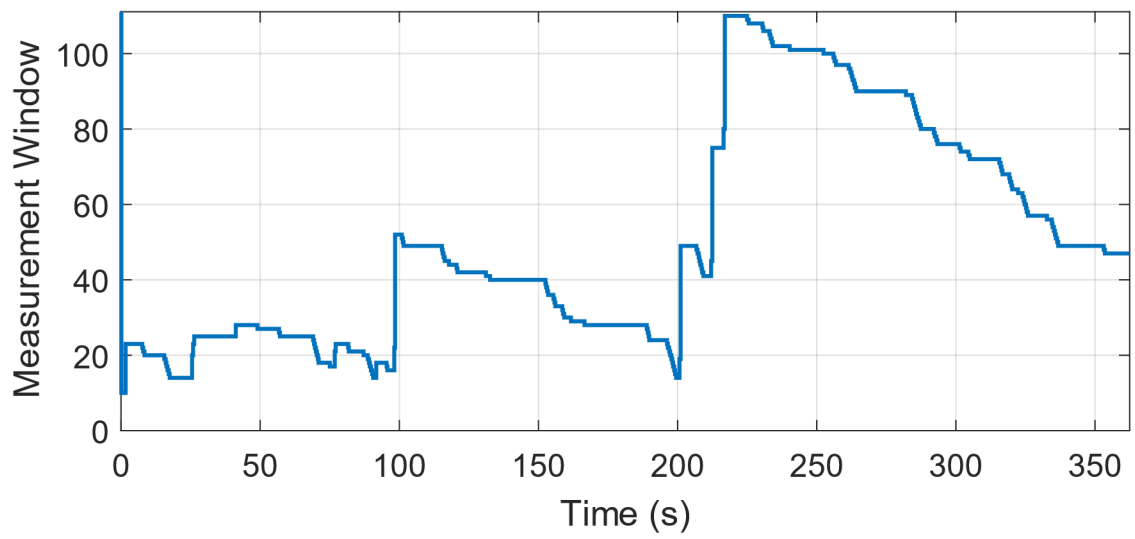


Figure 4.19. Dynamic measurement window versus time. The window adjusts throughout the experiment period in response to changes in RFI and the resulting behavior of the cognitive radar. Instances where the radar behavior transmits more consecutive unique pulses without repeat require larger measurement windows to accurately sample the radar's performance for optimization.

CHAPTER FIVE

Partial Load-Pull Extrapolation via Deep Image Completion

The work presented in this chapter on simulated linear devices has been published in:
[82] A. Egbert, A. Martone, C. Baylis, and R. J. Marks, "Partial Load-Pull Extrapolation Using Deep Image Completion," *2020 IEEE Texas Symposium on Wireless and Microwave Circuits and Systems (WMCS)*, 2020, pp. 1-5, doi: 10.1109/WMCS49442.2020.9172302. © 2020, IEEE.

5.1 Motivation

As discussed in Chapter Four, the average performance circuit optimization technique requires that a transmit configuration be observed at least once per impedance per iteration to be considered within the optimization step. In highly variable or complex spectral situations, the measurement window required to satisfy this requirement may be quite large. However, many transmit configurations have very similar performance contours with respect to impedance, such that they could be used interchangeably during the search process with negligible impact on the search's ability to converge to the optimal impedance.

In order to substitute configuration measurements during a search, enough data must first be obtained for the transmit configurations in question at similar impedances to determine if they are interchangeable. The comparison certainty required is relatively high, as false equivalences can severely impact the search's performance. This results in a similar data collection burden as needed for the search process itself and may not provide useful information for a long time while also requiring significant storage

resources to build up the comparison database. This database may also take a considerable amount of time to search, further slowing the optimization process.

Enabling comparison of transmit configurations across dissimilar impedances would greatly improve the benefit of configuration grouping, as the amount of data required to make similarity conclusions during system operation is greatly relaxed. Comparisons using data from disparate impedances necessitates extrapolating the performance of each configuration to the unknown impedances, establishing a common impedance set that can be compared. This operation is analogous to extrapolating a full set of load-pull contours from an incomplete dataset, as illustrated in Figure 5.1.

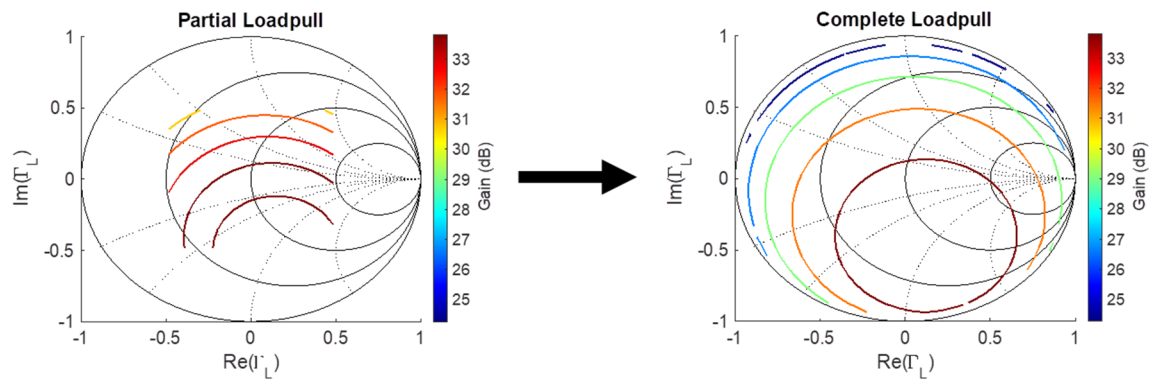


Figure 5.1. Illustration of partial load-pull extrapolation objective. Given the partial set of load-pull measurements (left), it is desired to produce the complete set of contours (right) without additional measurement.

If possible, the extra information provided by such an extrapolation has many other applications, including the selection of starting locations for search processes or regions of interest for dense load-pulls. For dense load-pulls, a common technique is used where consecutive load-pulls with increasing density are performed, utilizing the sparse understanding generated by previous iterations to select a region of focus for the next iteration [83]. For real-time circuit optimization techniques, the conjugate of the DUT's

output reflection coefficient is considered a good starting location [60]. Unless *a priori* knowledge of the DUT is available, all possible locations should be considered as equally likely to be the optimum, so beginning at the center of the Smith Chart minimizes the average expected distance to the device optimum. For search spaces where convexity, and by extension convergence, is not guaranteed, “Sarvin’s Method” of [24] has demonstrated the ability to select a good starting location by testing a few locations spread throughout the load tuner search space and choosing the best performing location, with the intention that the best performing point will be close enough to the optimum to ensure the search is able to converge. In all of these cases, load-pull extrapolation has potential to greatly reduce the number of impedances that must be evaluated, or greatly increase the quantity of information gained from the evaluated impedances.

Furthermore, load-pull extrapolation can be used as the primary circuit optimization mechanism without the need for an additional search process. In this approach, the predicted optimal impedances can guide the search, alternating between selecting regions of interest via extrapolation and acquiring new measurements in the region of interest. For efficient implementation, the specifics of this alternating process depend on the component reconfiguration period and the computational requirements of the adaptation algorithm.

This chapter introduces deep learning image completion as a mechanism for achieving the load-pull extrapolation goals of Figure 5.1. Image completion techniques in general have been previously demonstrated using more complicated datasets, including full-color photographs [84] and partial electron microscopy [85]. Additionally, the ability of neural networks to learn and extrapolate performance of an individual large-signal

microwave device has been previously demonstrated [86, 87], though [86] trains an individual network per device on partial load-pull data. This chapter builds upon these previously demonstrated capabilities and provides a method to extrapolate performance for microwave amplifiers in general from partial load-pull data without the need to retrain the underlying neural networks.

5.2 Extrapolation Method

To achieve the partial load-pull extrapolation goal of Figure 5.1, a gradient-based image completion technique is applied to a generative adversarial network (GAN) trained on known amplifier load-pull contours. The source of this data can be obtained from multiple sources, including linear and non-linear measurements or simulations; this work specifically uses only simulated, linear amplifiers for training (see Section 5.2.2 for more detail). GANs consist of two adversarial neural networks trained with opposing goals [88]. The first network (discriminator) is trained to classify instances of data as either belonging to some defined dataset or not belonging to the dataset. The second network (generator) is trained to utilize random input values to produce instances of data that are misclassified by the discriminator. These networks are trained in an alternating fashion to allow each to adapt to weaknesses in the other's behavior. More specifically, in this work the discriminator is trained to recognize if a given image depicts load-pull contours from the training set or from the generator network, being careful to not overfit the training data. Meanwhile, the generator is trained to produce images that the discriminator will classify as a valid set of load-pull contours. As both networks improve their performance over the training process, these objectives lead to a discriminator that can evaluate the validity of arbitrary load-pull contours and a generator that can produce valid load-pull

contours beyond those of the initial training dataset. The operation of these networks is illustrated in Figure 5.2.

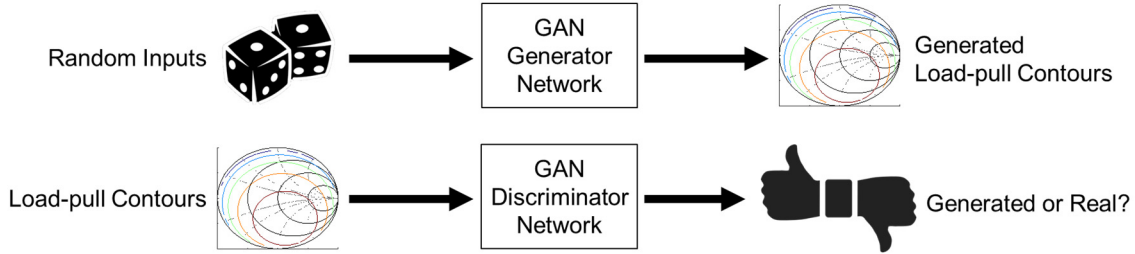


Figure 5.2. Illustration of the function of the generator and discriminator networks utilized within the generative adversarial network architecture used in this chapter.

Given a functional GAN, image completion can be performed by searching for an input to the generator that produces a result that closely agrees with the known portion of the image being completed. As the GAN is pre-trained prior to image completion, this approach provides a good basis for quickly evaluating an unknown device. This search process is illustrated in Figure 5.3 and discussed in more detail in Section 5.2.3.

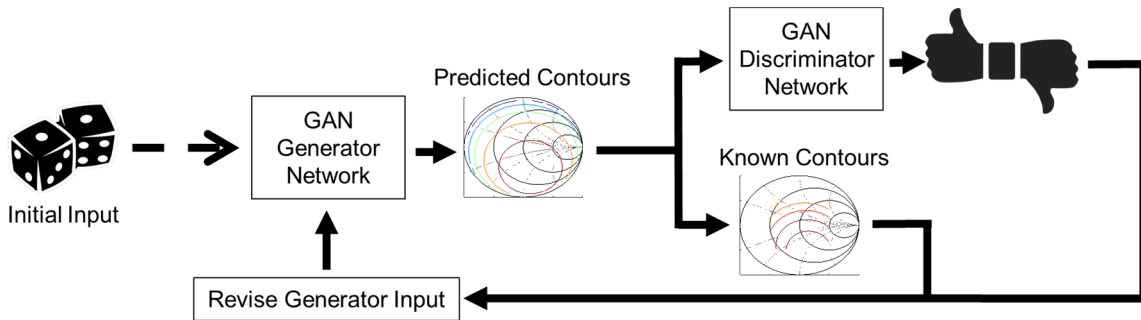


Figure 5.3. Illustration of the image completion search process used in this work. The input to the generator network is revised over time to produce load-pull contours that have good agreement with the known performance contours and present the appearance of a real load-pull dataset.

5.2.1 Implemented GAN Architecture

This chapter uses a variation of the traditional GAN architecture known as Wasserstein GAN (WGAN) [89]. The WGAN architecture uses the Wasserstein distance (equivalent to the Earth Mover Distance discussed in Section 4.3.2) as the loss metric when training the generator and critic (WGAN discriminator) networks. This distance method avoids the metric saturation that can occur when one of the networks performs too well (such as if the critic is never wrong, similar to the issues faced in Section 4.3.2 with significantly different frequency utilization distributions). Avoiding this saturation greatly improves the stability and robustness of the network training process by ensuring that the gradient calculations used to update the generator network do not vanish if the critic becomes too performant, and it helps prevent the generator network from only learning a few specific images capable of fooling the critic (mode collapse). The WGAN system used in this work is trained according to the approach presented by [84] utilizing gradient penalties (WGAN-GP) as opposed to the weight clipping methods of the initial WGAN architecture [89]. The implementation (including network layer topology) has been adapted from [90] for use with load-pull contour data. Figures 5.4 and 5.5 show illustrations of the resulting network structure for the generator and critic networks.

5.2.2 Training Data Generation and Measurement Preprocessing

The data used for this project is generated in MATLAB by simulating the output power contours for 100,000 randomly generated sets of amplifier S-Parameters. As such, these contours represent linear device performance. This approach is used in lieu of large-signal device behavior because of the need for a large dataset during training and the relative ease of generating S-Parameters compared to simulating non-linear models.

Datasets for large-signal operation could be produced by performing load-pull simulations using existing nonlinear device models across a variety of settings (frequency, bias conditions, input power, etc.); however, such an approach may not be necessary given the quality of the non-linear results shown in Section 5.4.2.

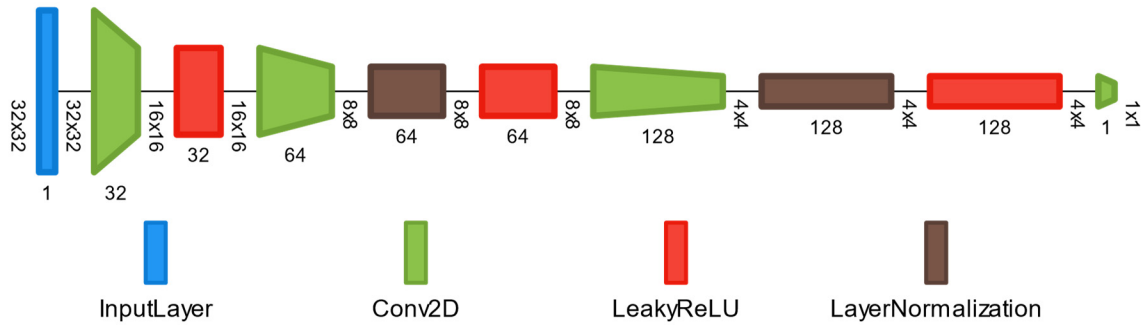


Figure 5.4. WGAN-GP network topology for load-pull critic network. This network operates on a 32x32 pixel greyscale load-pull image and produces a single value estimating how far the input image is from the learned set of valid load-pull images. Illustration synthesized using [91].

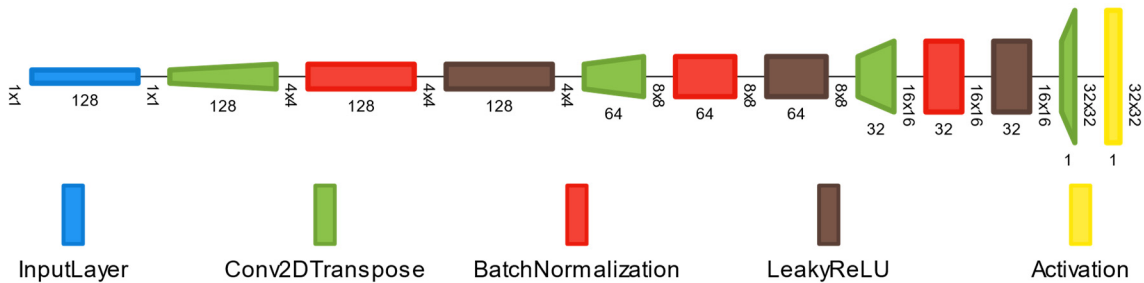


Figure 5.5. WGAN-GP network topology for load-pull generator network. This network operates on a 128-element initialization vector and produces a synthesized 32x32 pixel greyscale load-pull image. A hyperbolic tangent activation layer provides the final scaling of the network output. Illustration synthesized using [91].

Given a set of amplifier S-Parameters and source and load impedances, the linear amplifier output power can be calculated using the methods of Gonzalez [92]. The magnitude bounds for the randomly generated amplifier S-Parameters are included in Table 5.1. These bounds were selected to avoid generating potentially unstable

amplifiers. Only unconditionally stable amplifiers (as determined by the stability conditions $K > 1$ and $|\Delta| < 1$ defined in [92]) are used for training and evaluation to avoid unbounded performance values.

Table 5.1. Dataset S-Parameter Generation Bounds

S-Parameter	Bound (Linear Magnitude)
S_{11}	[0, 0.8]
S_{12}	[0.0001, 0.001]
S_{21}	[2, 20]
S_{22}	[0, 0.8]

The source impedance was fixed at 50Ω , and the load reflection coefficient's real and imaginary parts were varied over $[-1, 1]$ with 28 points each and uniform spacing, discarding values with $|\Gamma_L| > 1$.

The resulting dataset was pre-processed by standardizing to zero mean and unit variance and applying sigmoidal normalization with a hyperbolic tangent function as recommended by [93], such that

$$P'(n) = \frac{1 - e^{-P_s(n)}}{1 + e^{-P_s(n)}} = \tanh\left(\frac{P_s(n)}{2}\right) \quad (5.1)$$

$$P_s(n) = \frac{P(n) - \bar{P}}{\sigma_P}, \quad (5.2)$$

where $P'(n)$ are the normalized power samples and $P_s(n)$ are the power samples standardized from the mean \bar{P} and variance σ_P^2 of the original samples $P(n)$, represented in watts. Neglecting to apply the sigmoidal normalization results in the networks failing to predict optimized powers far from the mean observed power. This preprocessing can be inverted to recover predicted powers as

$$P_{pred}(n) = \left(2 \tanh^{-1}\left(P'_{pred}(n)\right) * \sigma_P\right) + \bar{P}. \quad (5.3)$$

For computational efficiency, each load-pull was rendered as 32×32 pixel greyscale images for use in the load-pull extrapolation system, matching the size of the input and output of the critic and generator networks.

5.2.3 Image Completion Process

The trained WGAN system is then leveraged for image completion using the techniques of Amos [94]. Although [94] utilizes a Deep Convolution GAN (DCGAN) architecture, the general image completion process readily translates to other GAN architectures, such as WGAN.

The goal of image completion is to find an input \hat{z} to the generator network $G()$ that produces an image $G(\hat{z})$ that is similar to the known partial image \hat{x} and fits the overall target dataset. To complete an image, a mask M is first specified that encodes what portion of the full image is provided by \hat{x} . The mask is specified as

$$M(n) = \begin{cases} 1, & \hat{x}(n) \text{ is valid} \\ 0, & \hat{x}(n) \text{ is invalid} \end{cases} \quad (5.4)$$

where n specifies pixels within the image. This mask is used in (5.5) to determine which portions of the generated image should be used when comparing the quality of the generated image to the provided partial image.

Two loss metrics are used to determine the quality of $G(\hat{z})$: contextual loss and perceptual loss. Contextual loss describes how similar the generated and partial images are to each other, and is defined as:

$$L_{context}(\hat{z}) = \|M * G(\hat{z}) - M * \hat{x}\|_1. \quad (5.5)$$

Perceptual loss describes how closely the generated image resembles members of the trained dataset according to the critic network $C()$, and is defined as:

$$L_{percept}(\hat{z}) = \log(1 - C(G(\hat{z}))). \quad (5.6)$$

These two losses are combined with a hyperparameter λ that weights the relative importance of the two metrics. (Amos [94] recommends $\lambda = 0.1$; this chapter instead uses $\lambda = 1$.) The final loss is then:

$$L(\hat{z}) = L_{context}(\hat{z}) + \lambda L_{percept}(\hat{z}) \quad (5.7)$$

with the optimization goal to find some \hat{z} that minimizes $L(\hat{z})$. The solution is found using the Adam optimization technique [95], with learning rate 0.01, $\beta_1 = 0.9$, $\beta_2 = 0.999$, and $\epsilon = 10^{-8}$. For the results of Section 5.3, each extrapolated load-pull contour set is the result of 1000 iterations of the Adam algorithm. Section 5.4 uses an early converge technique that looks for a minimum in the loss equation of (5.7) during the completion process, significantly reducing the time necessary for each extrapolation.

Note that the method of [94] combines the generated and partial images, utilizing the mask to remove part of the generated image and replace it with the original partial image. This chapter forgoes this step, using only the generated image as the final output.

5.3 Simulated Linear Load-Pull Extrapolation

The load-pull extrapolation system has been tested by presenting incomplete linear load-pulls of various sizes, generated with the same methodology as Section 5.2.2. Three sizes of incomplete data were selected such that known values were available for regions of the Smith Chart where $|\text{Re}(\Gamma_L), \text{Im}(\Gamma_L)| < \{0.5, 0.3, 0.1\}$, rounded down to the nearest pixel index. These are referred to as “0.5 Mask,” “0.3 Mask,” and “0.1 Mask” and correspond to partial load-pulls of 256, 81, and 9 values, respectively. Example extrapolated load-pulls are shown in Figures 5.6-8 along with the known data used as a basis for prediction and the true load-pull contours.

Each mask size was then tested with 100 different simulated amplifier load-pulls.

The prediction performance for each set is summarized in Table 5.2.

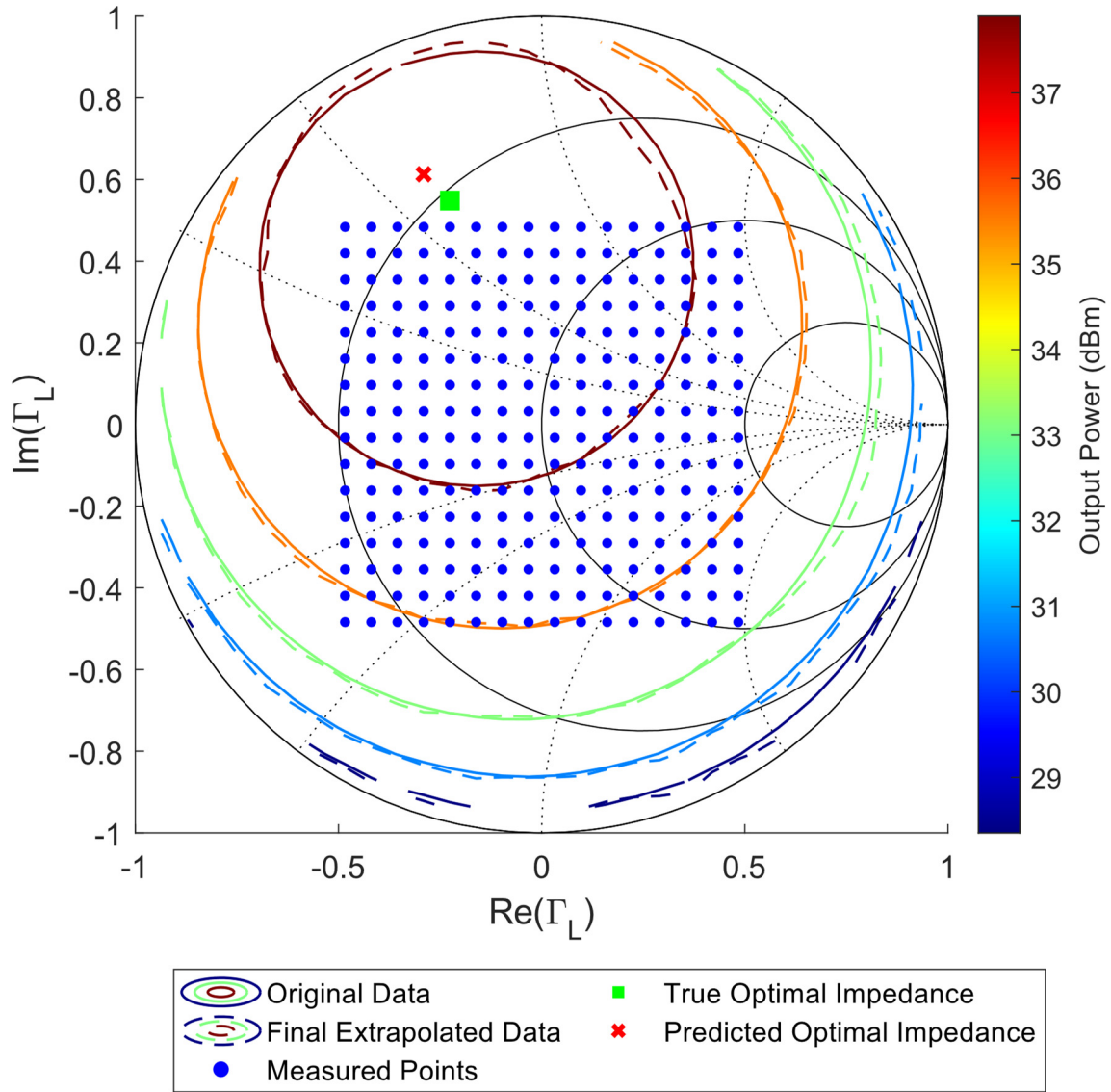


Figure 5.6. Original and predicted load-pull contours based on the 0.5 mask. Actual maximum gain is 40.28 dBm at $\Gamma_L = 0.59 \angle 112.4^\circ$. Predicted maximum gain is 40.65 dBm at $\Gamma_L = 0.68 \angle 115.3^\circ$.

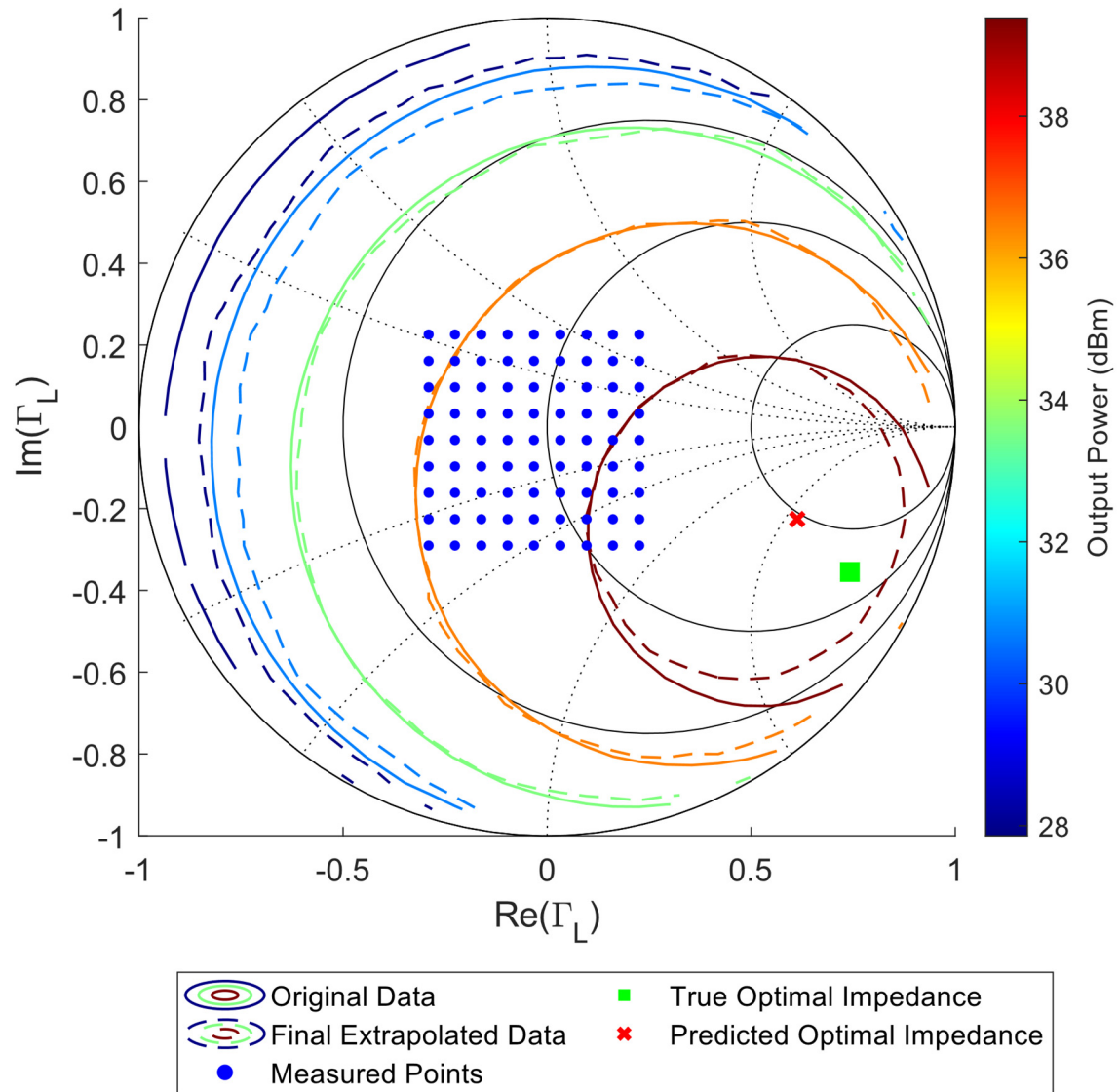


Figure 5.7. Original and predicted load-pull contours based on the 0.3 mask. Actual maximum power is 42.27 dBm at $\Gamma_L = 0.82\angle -25.6^\circ$. Predicted maximum power is 41.68 dBm at $\Gamma_L = 0.70\angle -20.2^\circ$.

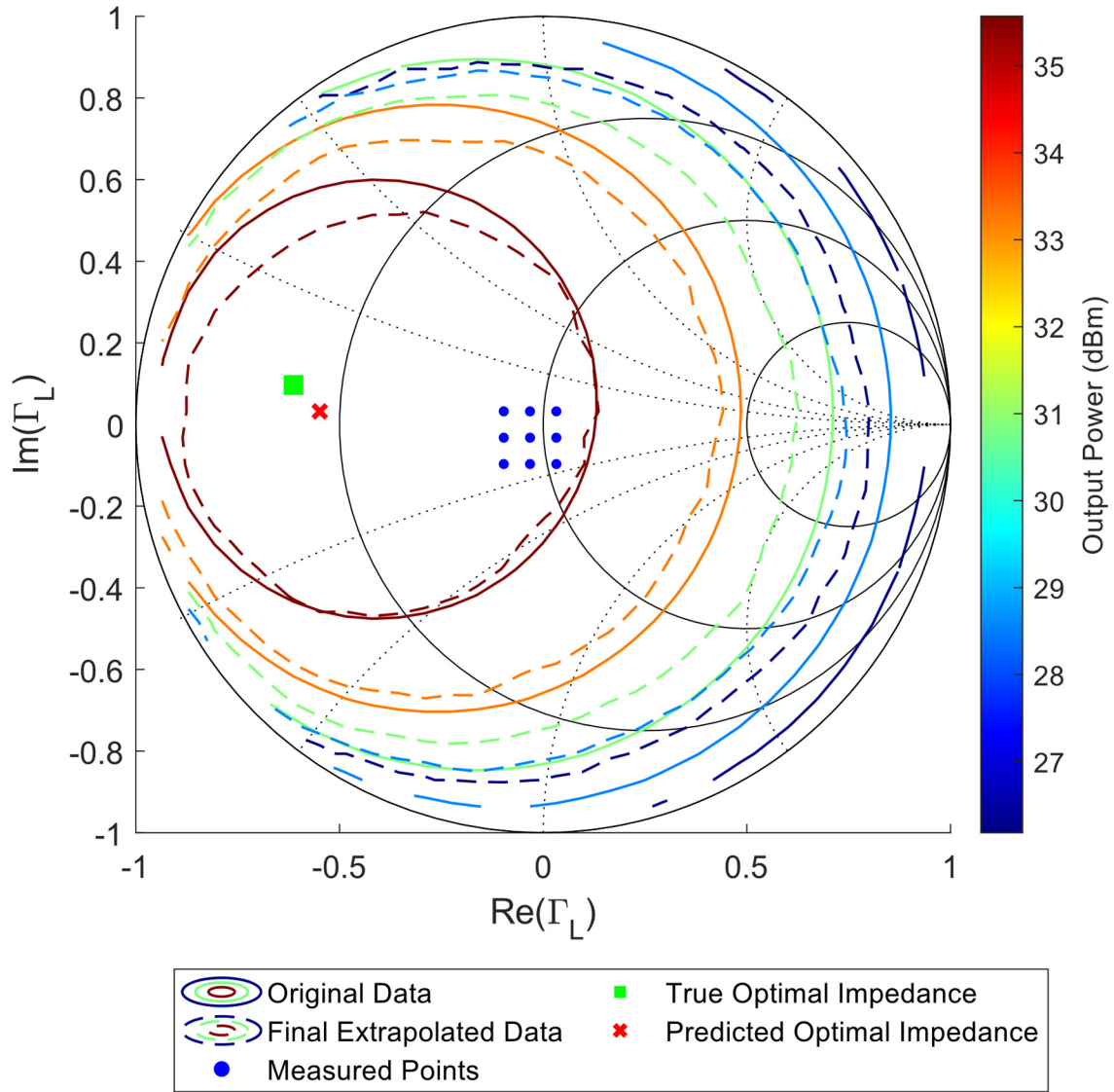


Figure 5.8. Original and predicted load-pull contours based on the 0.1 mask. Actual maximum power is 37.92 dBm at $\Gamma_L = 0.62\angle 171.0^\circ$. Predicted maximum power is 37.70 dBm at $\Gamma_L = 0.55\angle 176.6^\circ$.

Table 5.2. Linear Load-Pull Extrapolation Performance – Predicted Peak Statistics

Type of Peak Error Statistic	0.5 Mask	0.3 Mask	0.1 Mask
Power Error (Mean)	0.162 dB	0.453 dB	0.584 dB
Power Error (Median)	0.092 dB	0.240 dB	0.401 dB
Optimal Γ_L Error (Mean)	0.074	0.114	0.186
Optimal Γ_L Error (Median)	0.065	0.091	0.144

As expected, the extrapolation system performs better on average when given a larger initial load-pull sample (0.5 Mask). However, it still performs remarkably well even when given only nine measurements (0.1 Mask) as a prediction basis. Performance of optimum Γ_L predictions appears to encounter diminishing returns with increased sample size. This is likely an effect of confining Γ_L to the discrete 32×32 measurement grid used for evaluation as opposed to interpolating to a more precise maximum location with a finer grid.

5.4 Measured Non-Linear Device Load-Pull Extrapolation

The load-pull extrapolation technique of Section 5.2 has also been tested and demonstrated under measurement using the Skyworks 65017-70LF InGaP packaged amplifier with a bias voltage of 7 V. For each frequency under test, the Skyworks amplifier was power swept with a 50Ω load impedance to find the 3 dB compression input power; these 3 dB compression powers are used for all the results in this section. For this device, it is necessary to offset the measured powers by 20 dB to place them in the expected range for the image completion networks. In the event this offset is unknown for a device, it can be learned on the fly as part of the measurement process, offsetting the measured powers to lie within the expected range. All image completions in this section are run using a computer with an NVIDIA GeForce RTX 2070 Super GPU, AMD Ryzen 3700X CPU, and 32 GB of DDR4-3200 RAM, with an average image completion time of 1.1 seconds. Section 5.4.1 presents a circuit optimization technique that can be used in place of a traditional gradient peak-search algorithm, such as [72]. Section 5.4.2 presents a detailed look at the quality of the load-pull extrapolations performed as part of the optimizations shown in Section 5.4.1.

5.4.1 Circuit Optimization via Load-Pull Extrapolation

5.4.1.1 *Iterative Extrapolation Algorithm.* The general process flow for a circuit optimization algorithm using only load-pull extrapolation to drive exploration of the search space is shown in Figure 5.9. For each of the given steps in the algorithm, different variations are possible.

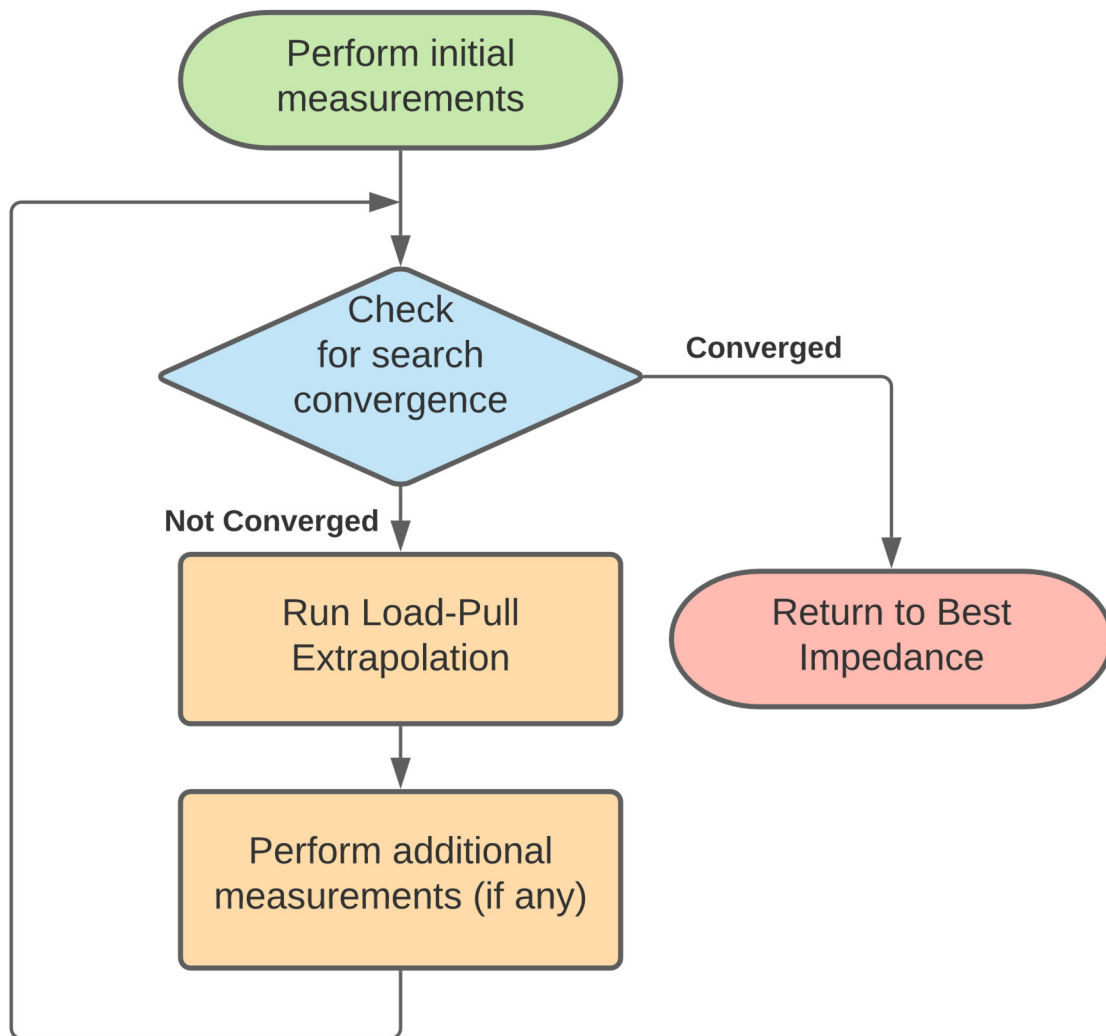


Figure 5.9. Generic process for circuit optimization using load-pull extrapolation. Variations on the algorithm are possible by changing how the initial and subsequent measurement points are selected based on extrapolation results and by changing the convergence criteria.

The primary algorithm used in this chapter is built on a simple “maximum addition” technique, where the best predicted impedance from the previous load-pull extrapolation is chosen for measurement and its performance added to the dataset used for the next extrapolation. The initial point is chosen at random from one of the four pixels closest to 50Ω , and the search converges when the most recently predicted best impedance has already been evaluated during a previous iteration. If applied to a frequency hopping context, the current system impedance could be used as the initial point instead of tuning near 50Ω .

This maximum addition technique is well suited for systems where the time cost of performing a load-pull extrapolation is low relative to the time required to tune to and evaluate some impedance. However, if this situation is reversed (i.e., it is faster to tune and measure than perform extrapolations), it may be beneficial to evaluate multiple impedances per extrapolation. For example, the eight pixels surrounding a predicted optimal impedance could also be evaluated in addition to the optimal impedance. This also permits a more sophisticated convergence check that looks for the presence of some local maximum performance; given the convex nature of output power contours on the Smith Chart, any local maximum is guaranteed to provide the best performance and no additional search is required.

5.4.1.2 Optimization Results. This circuit optimization technique has been tested with the traditional load-pull system of Section 3.5 at 21 frequencies between 2 and 4 GHz, spaced at 100 MHz intervals. 50 searches were performed at each frequency (total of 1050 searches). The results from several example searches at various frequencies are shown in Figures 5.10 through 5.12.

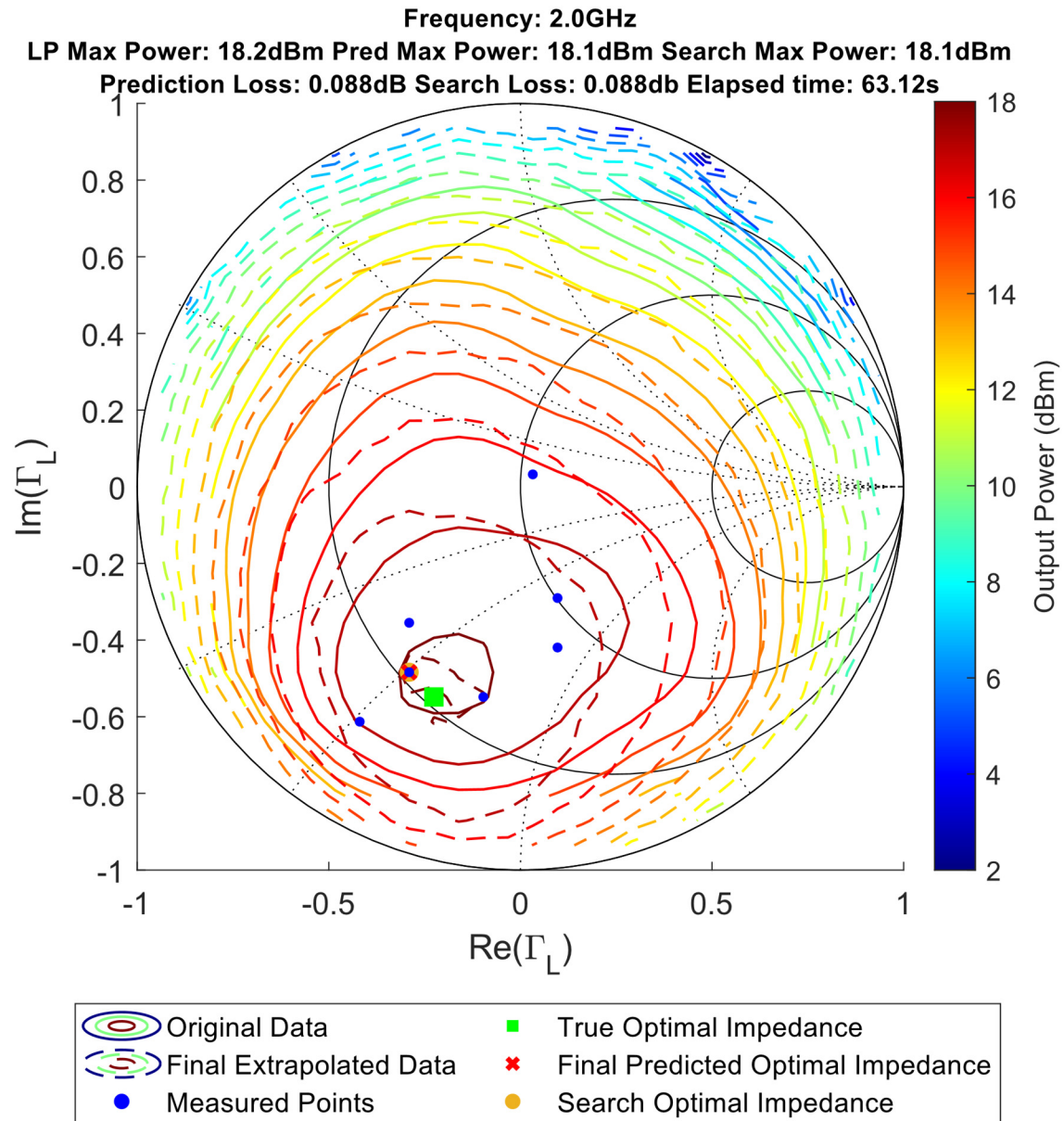


Figure 5.10. Results for a single run of the load-pull extrapolation circuit optimization algorithm at 2 GHz. This search evaluated 7 impedances in 63 seconds, converging to an impedance 1 pixel up and to the left of the true optimal impedance, with an associated performance loss of 0.09 dB.

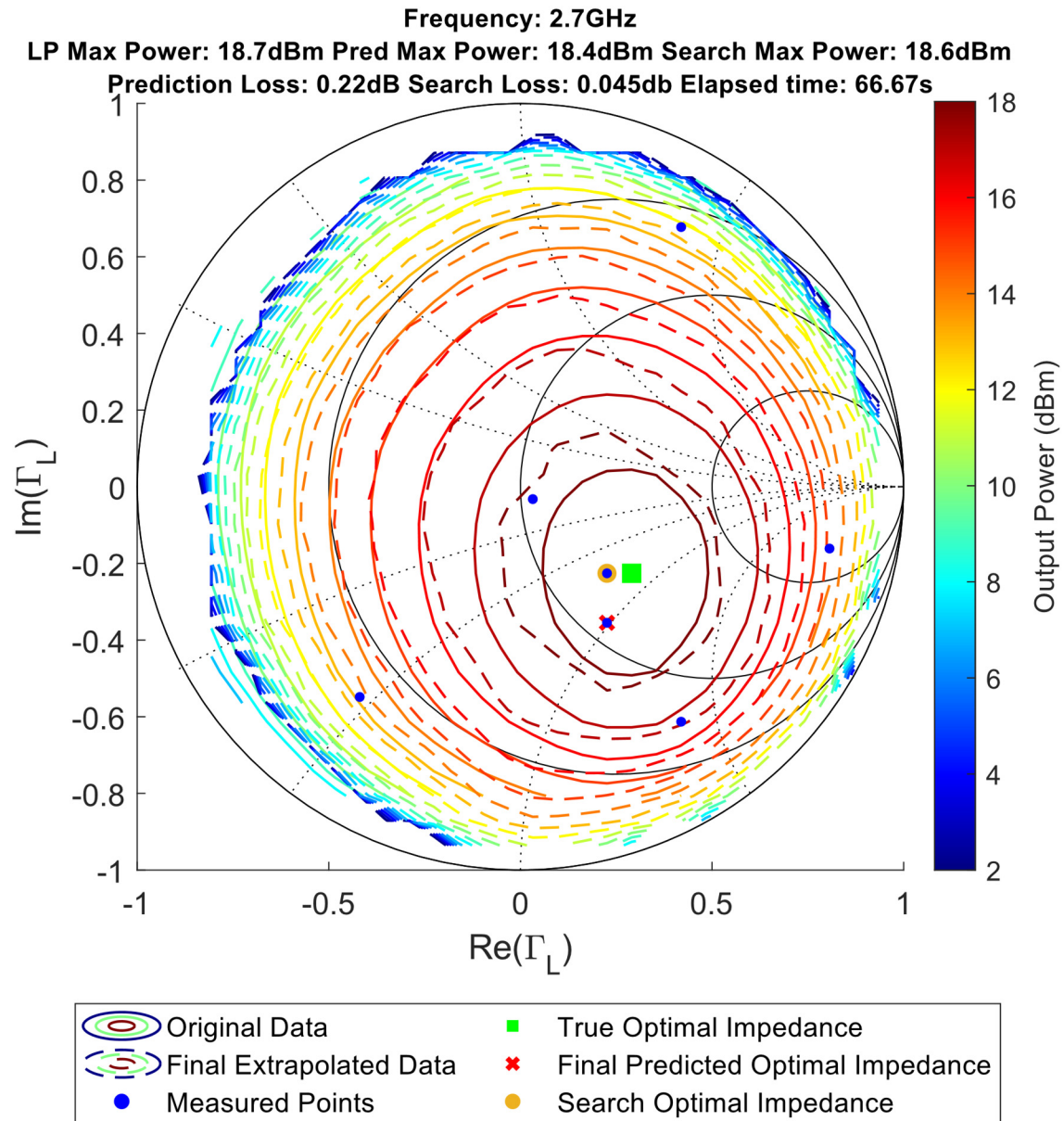


Figure 5.11. Results for a single run of the load-pull extrapolation circuit optimization algorithm at 2.7 GHz. This search evaluated 7 impedances in 67 seconds, converging to an impedance 1 pixel to the left of the true optimal impedance, with an associated performance loss of 0.05 dB.

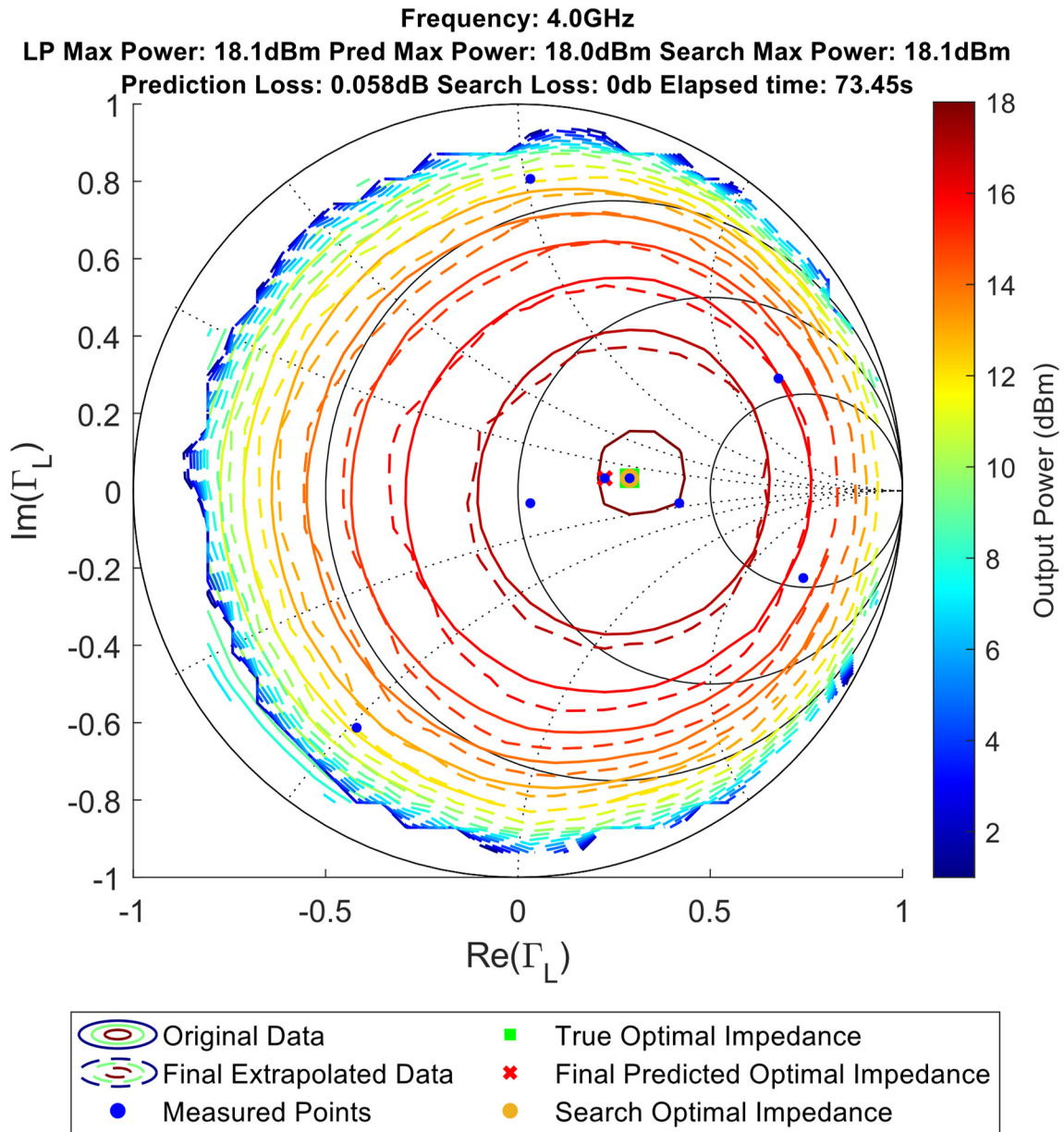


Figure 5.12. Results for a single run of the load-pull extrapolation circuit optimization algorithm at 4 GHz. This search evaluated 8 impedances in 73 seconds, converging to the true optimal impedance.

An overview of the achieved performance (compared to load-pull maximum) and elapsed time for each trial is shown in Figure 5.13. To accurately compare the search performance against the maximum power reported by the load-pull for each frequency, the load-pull performance for the final search impedance is used in place of the power reported at the end of the search. This eliminates the impact of small variations in measured power that occur over the significant time needed to run all 1050 trials.

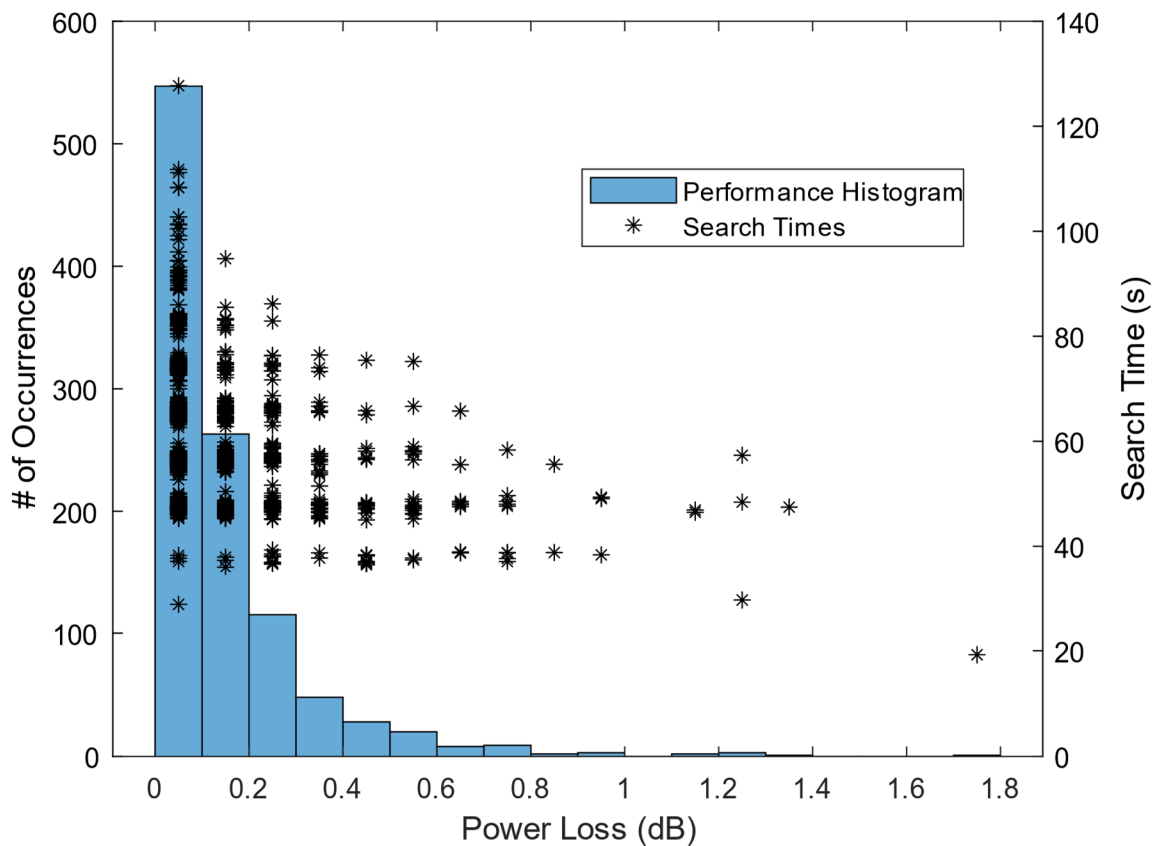


Figure 5.13. Overview of search results for circuit optimization with load-pull extrapolation using the traditional load-pull system of Section 3.5. Results are shown for 1050 searches ran across 21 frequencies from 2 to 4 GHz. Power loss is the difference in performance for the optimal load-pull impedance and the final search impedance.

The search algorithm is generally successful, converging to within 0.5 dB of the optimal performance 95% of the time (1001 out of 1050 trials). Of these trials, the search

converges within 60.5 s on average, with 95% of these searches converging within 84 s. Additionally, more than half the searches obtain performance within 0.1 dB of the true optimum (547 out of 1050 trials). Instances that miss the optimal impedance by a significant margin generally obtained an early repeated maximum predicated impedance, leading to early search convergence, such as the result shown in Figure 5.14. This can be mitigated by requiring a minimum number of measured points prior to convergence and selecting additional impedances to evaluate by some other means when an early repeat does occur. However, imposing a minimum number of measurements also imposes a floor on how quickly the search is allowed to converge.

Compared to a gradient search such as the one implemented in [72], this algorithm is able to converge much faster. Histograms of the elapsed times for the gradient search of [72] and extrapolation search are shown in Figure 5.15. While [72] does not report elapsed times for each search, an estimate can be performed by applying the average tuning and measurement time for the traditional load-pull system to the number of performance queries reported in [72] (assuming the computation time required for the gradient search is negligible). By this standard, the 14 searches performed in [72] converge in an average time of 166.7 s – nearly double the 95th percentile time for the extrapolation searches achieving within 0.5 dB of the optimal performance. This faster convergence comes at a cost of performance consistency: the total variation in final impedance for the gradient search is reported to be on the order of half a single pixel in the load-pull extrapolation search (each pixel is roughly 0.06 units wide on the Smith Chart). Note that it may be possible to improve the accuracy of the load-pull

extrapolation algorithm by training on a collection of non-linear data, as opposed to the simulated, linear data used in this chapter.

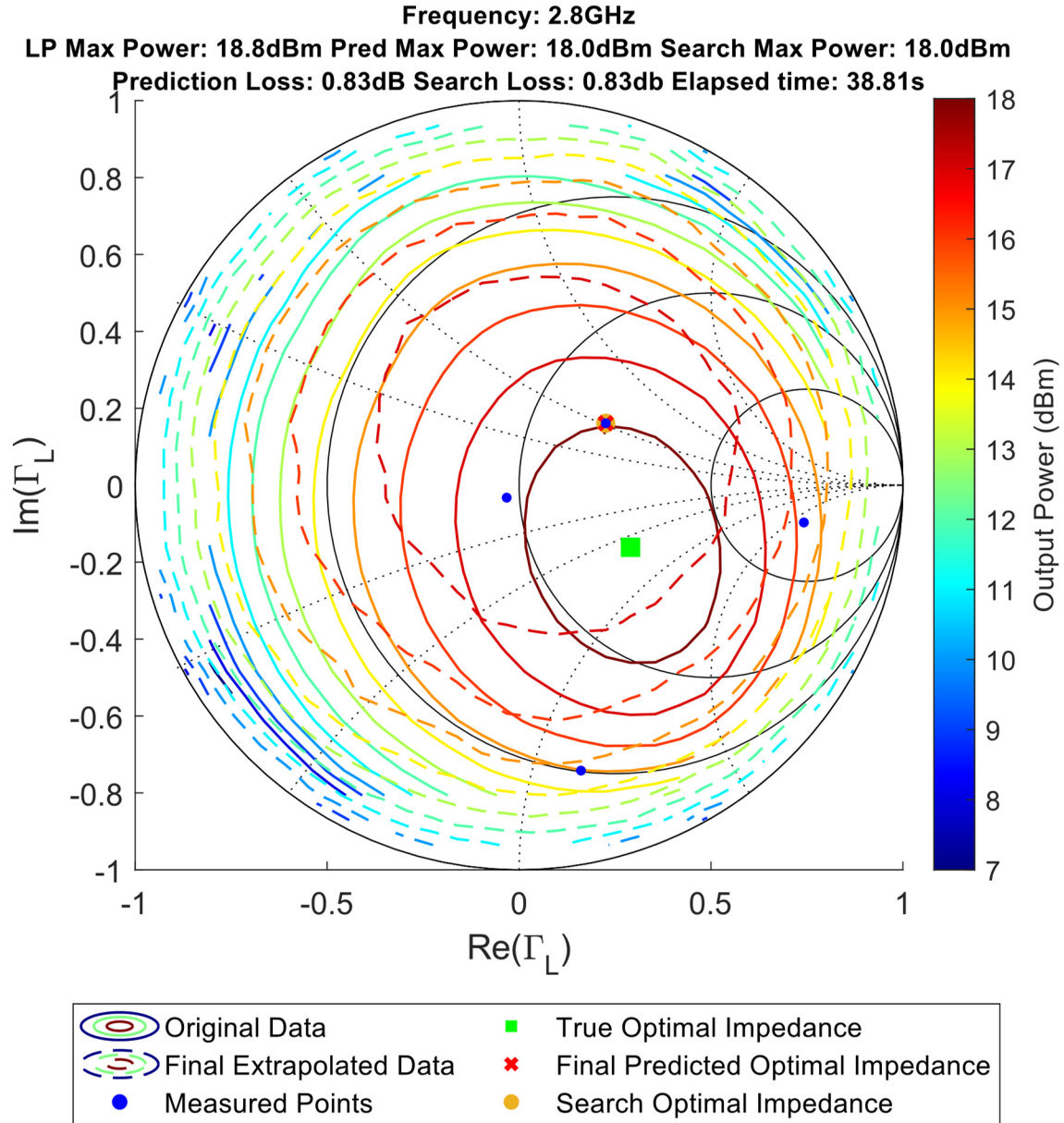


Figure 5.14. Results for a sub-optimal run of the load-pull extrapolation circuit optimization algorithm at 2.8 GHz. This search converged early after evaluating 4 impedances in 39 seconds, missing the true optimum by a significant margin.

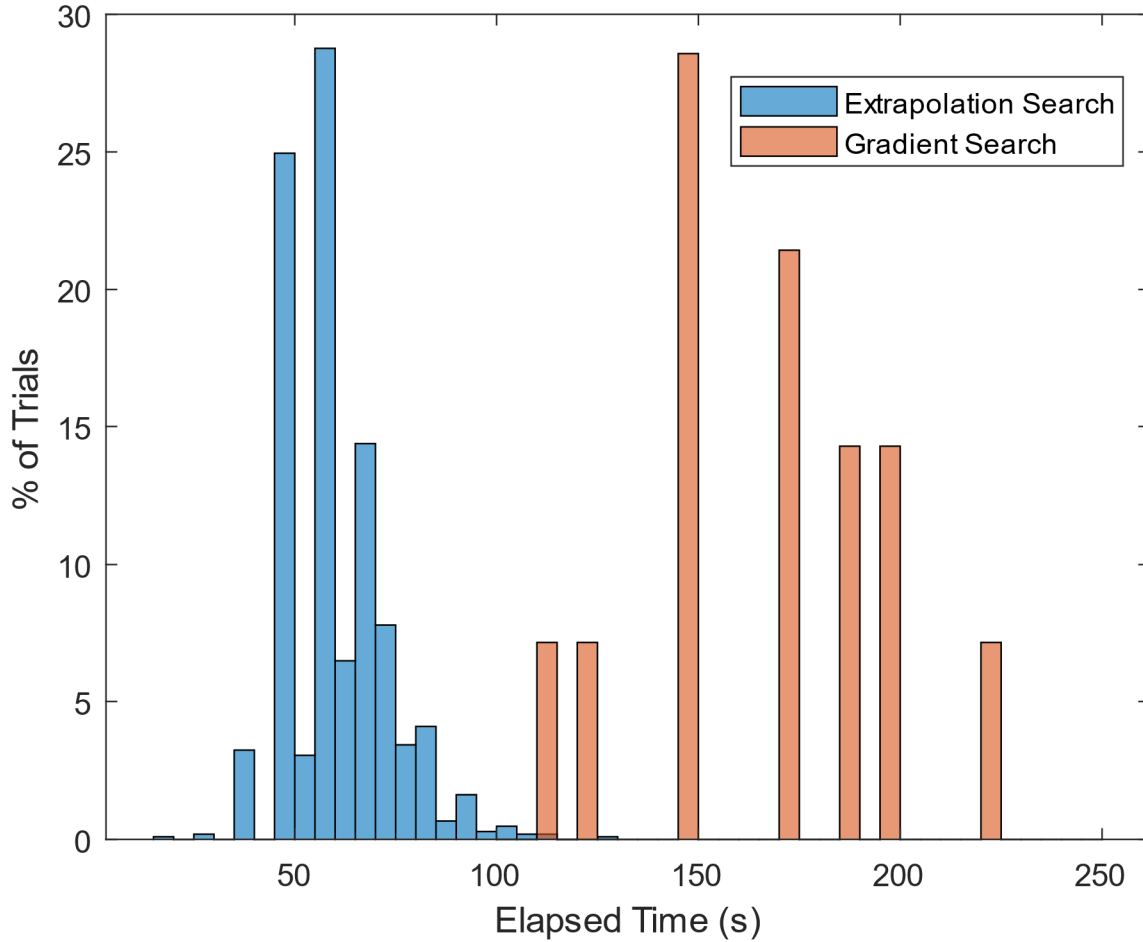


Figure 5.15. Comparison of elapsed times for the load-pull extrapolation search and the gradient algorithm of [72].

5.4.2 Load-Pull Extrapolation Analysis

Following up on the results of Section 5.3 for linear devices, this section considers the quality of the load-pull extrapolations performed as part of the searches in Section 5.4.1. Over the course of those searches, extrapolations were performed using anywhere from 1 to 14 measurements. However, only 1 extrapolation each was run for 13 and 14 measurements, and only 5 were run for 12 measurements. Figures 5.16 and 5.17 show statistics for the error in the predicted power and optimal impedance for all extrapolations with at least ten extrapolations per input dataset size. Table 5.3 provides a

numeric summary of these results for comparison with the simulated, linear results of Table 5.2.

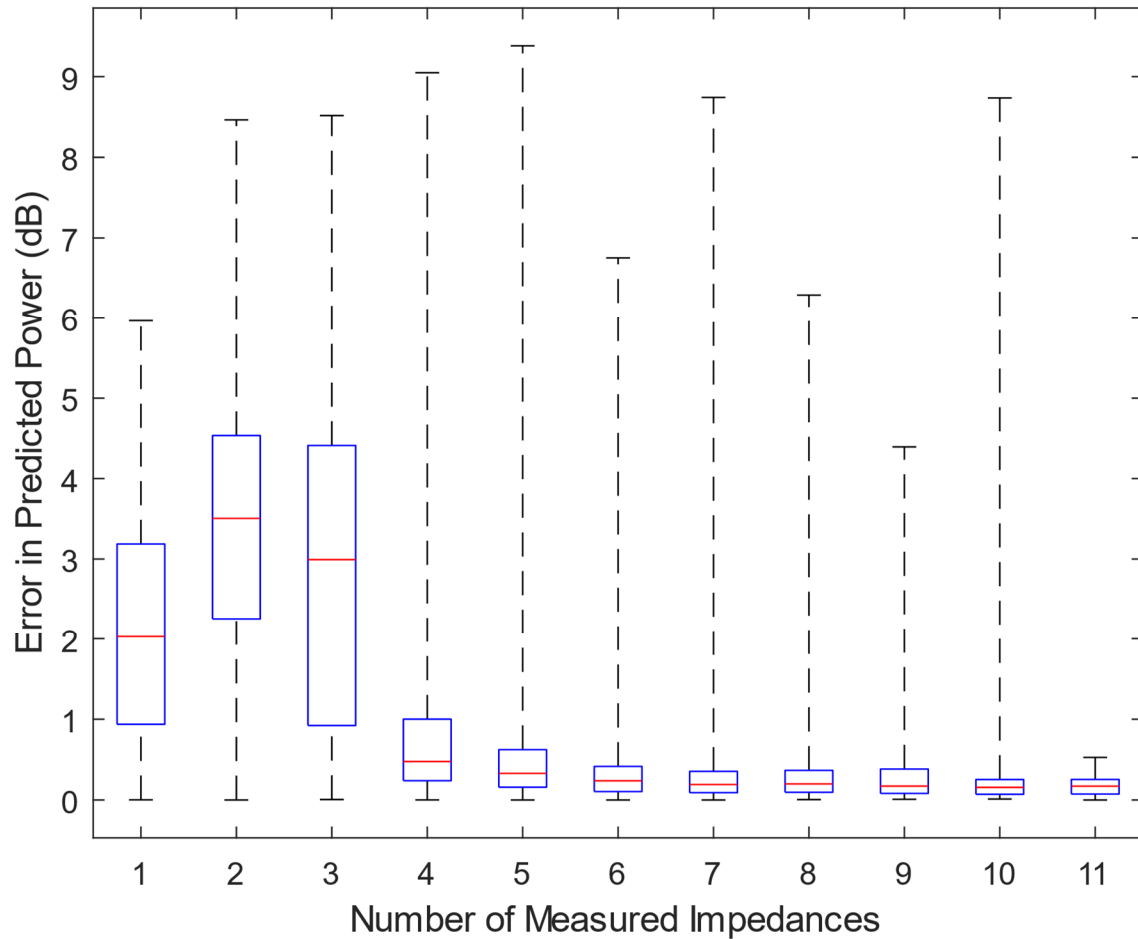


Figure 5.16. Power error statistics for the extrapolations performed in Section 5.4.1. Here, error is the difference between the measured load-pull maximum performance and the maximum power reported by the extrapolated load-pull.

Comparing the results of Tables 5.2 and 5.3, it appears that the extrapolations based on at least 7 measurements perform comparably to the linear results using the 0.3 mask with 81 measurements. This finding suggests that the load-pull extrapolation benefits greatly from having a collection of points scattered throughout the Smith Chart, as opposed to a group of points near a single area. This finding may be useful for other

microwave device modeling applications, such as the results of [86], which used measurements from a uniform grid in a single area of the Smith Chart. Additionally, the extrapolation method continues to perform quite well on non-linear measurements, despite having only been trained on simulated, linear devices.

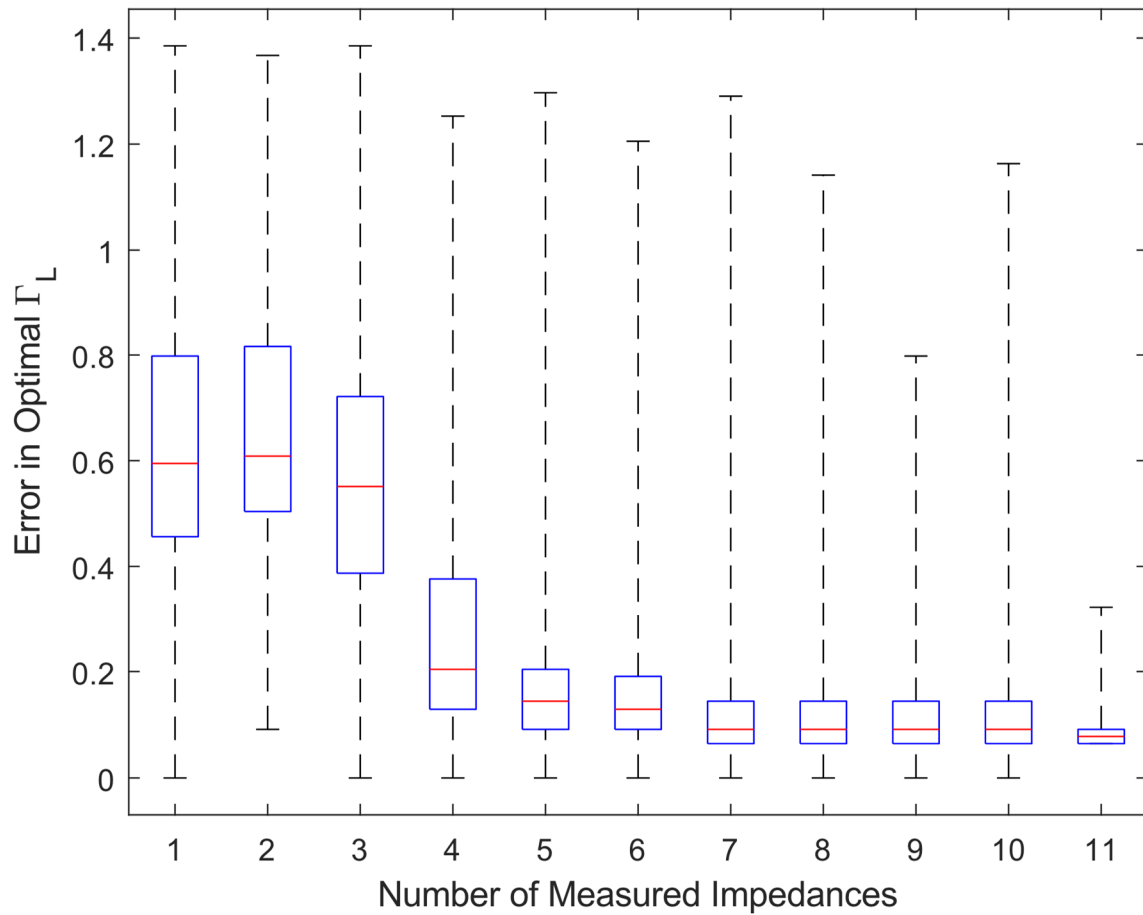


Figure 5.17. Load impedance error statistics for the extrapolations performed in Section 5.4.1. Here, error is the distance between the measured load-pull optimal reflection coefficient and the optimal reflection coefficient reported by the extrapolated load-pull.

Table 5.3. Non-Linear Load-Pull Extrapolation Performance – Predicted Peak Statistics

Number of Measured Impedances	Sample Size	Mean Power Error (dB)	Median Power Error (dB)	Mean Γ_L Error	Median Γ_L Error
1	1050	2.13	2.03	0.612	0.595
2	1050	3.36	3.51	0.655	0.609
3	1049	2.90	2.99	0.564	0.551
4	1047	1.04	0.477	0.275	0.204
5	1013	0.618	0.330	0.203	0.144
6	747	0.338	0.238	0.146	0.129
7	416	0.359	0.193	0.135	0.091
8	197	0.371	0.199	0.129	0.091
9	81	0.293	0.172	0.132	0.091
10	34	0.425	0.156	0.128	0.091
11	12	0.179	0.171	0.107	0.078

CHAPTER SIX

Effects of Impedance Tuning on Range-Doppler Processing

The work presented in this chapter has been published in: [96] A. Egbert *et al.*, "The Effect of Real-Time Radar Transmitter Amplifier Impedance Tuning on Range and Doppler Detection Accuracy," *2019 IEEE Texas Symposium on Wireless and Microwave Circuits and Systems (WMCS)*, Waco, TX, USA, 2019, pp. 1-4, doi: 10.1109/WMCaS.2019.8732549. © 2019, IEEE.

6.1 Background

One disadvantage associated with applying cognitive radar techniques on a pulse-to-pulse basis is the disruption to normal radar signal processing and target detection. Common processing approaches, such as matched filtering and range-Doppler processing, rely on the transmitted radar signal remaining unchanged from its initial synthesis throughout the processing time interval. These techniques estimate the range and velocity away from the radar system of various targets by evaluating the round-trip time delay and observed Doppler shift between the radar's transmitter and receiver. Range-Doppler processing specifically requires coherency over multiple pulse transmissions to accurately extract the required Doppler shift estimation. The period of time associated with the set of pulses used to generate a single range-Doppler image is the coherent processing interval (CPI).

Kirk has examined the significant effects of altering the radar waveform used for detection during a CPI, such as through rapidly alternating between channels according to a cognitive dynamic spectrum access strategy [30]. These variations result in distortions to a target's range-Doppler signature. By determining the response for a point target with

zero range and velocity using the variable signal set, the expected distortion of targets can be isolated. The range-Doppler image can then be processed as normal, followed by Richardson-Lucy deconvolution with the distorted point target response to reduce the distortions caused by the non-constant signal [97].

Variations within the reconfigurable transmit hardware can also cause distortions in target detection as the signal content is altered. If transmit hardware adaptations can be limited to the listening period of the radar between CPIs, then no impact is realized. However, as discussed Chapter Four, the reconfiguration times of available high-power impedance tuners is much greater than the listening time between radar pulses. As such, mitigation techniques should be employed to minimize the impact of distortions caused by impedance tuners during transmission to avoid disruptions in radar data availability. This chapter specifically examines the effects of signal phase shifts caused by reconfigurable hardware components in a radar transmitter.

Reconfigurable devices have previously been investigated for phase-shift related operations such as beamforming using micro-electrical mechanical systems (MEMS) tunable phase shifters [98]. As an example of possible negative effects associated with tunable hardware, unwanted Doppler shifts have been observed in acousto-optic filter designs, as presented by Boyd [99]. Here, Boyd corrects for the Doppler shifts by predistorting the input signal to offset the shifts caused by the tunable component. To address another potential effect of such adaptive components, Zeidan presents an approach to detect and correct transient phase shifts in RF receiver chains used for communications [100]. The presented method is able to detect a change in the gain state of the receive amplifier (impacting both the signal amplitude and phase offset) and

synthesize corrected data. However, this approach is not well suited to radar transmit systems, as it works to isolate and account for hardware distortions generated in the receive hardware, which is possible as all the received data will be affected at the single time instance when the receiver performed an adaptation. Distortions from the transmit hardware differ as they will first interact with the environment and radar targets, arriving at the radar receiver at several different times, requiring the receiver to apply the time-domain correction to each reflected instance of the signal obtained by the receiver.

6.2 Proposed Theory of Adaptive Component Doppler Shifts

While the objective of impedance tuning is to alter the impedance presented to the amplifying device, the tuners of [25-26] also alter the magnitude of the signal (by modulating the gain of the amplifier or the tuner's own power loss characteristic) as well as the phase shift applied to the signal as it propagates through the tuner. Together, these effects are considered as the complex-valued transmission S-Parameter, S_{21} . Assuming S_{21} remains constant during transmission, no impact to the quality of radar processing occurs, aside from the intended impact on amplifier gain as well as the incidental transmission coefficient magnitude influencing the maximum detectable range. However, while transitioning between two impedances, a tuner causes a time-varying phase shift through the transmit chain. This variable phase offset can be equated to an apparent false Doppler frequency shift in the target responses using the instantaneous definition of frequency:

$$f_D = \frac{1}{2\pi} \frac{d\phi(t)}{dt}, \quad (6.1)$$

where f_D is the apparent shift in Hertz and $\phi(t)$ is transmitted signal phase at time t at the impedance tuner output reference plane.

6.3 Range-Doppler Processing During Impedance Tuning

In this section, range-Doppler analysis of a simulated target is performed while transitioning between different impedances with the tuner of [25] (shown in Figure 6.1). This tuner, controlled based on cavity position numbers n_1 and n_2 , is used to control the load impedance for a Microwave Technologies MWT-173 FET during range-Doppler measurements of a simulated radar target. For context, a load-pull of the amplifier's power added efficiency (PAE) using the tuner is shown in Figure 6.2.

In the first experiment, the tuner was set to a position of $(n_1, n_2) = (6000, 6000)$, and the range and Doppler of a simulated target were measured. Four CPIs, each consisting of 500 acquisitions of 8192 samples, were collected at 10 MS/s using a Hamming windowed chirp waveform with 3 MHz bandwidth centered at 3.55 GHz with a 50% duty cycle. The simulated target is located approximately 49.8 km downrange and exhibits a Doppler shift of 49 Hz. Figure 6.3 shows range-Doppler detections from repeating this experiment for four different tuning scenarios, with each scenario tested four times with a CPI of 500 acquisitions: (1) tuner stationary at (6000, 6000), (2) tuner stationary at (7200, 7200), (3) tuner moving from (6000, 6000) to (7200, 7200), and (4) tuner moving from (7200, 7200) to (6000, 6000). These tuner positions are chosen to demonstrate the most significant transition based on Figure 6.2.

For the two stationary settings (1) and (2), the detected range and Doppler are the same and correspond to the actual range and Doppler of the target. However, in setting (3), when the tuner is moving from (6000, 6000) to (7200, 7200), an apparent Doppler

shift of -0.29 Hz is visible relative to the detected Doppler under stationary tuner conditions, indicated by the left shift in the upper portion of Figure 6.3. Additionally, when the tuner is moved from (7200, 7200) to (6000, 6000) in setting (4), an apparent relative Doppler shift of +0.29 Hz (right shift) is observed. In settings (3) and (4), the changing phase of the tuner's S_{21} causes the artificial Doppler shift based on the speed of the tuner movement from equation (1). This ± 0.29 Hz error translates to approximately 3 cm/s of velocity error under the radar configuration presented here.



Figure 6.1. First-generation evanescent-mode cavity tuner with piezo actuators developed by Purdue University [25]. © 2019, IEEE.

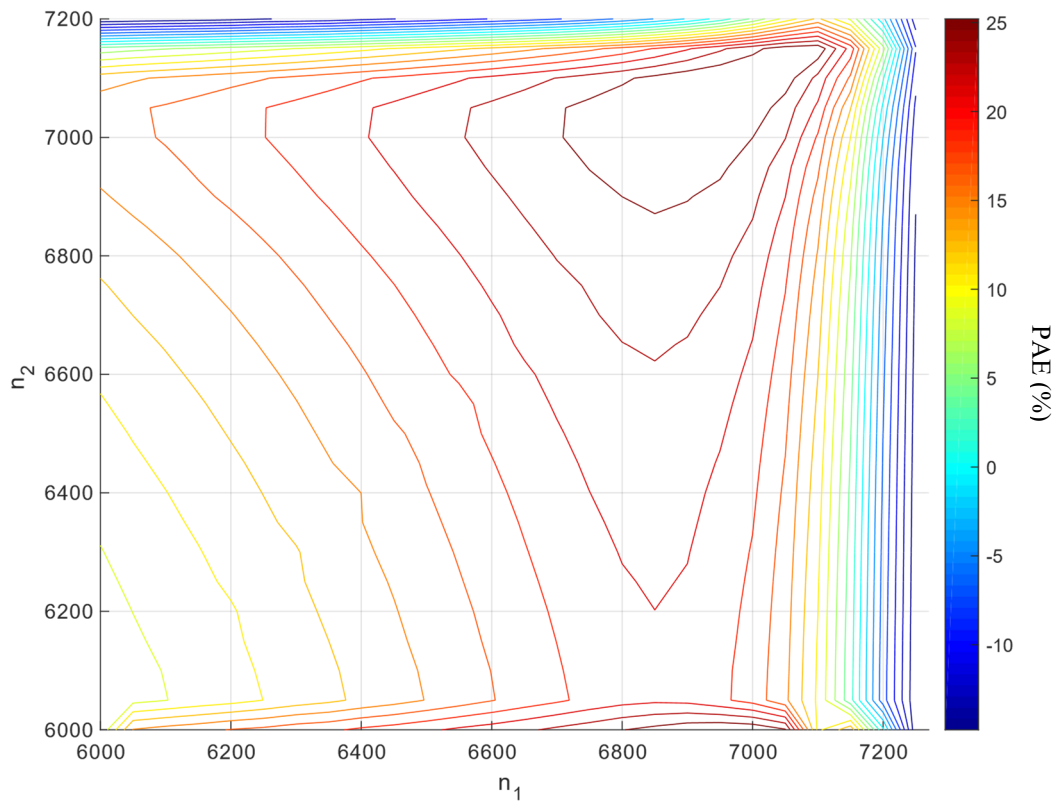


Figure 6.2. MWT-173 FET power-added efficiency (PAE) contours for variations of cavity position numbers (n_1 , n_2) at 3.55 GHz. © 2019, IEEE.

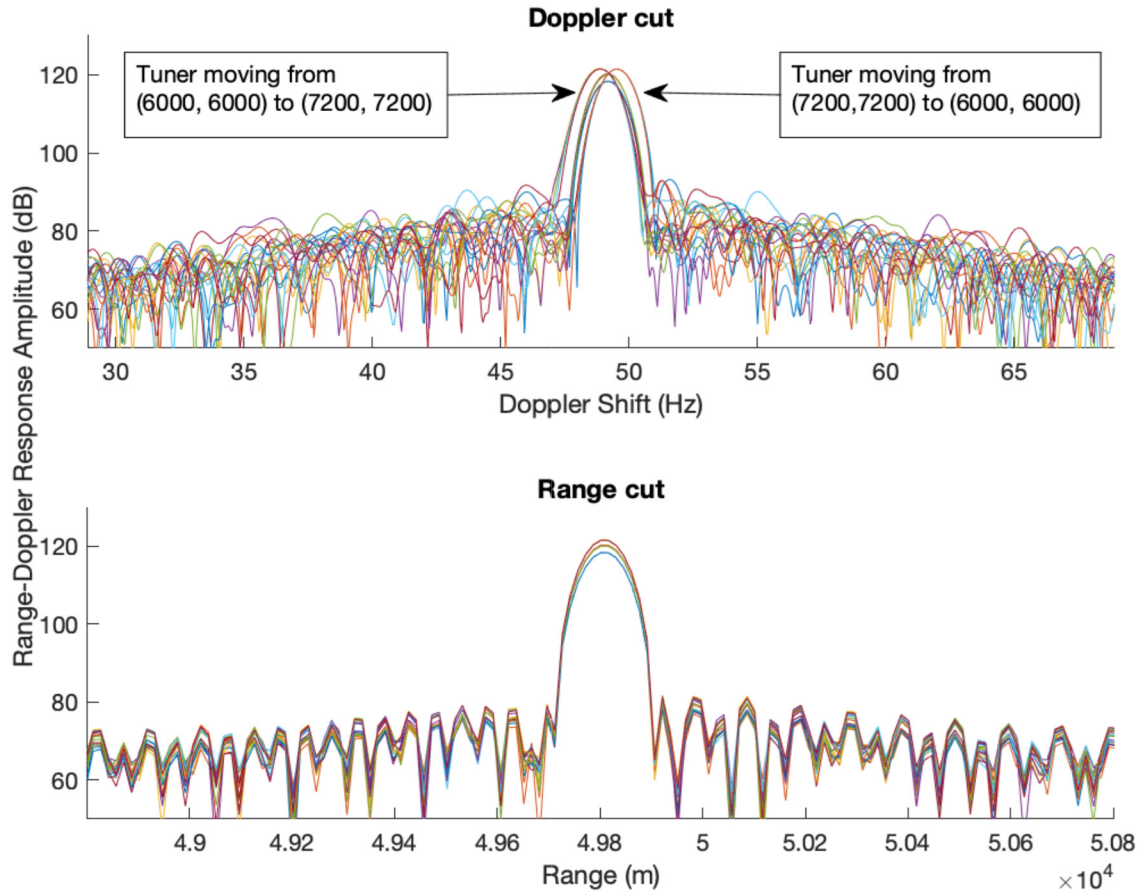


Figure 6.3. Doppler and range detection results from measurements with simulated radar target: (1) tuner stationary at (6000, 6000), (2) tuner stationary at (7200, 7200), (3) tuner moving from (6000, 6000) to (7200, 7200), and (4) tuner moving from (7200, 7200) to (6000, 6000). © 2019, IEEE.

6.4 Direct Measurements of Impedance Tuning Doppler Shift

Building on the results of the previous section, measurements of the tuner's S_{21} were measured using a vector network analyzer (VNA) during tuning operations across the path between $(n_1, n_2) = (6000, 6000)$ to $(7500, 7500)$ and vice versa. The transmission coefficient phase during these operations is shown in Figure 6.4. Over the transition period, the transmitted signal experiences nearly a 180° phase shift realized at a non-linear rate (i.e., the applied frequency shift is itself time-varying). The expected instantaneous frequency shift at sample n can be calculated using

$$\Delta f[n] = \frac{\phi[n + 1] - \phi[n]}{\Delta t} \times \frac{1}{360^\circ}, \quad (6.2)$$

where $\phi[n]$ and $\phi[n + 1]$ are the phase values, in degrees, at the n^{th} and $(n + 1)^{th}$ samples respectively, and Δt is the time between samples. Based on this approach, the expected instantaneous detected Doppler shifts are plotted versus time in Figure 6.5.

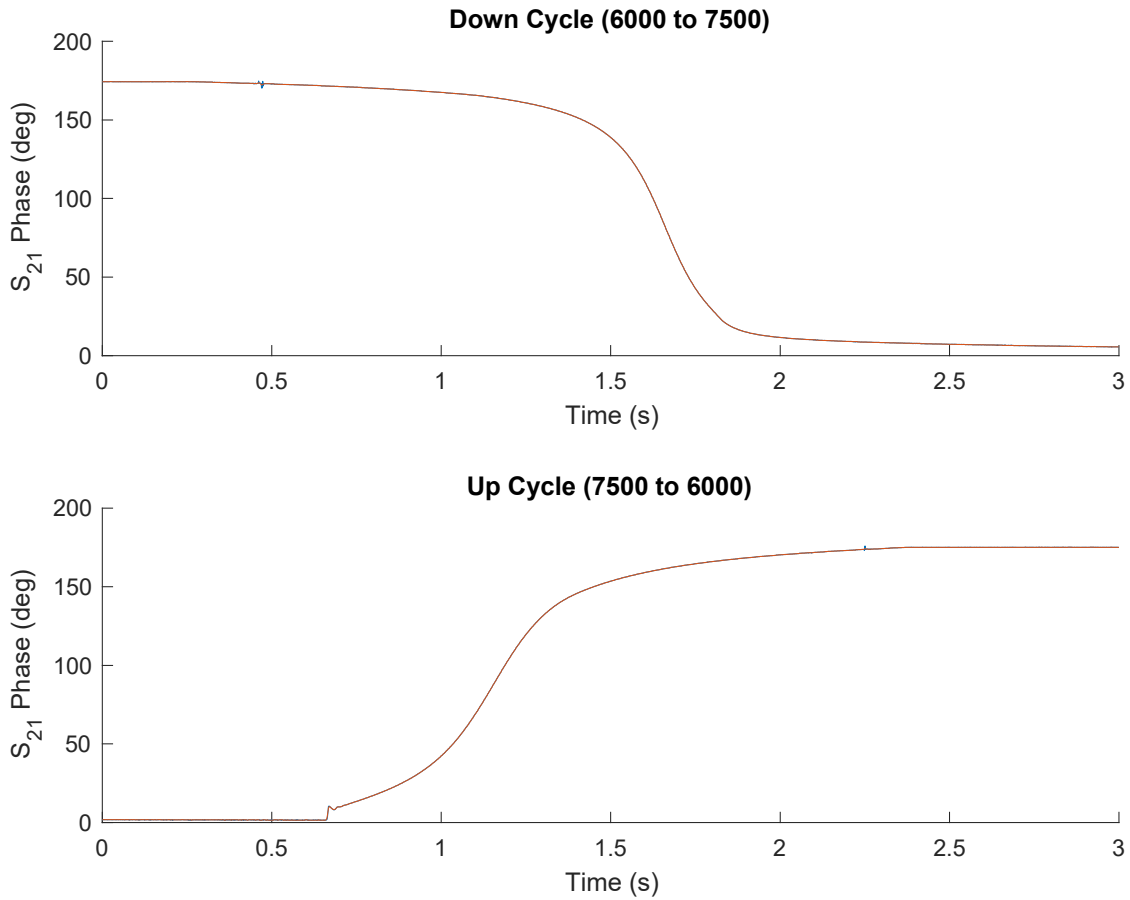


Figure 6.4. Tuner transmission coefficient (S_{21}) phase versus time in tuning from $(n_1, n_2) = (6000, 6000)$ to $(7500, 7500)$ (top) and from $(7500, 7500)$ to $(6000, 6000)$ (bottom). © 2019, IEEE.

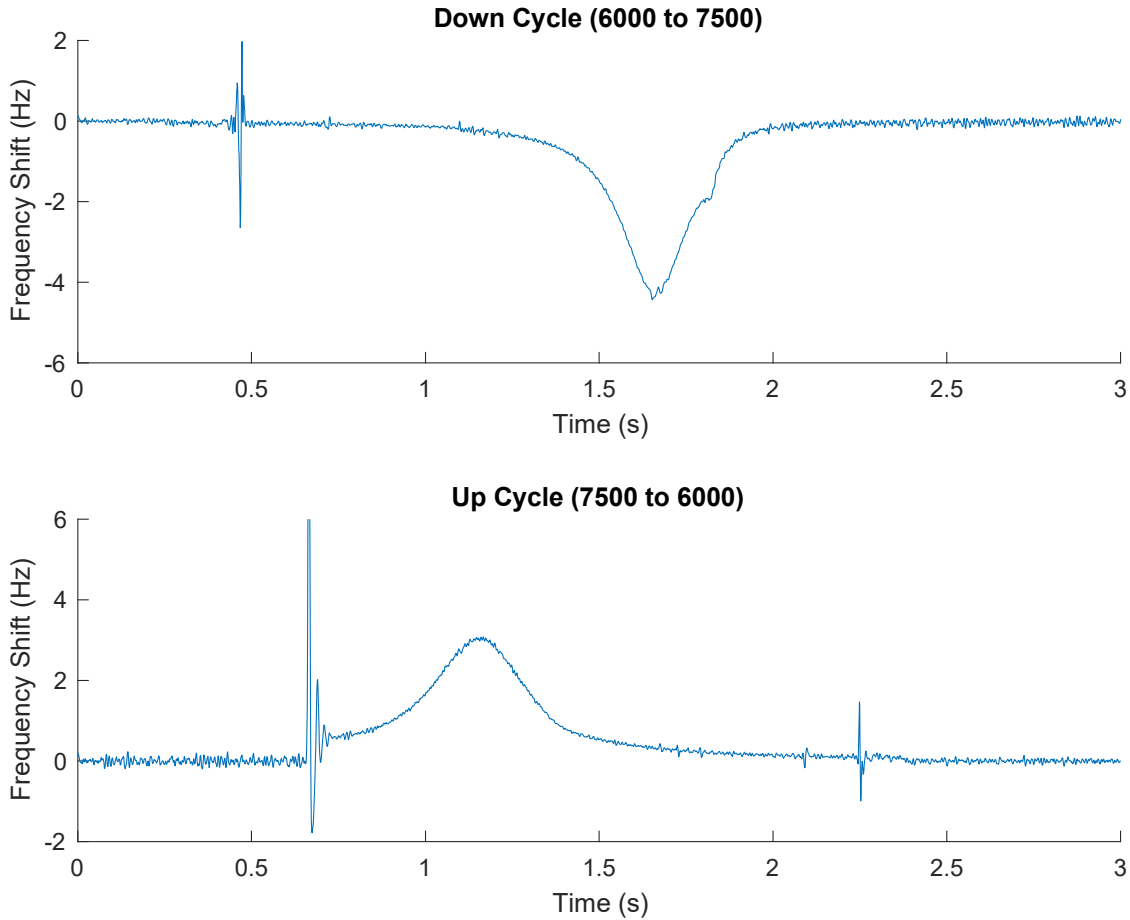


Figure 6.5. Calculated estimated Doppler frequency shift versus time in tuning from $(n_1, n_2) = (6000, 6000)$ to $(7500, 7500)$ (top) and from $(7500, 7500)$ to $(6000, 6000)$ (bottom). © 2019, IEEE.

The initially large-amplitude activity observed in the interval $0.4 \text{ s} < t < 0.6 \text{ s}$ of Figure 6.5 is attributed to the sudden start of tuner movement. During the interval $0.5 \text{ s} < t < 2 \text{ s}$ the tuner performs its movement (for the down cycle case), and the expected Doppler frequency shift ranges from $0 < f < 4.5 \text{ Hz}$. The maximum value of this shift is much larger than the $\pm 0.29 \text{ Hz}$ observed in Figure 6.3. This discrepancy suggests that the range-Doppler processing in some way averages the measured instantaneous frequency shift over the entire CPI, or otherwise in some way does not experience the worst-case Doppler shift. (A closer look at this behavior is included later

in this chapter.) For these measurements, the CPI acquisition period roughly overlaps the $0.5 \text{ s} < t < 1.75 \text{ s}$ interval of Figure 6.4, resulting in an observed phase shift of nearly 130 degrees over 1.25 s. This would correspond with a uniform Doppler shift of approximately $0.36 \text{ cycles}/1.25 \text{ s} = 0.288 \text{ Hz}$, agreeing with the $\pm 0.29 \text{ Hz}$ shift of Figure 6.3.

To confirm the VNA measurement results, a second experiment was performed using two equal-frequency tones fed through a mixer, with one tone passing through the tuner and an oscilloscope measuring the mixer's output. Here, the mixer uses the unmodified tone to down-convert the tuner-modulated signal to baseband. A block diagram of this setup is shown in Figure 6.6.

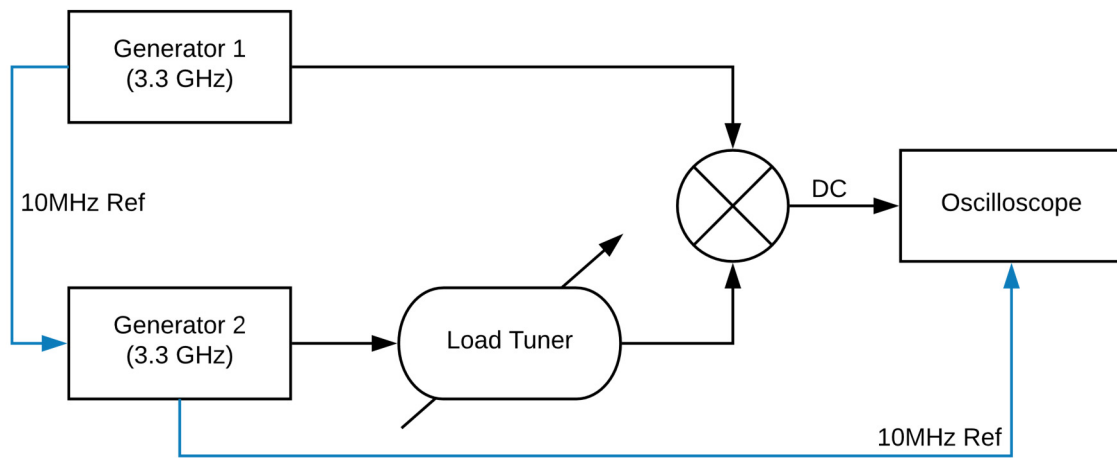


Figure 6.6. Down-conversion measurement setup for tuner frequency shift. © 2019, IEEE.

When the tuner is moved, the S_{21} phase change causes the waveform to change phase by 180 degrees over the tuning time, and a partial sinusoid (generated by the varying relative phase of the mixer inputs and corresponding to the artificial Doppler shift) will appear at the output of the mixer until the tuner has settled at its new state. At

this point, the mixer output takes on a new amplitude based on the new relative phase of the mixer inputs. Figure 6.7 shows the mixer output during tuner movements in both directions: from (6000, 6000) to (7500, 7500) and then reversed. The calculation of the instantaneous frequency at the n th sample, $f[n]$, can be approximated from the recovered signal phase

$$y[n] = A \cos(\phi[n]) \leftrightarrow \phi[n] = \cos^{-1}\left(\frac{1}{A}y[n]\right) \quad (6.3)$$

with a forward difference similar to (6.2) as follows:

$$f[n] = \frac{1}{2\pi} \frac{\cos^{-1}\left(\frac{1}{A}y[n+1]\right) - \cos^{-1}\left(\frac{1}{A}y[n]\right)}{\Delta t}, \quad (6.4)$$

where $y[n]$ is the n^{th} sample of the measured mixer output, A is the amplitude of the assumed cosine waveform, and Δt is the time between samples. Figure 6.8 shows good correspondence between instantaneous frequency shift estimations from this down-conversion setup and VNA measurements.

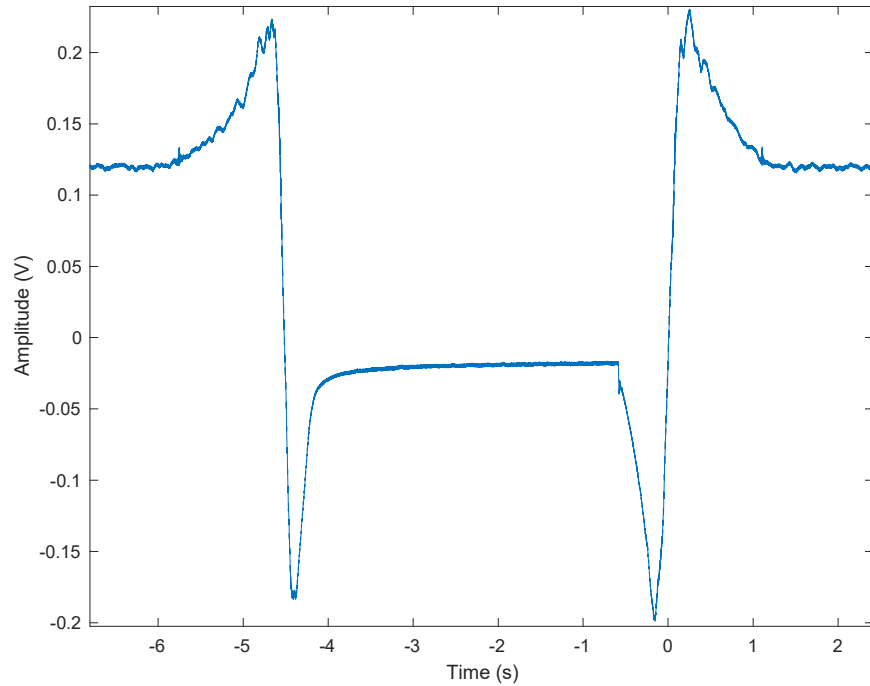


Figure 6.7. Oscilloscope-measured signal for tuner transitions from (6000, 6000) to (7500, 7500) and reversed from (7500, 7500) to (6000, 6000). © 2019, IEEE.

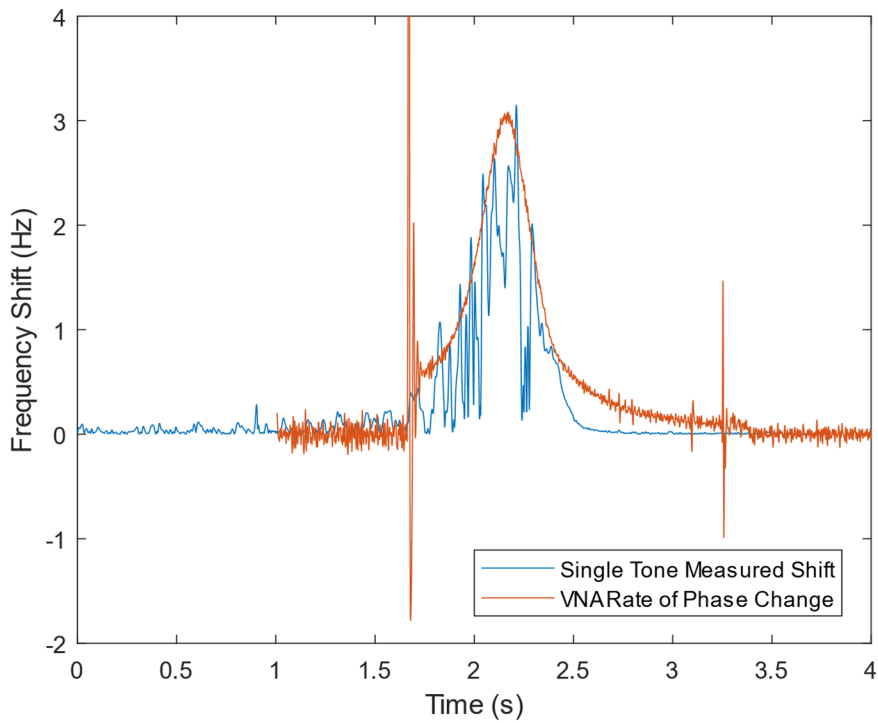


Figure 6.8. Instantaneous frequency shift measurements from the VNA (red) and down-conversion (blue) measurement setups.

6.5 Distortion Analysis and Correction Process

6.5.1 Matched Filtering Distortion – Range Errors

As range-Doppler processing is built upon matched filter detection, it is important to understand the impacts of frequency shifts on matched filtering operations. Matched filtering operates by correlating the received radar data with the transmit waveform, looking for peaks in the correlation response that indicate the presence of a target's returned signal. For a transmitted signal $S_{in}(t)$, the target response $S_{out}(t)$ via matched filtering is given by the signal's autocorrelation:

$$S_{out}(t) = \int_{-\infty}^{\infty} S_{in}(\tau) S_{in}^*(\tau - t) d\tau, \quad (6.5)$$

where $S_{in}^*(t)$ represents the complex conjugate of the input signal.

To evaluate how a signal performs given a moving target's imposed Doppler shift (radial velocity), this correlation process can be performed with frequency-shifted versions of the transmit waveform. The set of all possible matched filter responses for a single point target is provided by the ambiguity function $\chi(f_D, t)$:

$$\chi(f_D, t) = \int_{-\infty}^{\infty} S_{in}^*(\tau - t) S_{in}(\tau) e^{j2\pi f_D \tau} d\tau, \quad (6.6)$$

where $e^{j2\pi f_D t}$ applies a frequency shift of f_D . For the common linear frequency modulated (LFM) chirp radar waveform with period T , carrier frequency \bar{f} , and frequency modulation slope k

$$S_{LFM}(t) = \Pi\left(\frac{t}{T}\right) e^{j2\pi \bar{f} t} e^{j\pi k t^2}, \quad (6.7)$$

the ambiguity function is:

$$\begin{aligned}
\chi_{LFM}(f_D, t) &= \int_{-\infty}^{\infty} \Pi\left(\frac{\tau-t}{T}\right) e^{-j2\pi\bar{f}(\tau-t)} e^{-j\pi k(\tau-t)^2} \Pi\left(\frac{\tau}{T}\right) e^{j2\pi\bar{f}\tau} e^{j\pi k\tau^2} e^{j2\pi f_D\tau} d\tau \\
&= \int_{-\infty}^{\infty} \Pi\left(\frac{\tau-t}{T}\right) e^{+j2\pi\bar{f}t} e^{-j2\pi\bar{f}\tau} e^{-j\pi k(\tau-t)^2} \Pi\left(\frac{\tau}{T}\right) e^{j2\pi\bar{f}\tau} e^{j\pi k\tau^2} e^{j2\pi f_D\tau} d\tau \\
&= e^{j2\pi\bar{f}t} \int_{-\infty}^{\infty} \Pi\left(\frac{\tau-t}{T}\right) e^{-j\pi k\tau^2} e^{-j\pi k t^2} e^{j2\pi k t \tau} \Pi\left(\frac{\tau}{T}\right) e^{j\pi k\tau^2} e^{j2\pi f_D\tau} d\tau \\
&= e^{j2\pi\bar{f}t} e^{-j\pi k t^2} \int_{-\infty}^{\infty} \Pi\left(\frac{\tau-t}{T}\right) \Pi\left(\frac{\tau}{T}\right) e^{j2\pi k t \tau} e^{j2\pi f_D\tau} d\tau \\
&= e^{j2\pi\bar{f}t} e^{-j\pi k t^2} \int_{-\infty}^{\infty} \Pi\left(\frac{\tau-t}{T}\right) \Pi\left(\frac{\tau}{T}\right) e^{j2\pi(k t + f_D)\tau} d\tau \\
&= \begin{cases} e^{j2\pi\bar{f}t} e^{-j\pi k t^2} \int_{-T/2}^{t+T/2} e^{j2\pi(k t + f_D)\tau} d\tau, & -T \leq t \leq 0 \\ e^{j2\pi\bar{f}t} e^{-j\pi k t^2} \int_{t-T/2}^{T/2} e^{j2\pi(k t + f_D)\tau} d\tau, & 0 \leq t \leq T \end{cases} \\
&= \begin{cases} e^{j2\pi\bar{f}t} e^{-j\pi k t^2} \frac{e^{j2\pi(k t + f_D)(t+\frac{T}{2})} - e^{j2\pi(k t + f_D)(-\frac{T}{2})}}{j2\pi(k t + f_D)}, & -T \leq t \leq 0 \\ e^{j2\pi\bar{f}t} e^{-j\pi k t^2} \frac{e^{j2\pi(k t + f_D)\frac{T}{2}} - e^{j2\pi(k t + f_D)(t-\frac{T}{2})}}{j2\pi(k t + f_D)}, & 0 \leq t \leq T \end{cases} \\
&= \begin{cases} e^{j2\pi\bar{f}t} e^{-j\pi k t^2} e^{j2\pi(k t + f_D)\frac{t}{2}} \frac{e^{j2\pi(k t + f_D)(\frac{t}{2}+\frac{T}{2})} - e^{-j2\pi(k t + f_D)(\frac{t}{2}+\frac{T}{2})}}{j2\pi(k t + f_D)}, & -T \leq t \leq 0 \\ e^{j2\pi\bar{f}t} e^{-j\pi k t^2} e^{j2\pi(k t + f_D)\frac{t}{2}} \frac{e^{j2\pi(k t + f_D)(\frac{T}{2}-\frac{t}{2})} - e^{-j2\pi(k t + f_D)(\frac{T}{2}-\frac{t}{2})}}{j2\pi(k t + f_D)}, & 0 \leq t \leq T \end{cases} \\
&= \begin{cases} e^{j2\pi\bar{f}t} e^{-j\pi k t^2} e^{j\pi(k t + f_D)t} \frac{j2 \sin[2\pi(k t + f_D)(\frac{t}{2} + \frac{T}{2})]}{j2\pi(k t + f_D)}, & -T \leq t \leq 0 \\ e^{j2\pi\bar{f}t} e^{-j\pi k t^2} e^{j\pi(k t + f_D)t} \frac{j2 \sin[2\pi(k t + f_D)(\frac{T}{2} - \frac{t}{2})]}{j2\pi(k t + f_D)}, & 0 \leq t \leq T \end{cases}
\end{aligned}$$

$$\begin{aligned}
\chi_{LFM}(f_D, t) &= \begin{cases} e^{j2\pi\bar{f}t} e^{-j\pi kt^2} e^{j\pi kt^2} e^{j\pi f_D t} \frac{\sin[\pi(kt + f_D)(t + T)]}{\pi(kt + f_D)}, & -T \leq t \leq 0 \\ e^{j2\pi\bar{f}t} e^{-j\pi kt^2} e^{j\pi kt^2} e^{j\pi f_D t} \frac{\sin[\pi(kt + f_D)(T - t)]}{\pi(kt + f_D)}, & 0 \leq t \leq T \end{cases} \\
&= e^{j2\pi\bar{f}t} e^{j\pi f_D t} \frac{\sin[\pi(kt + f_D)(T - |t|)]}{\pi(kt + f_D)}, \quad -T \leq t \leq T \\
&= e^{j2\pi\bar{f}t} e^{j\pi f_D t} (T - |t|) \frac{\sin[\pi(kt + f_D)(T - |t|)]}{\pi(kt + f_D)(T - |t|)}, \quad -T \leq t \leq T \\
\chi_{LFM}(f_D, t) &= e^{j2\pi\bar{f}t} e^{j\pi f_D t} (T - |t|) \text{sinc}[\pi(f_D + kt)(T - |t|)], \quad -T \leq t \leq T, \quad (6.8)
\end{aligned}$$

where $\Pi\left(\frac{t}{T}\right)$ is the rectangle function with width T . This result leads to the “tilted sinc” target response pattern common to LFM radar signals, with a propagation delay (range) error due to target Doppler shifting of

$$t_{error} = \frac{f_D}{k}, \quad (6.9)$$

as reported in [101]. Returning to the idea of unintentional phase shifts from tunable components, an example of the matched filter target responses for various per-pulse phase shifts is shown in Figure 6.9. In each case, the listed phase change occurs linearly during the period of a single LFM pulse with a bandwidth of 5 MHz and period of 819.2 μs ($k = 6.1 \text{ GHz/s}$); the right-most shift of 1080° corresponds to a frequency shift of 3.662 kHz (3 cycles/819.2 μs).

Note that this expected range error is not apparent in the experimental results shown in Figure 6.3. This is because the actual phase shifts exhibited by the tuner of [25] are much smaller than those shown in Figure 6.9. Assuming the maximum shift of 4.5 Hz, a propagation delay error of 0.61 ns is expected—much lower than the sample

period of 10 ns used in Figure 6.9. As such, no correction for phase shifts using this tuner is required for range detection with matched filtering with these radar waveforms.

6.5.2 Range-Doppler Distortion – Velocity Errors

To acquire a range-Doppler image, multiple pulses within a CPI are processed via matched filtering, and the resulting range bins are Fourier transformed. Given the discussion in the previous section, one might assume that the tuner of [25] should not degrade range-Doppler results as the impact on the matched filter output magnitude is negligible due to the slow rate of phase change compared to the waveform period. However, range-Doppler processing utilizes the complex-valued matched filter response—not only the response magnitude. In practice, each matched filter output $S_{out}(t)$ experiences a nearly constant phase offset during each transmission

$$S_{out}(t) = \int_{-\infty}^{\infty} S_{in}(\tau)S_{in}^*(\tau - t)e^{-j\phi(\tau)}d\tau \approx e^{-j\phi} \int_{-\infty}^{\infty} S_{in}(\tau)S_{in}^*(\tau - t)d\tau, \quad (6.10)$$

where $\phi(t)$ is the tuner phase shift at time t . Over the course of an entire CPI, each pulse (and by extension, each matched filter output) will express a different phase offset

$$S_{out}(t)[n] \approx e^{-j\phi[n]} \int_{-\infty}^{\infty} S_{in}(\tau)S_{in}^*(\tau - t)d\tau, \quad (6.11)$$

where $S_{out}(t)[n]$ indicates the n^{th} pulse response within a CPI and $\phi[n]$ is the current tuner phase shift during the n^{th} pulse. Figure 6.10 shows the magnitude and phase of the matched filter output for constant phase offsets of 0° , 50° , and 100° .

This per-pulse constant phase offset assumption of (6.10) and (6.11) is valid for the measurement data in Figure 6.4. To confirm, a CPI of LFM waveforms was generated with the CPI equal to the measurement period of the tuner phase data, and each sample within the CPI was given an additional phase offset equal to the tuner phase offset at that

time. Each pulse was then match filtered against the first pulse in the CPI. The resulting per-pulse matched filter phase response at each range peak is shown in Figure 6.11, along with the applied tuner phase profile. Note that the tuner’s phase pattern is directly transferred to the matched filter output as expected according to (6.11) and Figure 6.10.

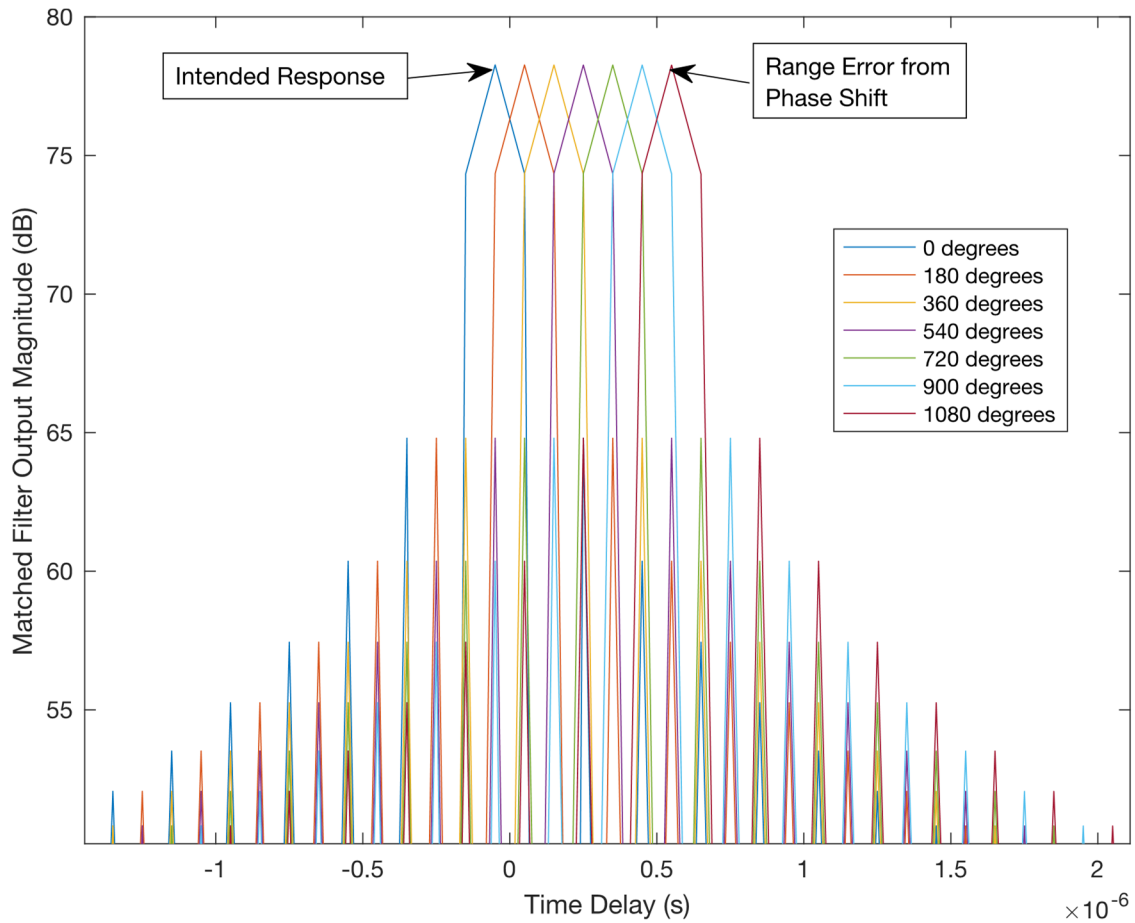


Figure 6.9. Propagation error incurred by tunable component phase shifts from 0 to 1080° during an LFM pulse with a bandwidth of 5 MHz and period of 8192.6 μ s.

Assuming a stationary target and ideal processing, the matched filter response for all pulses within a CPI will be constant. After applying the Fourier transform to each range bin, no frequency variation will be observed, leading to a zero-Doppler target response (Doppler bin peak at 0 Hz and zero elsewhere). However, given the matched

filter response phase variations of Figure 6.11, the target Doppler response will instead take the shape of the Fourier transform of the observed change in the matched filtered output. For a stationary target and slow time-varying adaptive component, the distorted target Doppler response will then be determined by the Fourier transform of the phase variations of the adaptive component. This is illustrated in Figure 6.12 for the phase response of Figure 6.11. Note that the tuner's phase response has caused the target's Doppler response to incorrectly shift away from the 0 Hz Doppler bin, indicated by the vertical line in Figure 6.12. Combined with windowing, this mechanism explains the small Doppler errors encountered in the measurement results of Figure 6.3.

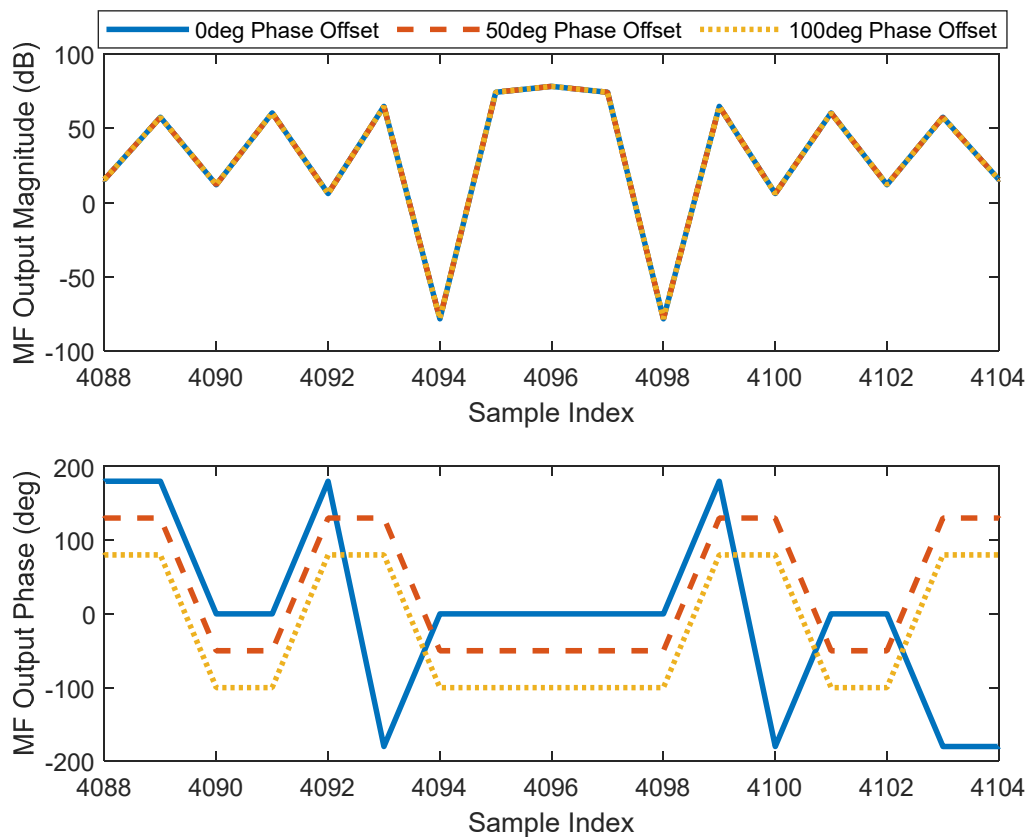


Figure 6.10. Matched filter response for an example LFM pulse with varying constant phase offsets applied to the filtered pulse.

6.5.3 Correction Methods

One approach that can correct for the effects presented in this chapter is the predistortion method of Boyd described in the introduction to this chapter [99]. However, this approach requires advance knowledge of the phase response the tuner will exhibit. Precharacterizing all possible impedance transitions is not feasible because of the vast number of possible transitions (on the order of 10^{12} for the tuners of [25] and [26]). Generating a transition model based on some subset of the possible transitions is also difficult, as the transitions are also affected by the tuner's internal mechanisms, such as the rate of speed of the tuner's internal actuation mechanisms (possibly subject to temperature, orientation, and external environmental forces).

Instead, the impact of these slow phase changes can be mitigated in post-processing after transmission completes. It is possible to generate a per-pulse matched filter definition for each pulse within the CPI using copies of the transmit waveform at the output of the impedance tuner. As this copy is already acquired as part of the performance evaluation required of a cognitive radar in the previous chapters, very few system modifications are necessary. Generating per-pulse matched filters eliminates the effect by incorporating the slow phase transition from impedance tuning in the matched filter definition, removing the offset from the matched filter output. As shown in Figure 6.13, this phase drift vanishes using per-pulse matched filtering, which eliminates the negative impact on range-Doppler processing of impedance tuning, as evidenced by the agreement between the ideal, non-distorted range-Doppler result (blue line) and the distorted CPI processed with per-pulse matched filtering (orange, dashed line).

Note that this technique can result in a time-varying pulse within a given CPI. In practice, the adjustment is minimal to the point of no observable error in the resulting range-Doppler image. However, in more extreme cases, some distortion due to the non-constant CPI may occur. Under this condition, the deconvolution technique applied by Kirk [97] is well suited to correct for this variance in addition to the more significant variations caused by intentional waveform variations arising from dynamic spectrum access.

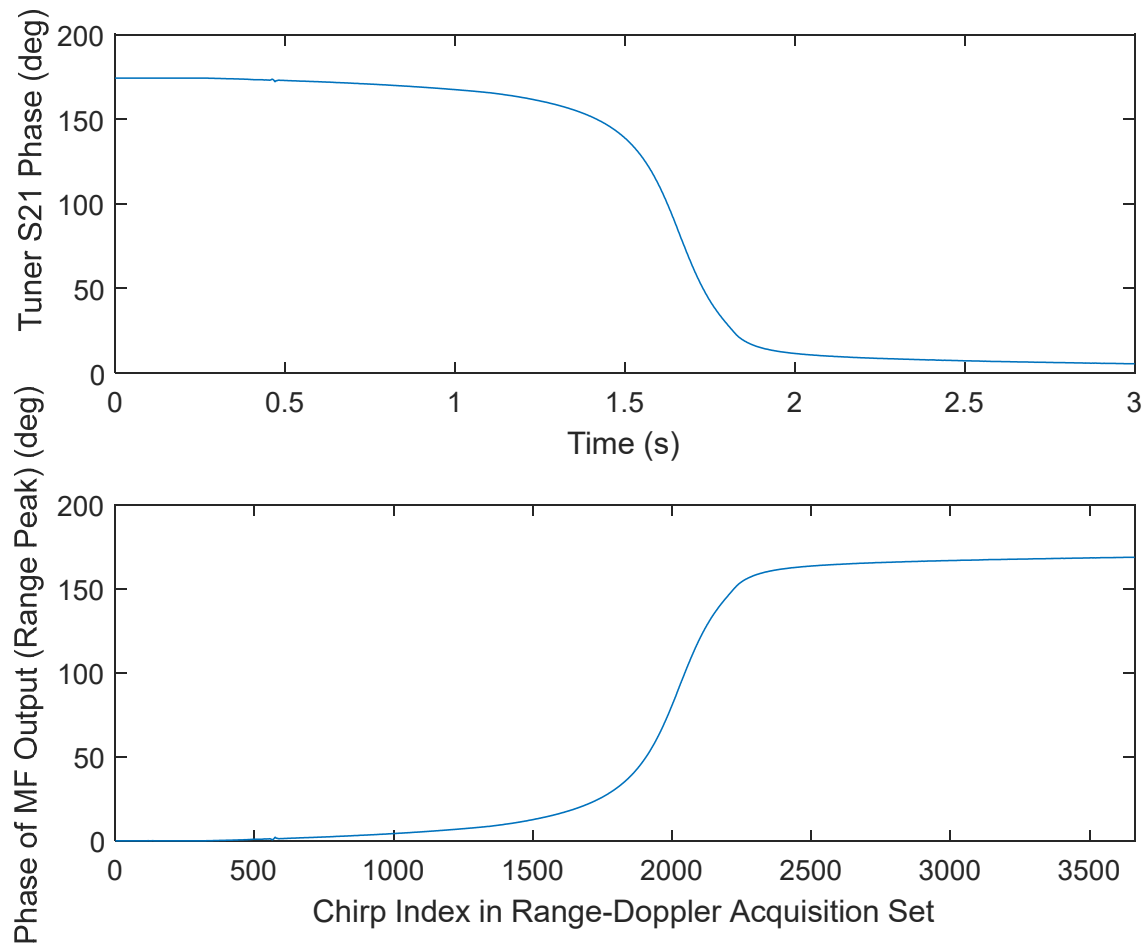


Figure 6.11. Matched filter responses for simulated CPI with measured tuner phase data applied to each waveform sample.

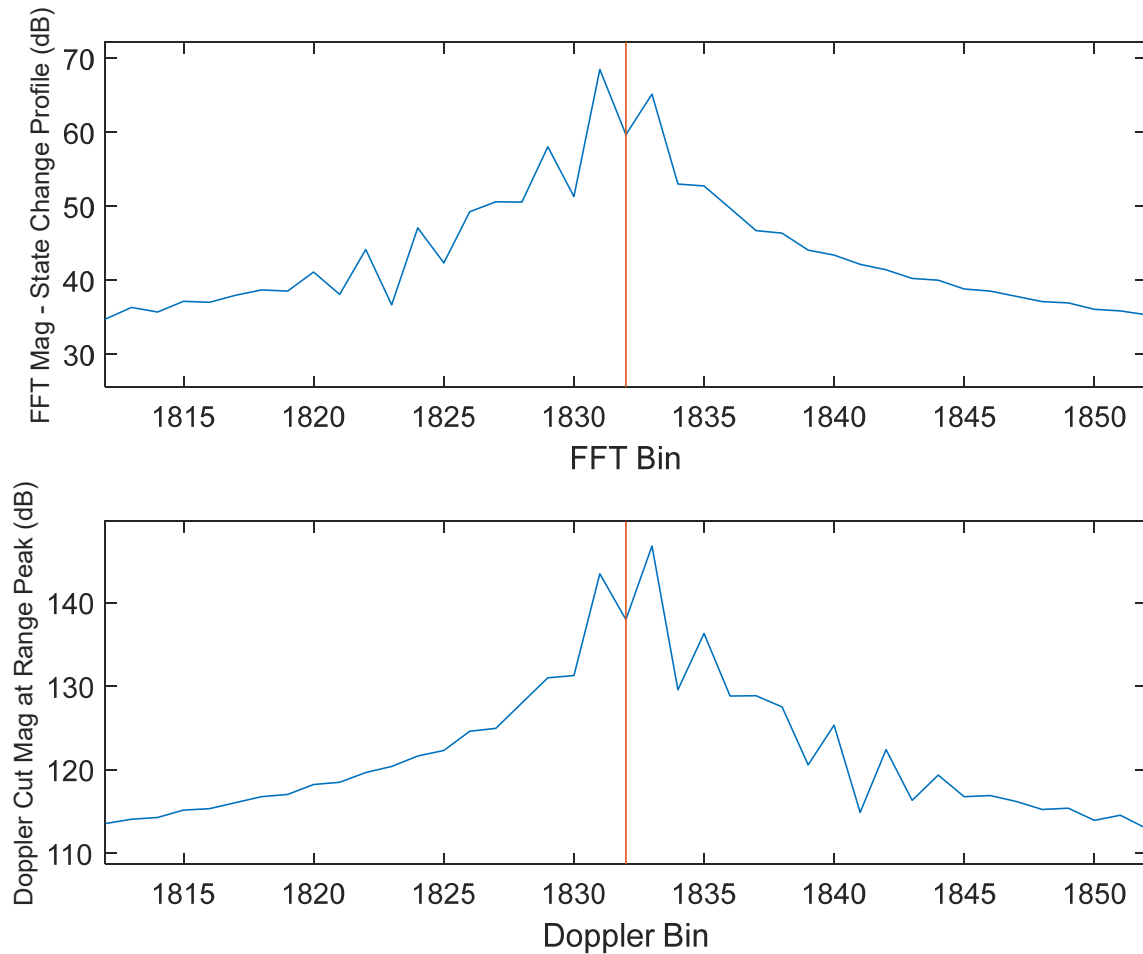


Figure 6.12. Fourier transform of the tuner phase response of Figure 6.11 (top) and the distorted target Doppler response along the peak target range bin (bottom). The 0 Hz Doppler bin is indicated by the vertical line at bin 1832.

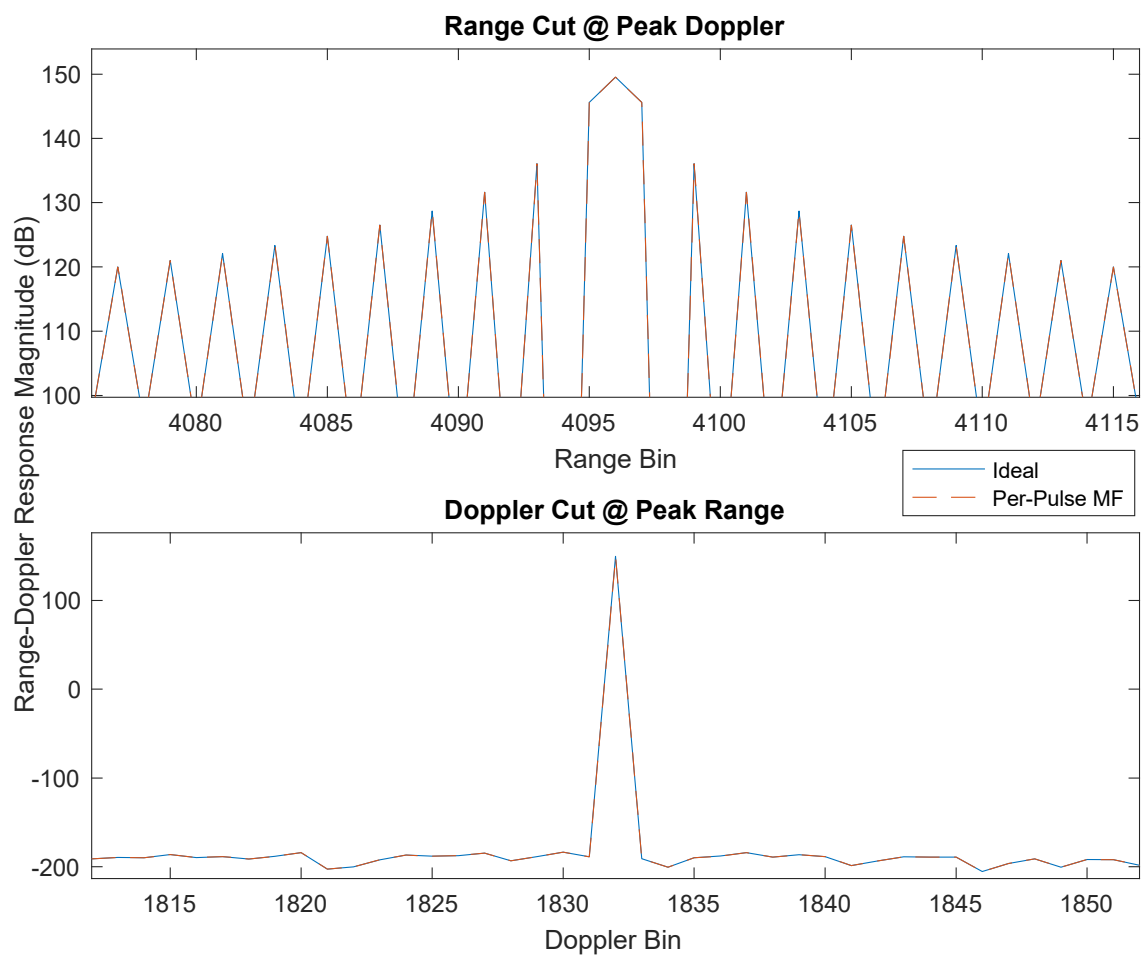


Figure 6.13. Range-Doppler target response (range response on top, Doppler response on bottom) for both an ideal, non-distorted CPI (no tuning) using the regular matched filtering technique (solid blue) and a distorted CPI (mid-tuning) using the per-pulse matched filtering technique of this section (dashed).

CHAPTER SEVEN

Conclusions and Future Work

As the spectral environment continues to become more crowded with the introduction of new technologies, the need for adaptive spectrum usage will only become more critical. While more advanced methods of spectrum allocation and management have arisen to address the increasing congestion, including the FCC's Citizen's Band Radio Service (CBRS) and accompanying Spectrum Access System (SAS), additional degrees of freedom in Drozd's transmission hypercube [32] remain underutilized. Chapter Two has demonstrated how spectral and spatial freedoms can be determined based on knowledge of existing users in the band and location of interest, as well as how to apply these freedoms to adaptively generated radar waveforms given a fixed transmission pattern. Rodriguez-Garcia has built upon the foundation presented in Chapter Two and demonstrated the parallel case of generating a dynamic transmission pattern given a fixed radar waveform, as well as utilizing a dynamic spectral mask to avoid users positioned in directions of interest that cannot otherwise be avoided by spatial adaptation [102]. However, a fully integrated technique that can operate directly upon the spatial-spectral constraint map and jointly optimize the spatial and spectral transmission content remains an open research question. Some variation of the alternating technique of Latham's joint circuit and waveform optimization [103] may prove useful in fully leveraging the information provided by the spatial-spectral constraint map.

Regardless of the method of determining transmission content, adaptive spectrum users operating with high-power transmissions greatly benefit from (if not require) adaptive hardware components to obtain the necessary performance over wide bands of potential operation. The SDR-based measurement techniques of Chapter Three have enabled the use of circuit optimization techniques in real-time applications. Combined with the average performance developments of Chapter Four, real-time circuit optimization of a highly adaptive cognitive radar transmitter has been demonstrated. However, the techniques of Chapter Four can still be improved through the development of a technique that permits grouping similar transmit configurations into interchangeable sets, reducing the number of measurements required per iteration of the optimization algorithm.

Additionally, the introduction of faster tuners, capable of tuning for each individual radar pulse, can enable faster, more direct optimization of each transmit configuration than has been demonstrated in this dissertation. For instance, Calabrese has demonstrated the use of a binary stub tuner capable of optimizing a single transmit configuration in under 35 μs [104]. However, it is important to note that faster tuning alone is not sufficient to address the complications of optimizing adaptive systems described in Chapter Four. As mentioned in Section 4.3.1, optimization requires multiple evaluations of a given transmit configuration; for radar purposes, this requires either optimizing over the course of several PRIs or using an adaptive dummy load to emulate the antenna while optimizing for the next pulse during the radar's dwell time. Unless true per-pulse optimization is a hard requirement, the former option is likely preferred, as it avoids the power inefficiencies of multiple, high-power pseudo-transmissions that are not

actually broadcast. If a tuner is able to tune within the period when the next transmission is determined and when it is transmitted, then it is possible to run multiple optimizations in an interleaved fashion rather than averaging the performance of multiple configurations under one optimization. Given the extremely short, sub-PRI time window available, both the tuning latency and the optimization look-up latency are critical for maintaining responsive adaptive systems. How best to effectively manage the optimization look-up latency for interleaved optimizations is under investigation.

Given the multi-PRI nature of optimization, improving the rate of optimization will eventually rely less on faster tuners and more on reducing the number of performance evaluations, lowering the number of PRIs required for optimization convergence. The load-pull extrapolation technique of Chapter Five presents an incredibly efficient method of performing circuit optimization, frequently converging in seven or fewer pulses. By comparison, this same period permits only two full iterations of a two-dimensional gradient search or a single iteration of the stub tuner algorithm in [104].

However, the existing implementation of the extrapolation optimization still has room for possible improvement. Currently, the load-pull extrapolation technique relies on Smith Chart contours, necessitating the need for tuner characterization. Whether or not image completion can be usefully applied to performance contours in the tuner's fundamental element space (such as the (n_1, n_2) space) remains an unexplored question. If so, the algorithm is ripe for application to configuration grouping in the algorithm of Chapter Four. Meanwhile, the current time required for each image completion remains too great for per-PRI application. In the future, additional algorithm optimization and

alternative hardware platforms designed for accelerating neural network computation could provide significant reductions in processing time to permit extremely fast completions.

Finally, unless operating in the circuit optimization paradigm of evaluating for each pulse with a dummy load, the radar system processing must be able to cope with the effects of the adaptive transmit hardware on the transmission waveforms. While the techniques of Kirk discussed in Section 6.1 work quite well at accounting for intentional changes to transmission by the cognitive radar, the adaptive hardware imparts additional, unanticipated changes on each transmission as the transmission magnitude and phase are altered pulse-to-pulse or mid-pulse. As such, it is highly recommended to use the loopback matched filter definition technique shown in Section 6.5.3 to account for the effects of the transmit hardware. Combined with Kirk's deconvolution method, this permits the use of the adaptation methodologies presented in this dissertation to improve the radar's transmit ability and obtain greater detection range with minimal negligible impact on the radar detection quality.

In summary, this dissertation has presented significant contributions to the state-of-the-art in real-time cognitive radar transmitter optimization. These contributions have significantly lowered the time required to evaluate the performance of a transmit amplifier and have demonstrated the real-time optimization of a cognitive radar transmitter during spectrum sharing operations for the first time. Additionally, this work has addressed how adaptive transmitters can be deployed for practical application by establishing a framework for considering spatial transmission constraints and correcting for distortions encountered in range-Doppler processing as a result of live impedance

tuning. Finally, a basis for future time improvements in real-time circuit optimization has been demonstrated with the load-pull extrapolation technique, which can further reduce the required number of performance evaluations and lower the time required for optimization convergence.

BIBLIOGRAPHY

- [1] J. Genachowshi, "America's Mobile Broadband Future," Address to International CTIA WIRELESS I.T. & Entertainment Convention [Online]. October 2009. Available from: https://hraunfoss.fcc.gov/edocs_public/attachmatch/DOC-293891A1.pdf [Accessed 7 March 2019].
- [2] "Mobile data traffic outlook," *Ericsson Mobility Report Data and Forecasts* [Online]. Available from: <https://www.ericsson.com/en/mobility-report/dataforecasts/mobile-traffic-forecast> [Accessed 7 June 2021].
- [3] Federal Communications Commission, "National Broadband Plan," [Online]. Available from: <https://www.fcc.gov/general/national-broadband-plan> [Accessed 7 March 2019].
- [4] "Use of the 5.850-5.925 GHz Band; Proposed rule," 86 *Federal Register* 83 (3 May 2021), pp. 23323-23340.
- [5] President's Council of Advisors on Science and Technology, "Realizing the Full Potential of Government-Held Spectrum to Spur Economic Growth," July 2012.
- [6] M. McHenry *et al.*, "Spectrum Occupancy Measurements: Republican National Convention, New York City, New York, August 30 - September 3, 2004," [Online]. August 2005. Available from: http://www.sharespectrum.com/wp-content/uploads/4_NSF_NYC_Report.pdf [Accessed 7 March 2019].
- [7] M. McHenry *et al.*, "Spectrum Occupancy Measurements: Chicago, Illinois, November 16 - 18, 2005," [Online]. December 2005. Available from: http://www.sharespectrum.com/wp-content/uploads/NSF_Chicago_2005-11_measurements_v12.pdf [Accessed 7 March 2019].
- [8] M. McHenry *et al.*, "Spectrum Occupancy Measurements: Dublin, Ireland, April 16 - 18, 2007," [Online]. November 2007. Available from: http://www.sharespectrum.com/wp-content/uploads/NSF_Chicago_2005-11_measurements_v12.pdf [Accessed 7 March 2019].
- [9] Q. Zhao and A. Swami, "A Survey of Dynamic Spectrum Access: Signal Processing and Networking Perspectives," *2007 IEEE International Conference on Acoustics, Speech and Signal Processing - ICASSP '07*, 2007, pp. IV-1349-IV-1352, doi: 10.1109/ICASSP.2007.367328.

- [10] H.J. Levin, *The Invisible Resource: Use and Regulation of the Radio Spectrum*, Second Edition, Earthscan, 2011.
- [11] H. Griffiths, "The challenge of spectrum engineering," *2014 11th European Radar Conference*, 2014, pp. 1-4, doi: 10.1109/EuRAD.2014.6991052.
- [12] H. Deng and B. Himed, "Interference Mitigation Processing for Spectrum-Sharing Between Radar and Wireless Communications Systems," in *IEEE Transactions on Aerospace and Electronic Systems*, vol. 49, no. 3, pp. 1911-1919, July 2013, doi: 10.1109/TAES.2013.6558027.
- [13] C. Latham, C. Baylis, L. Cohen, and R. J. Marks, "Dynamic spectral mask construction for radar transmission based on communication receiver locations," *2016 Texas Symposium on Wireless and Microwave Circuits and Systems (WMCs)*, 2016, pp. 1-5, doi: 10.1109/WMCaS.2016.7577484.
- [14] Federal Communications Commission, "Report and Order and Second Further Notice of Proposed Rulemaking in the Matter of Amendment of the Commission's Rules with Regard to Commercial Operations in the 3550-3650 MHz Band," *FCC 15-47*, April 2015.
- [15] National Telecommunications and Information Administration, "RE: Amendment of the Commission's Rules with Regard to Facilitating Shared Use in the 3100-3550 MHz Band (WT Docket No. 19-348)," February 22, 2021.
- [16] B. Badic *et al.*, "The Disruptor: The Millimeter-Wave Spectrum," *Rolling Out 5G: Use Cases, Applications, and Technology Solutions*, Apress, 2016, pp. 111-130.
- [17] P. Nagvanshi, "Analysis of Multiple Antenna Ultra-Wideband and Millimeter Wave Communication Systems," Ph.D. Dissertation, Univ. California – San Diego, 2007.
- [18] A. L. Swindlehurst, E. Ayanoglu, P. Heydari, and F. Capolino, "Millimeter-wave massive MIMO: the next wireless revolution?," in *IEEE Communications Magazine*, vol. 52, no. 9, pp. 56-62, September 2014, doi: 10.1109/MCOM.2014.6894453.
- [19] R. Cai, Q. Chen, X. Peng, and D. Liu, "Spatial Sharing Algorithm in mmWave WPANs with Interference Sense Beamforming Mechanism," *MILCOM 2013 - 2013 IEEE Military Communications Conference*, 2013, pp. 163-168, doi: 10.1109/MILCOM.2013.37.

- [20] M. Di Renzo, H. Haas, A. Ghayeb, S. Sugiura, and L. Hanzo, "Spatial Modulation for Generalized MIMO: Challenges, Opportunities, and Implementation," in *Proceedings of the IEEE*, vol. 102, no. 1, pp. 56-103, Jan. 2014, doi: 10.1109/JPROC.2013.2287851.
- [21] C. Baylis *et al.*, "Circuit optimization algorithms for real-time spectrum sharing between radar and communications," *2016 IEEE Radar Conference (RadarConf)*, 2016, pp. 1-4, doi: 10.1109/RADAR.2016.7485065.
- [22] Z. Hays *et al.*, "Fast amplifier PAE optimization using resonant frequency interval halving with an evanescent-mode cavity tuner," *2017 Texas Symposium on Wireless and Microwave Circuits and Systems (WMCs)*, 2017, pp. 1-3, doi: 10.1109/WMCaS.2017.8070702.
- [23] L. Hays *et al.*, "Direct Tuning of Cavity Position Numbers for Circuit Optimization Using an Evanescent-Mode Cavity Tuner Designed for Reconfigurable Radar Transmitters" *USNC-URSI National Radio Science Meeting*, January 2018, Boulder, Colorado.
- [24] A. Dockendorf *et al.*, "Fast Optimization Algorithm for Evanescent-Mode Cavity Tuner Optimization and Timing Reduction in Software-Defined Radar Implementation," in *IEEE Transactions on Aerospace and Electronic Systems*, vol. 56, no. 4, pp. 2762-2778, Aug. 2020, doi: 10.1109/TAES.2020.2981234.
- [25] A. Semnani, M. Abu Khater, Y. Wu, and D. Peroulis, "An Electronically Tunable High-Power Impedance Tuner With Integrated Closed-Loop Control," in *IEEE Microwave and Wireless Components Letters*, vol. 27, no. 8, pp. 754-756, Aug. 2017, doi: 10.1109/LMWC.2017.2723949.
- [26] A. Semnani, G.S. Shaffer, M.D. Sinanis, and D. Peroulis, "High-Power Impedance Tuner Utilising Substrate-Integrated Evanescent-Mode Cavity Technology and External Linear Actuators," *IET Microwaves, Antennas & Propagation*, Vol. 13, No. 12, 2019, pp. 2067-2072.
- [27] P. Roblin, S. J. Doo, X. Cui, G. H. Jessen, D. Chaillot, and J. Strahler, "New Ultra-fast Real-time Active Load-pull Measurements for High Speed RF Power Amplifier Design," *2007 IEEE/MTT-S International Microwave Symposium*, 2007, pp. 1493-1496, doi: 10.1109/MWSYM.2007.380536.
- [28] G. Tendürüs, A. Ç. Yapıcı, and E. Çağlar, "A low cost measurement setup for measuring ACPR of OFDM signal," *2018 26th Signal Processing and Communications Applications Conference (SIU)*, 2018, pp. 1-4, doi: 10.1109/SIU.2018.8404469.

- [29] T. Jordbru, H. Idsøe, L. R. Cenkeramaddi, B. Beferull-Lozano, and M. Hamid, "Radio measurements on a customized software defined radio module: A case study of energy detection spectrum sensing," *2017 IEEE International Instrumentation and Measurement Technology Conference (I2MTC)*, 2017, pp. 1-6, doi: 10.1109/I2MTC.2017.7969681.
- [30] B. H. Kirk, A. F. Martone, K. D. Sherbondy, and R. M. Narayanan, "Performance Analysis of Pulse-Agile SDRadar with Hardware Accelerated Processing," *2020 IEEE International Radar Conference (RADAR)*, Washington, DC, USA, 2020, pp. 117-122, doi: 10.1109/RADAR42522.2020.9114561.
- [31] A. Egbert, C. Latham, C. Baylis, and R. J. Marks, "Multi-dimensional coexistence: Using a spatial-spectral mask for spectrum sharing in directional radar and communication," *2018 Texas Symposium on Wireless and Microwave Circuits and Systems (WMCs)*, 2018, pp. 1-6, doi: 10.1109/WMCaS.2018.8400641.
- [32] A. L. Drozd, C. K. Mohan, P. K. Varshney, and D. D. Werner, "Multiobjective joint optimization and frequency diversity for efficient utilization of the RF transmission hyperspace," *2004 International Waveform Diversity & Design Conference*, 2004, pp. 1-7, doi: 10.1109/IWDDC.2004.8317549.
- [33] D. Eustice, C. Baylis, L. Cohen, and R. J. Marks, "Waveform synthesis via alternating projections with ambiguity function, peak-to-average power ratio, and spectrum requirements," *2016 IEEE Radio and Wireless Symposium (RWS)*, 2016, pp. 190-192, doi: 10.1109/RWS.2016.7444401.
- [34] A. Egbert, B. H. Kirk, C. Baylis, A. Martone, and R. J. Marks, "Fast Software-Defined Radio-based System Performance Evaluation for Real-time Adaptive RF Systems," *2020 95th ARFTG Microwave Measurement Conference (ARFTG)*, 2020, pp. 1-4, doi: 10.1109/ARFTG47271.2020.9241369.
- [35] C. Andrich, J. Bauer, A. Ihlow, N. Beuster, and G. D. Galdo, "Comparison of Software-Defined Radios for Performance Evaluation of High Precision Clocks," *2018 IEEE International Symposium on Precision Clock Synchronization for Measurement, Control, and Communication (ISPCS)*, 2018, pp. 1-6, doi: 10.1109/ISPCS.2018.8543073.
- [36] A. Wolke, "Calculating RF Power from IQ Samples," Tektronix Blog, [Online]. Available from: <https://www.tek.com/blog/calculating-rf-power-iq-samples> [Accessed 26 March 2020].
- [37] M. Fellows, C. Baylis, L. Cohen and R. J. Marks II, "Real-time load impedance optimization for radar spectral mask compliance and power efficiency," in *IEEE Transactions on Aerospace and Electronic Systems*, vol. 51, no. 1, pp. 591-599, January 2015, doi: 10.1109/TAES.2014.130825.

- [38] M. Fellows, J. Barlow, C. Baylis, J. Barkate, and R. J. Marks, "Designing power amplifiers for spectral compliance using spectral mask load-pull measurements," *2015 IEEE Topical Conference on Power Amplifiers for Wireless and Radio Applications (PAWR)*, 2015, pp. 1-3, doi: 10.1109/PAWR.2015.7139199.
- [39] S. W. Ellingson, "Correcting I-Q Imbalance in Direct Conversion Receivers," Argus Technical and Scientific Documents, [Online]. Available from: <https://www.faculty.ece.vt.edu/swe/argus/iqbal.pdf> [Accessed 26 March 2020].
- [40] A. Egbert, A. Goad, C. Baylis, R. J. Marks, and A. Martone, "Detecting Potential Performance Improvements in Cognitive Radar Systems," *2021 IEEE Radar Conference (RadarConf21)*, 2021, pp. 1-5, doi: 10.1109/RadarConf2147009.2021.9455339.
- [41] A. Egbert *et al.*, "Continuous Real-Time Circuit Reconfiguration to Maximize Average Output Power in Cognitive Radar Transmitters," accepted to *IEEE Transactions on Aerospace and Electronic Systems*, July 2021.
- [42] "White House and DOD Announce Additional Mid-Band Spectrum Available for 5G by the end of the Summer," United States Department of Defense, [Online]. Available from: <https://www.defense.gov/Newsroom/Releases/Release/Article/2307275/white-house-and-dod-announce-additional-mid-band-spectrum-available-for-5g-by-t/> [Accessed 12 December 2020].
- [43] Martone, A.F. "Cognitive Radar Demystified," *URSI Bulletin*, no. 350, September 2014, pp. 10-22.
- [44] S. Haykin, "Cognitive radar: a way of the future," in *IEEE Signal Processing Magazine*, vol. 23, no. 1, pp. 30-40, Jan. 2006, doi: 10.1109/MSP.2006.1593335.
- [45] H. Griffiths *et al.*, "Radar Spectrum Engineering and Management: Technical and Regulatory Issues," in *Proceedings of the IEEE*, vol. 103, no. 1, pp. 85-102, Jan. 2015, doi: 10.1109/JPROC.2014.2365517.
- [46] B. H. Kirk, K. A. Gallagher, J. W. Owen, R. M. Narayanan, A. F. Martone, and K. D. Sherbondy, "Cognitive software defined radar: A reactive approach to RFI avoidance," *2018 IEEE Radar Conference (RadarConf18)*, Oklahoma City, OK, 2018, pp. 0630-0635, doi: 10.1109/RADAR.2018.8378632.
- [47] B. H. Kirk *et al.*, "Cognitive Software-Defined Radar: Evaluation of Target Detection with RFI Avoidance," *2019 IEEE Radar Conference (RadarConf)*, Boston, MA, USA, 2019, pp. 1-6, doi: 10.1109/RADAR.2019.8835498.

- [48] B. H. Kirk, R. M. Narayanan, K. A. Gallagher, A. F. Martone, and K. D. Sherbondy, "Avoidance of Time-Varying Radio Frequency Interference With Software-Defined Cognitive Radar," in *IEEE Transactions on Aerospace and Electronic Systems*, vol. 55, no. 3, pp. 1090-1107, June 2019, doi: 10.1109/TAES.2018.2886614.
- [49] G. E. Smith *et al.*, "Experiments with cognitive radar," in *IEEE Aerospace and Electronic Systems Magazine*, vol. 31, no. 12, pp. 34-46, December 2016, doi: 10.1109/MAES.2016.150215.
- [50] A. F. Martone, K. I. Ranney, K. Sherbondy, K. A. Gallagher, and S. D. Blunt, "Spectrum Allocation for Noncooperative Radar Coexistence," in *IEEE Transactions on Aerospace and Electronic Systems*, vol. 54, no. 1, pp. 90-105, Feb. 2018, doi: 10.1109/TAES.2017.2735659.
- [51] A. Aubry, A. De Maio, Y. Huang, M. Piezzo, and A. Farina, "A new radar waveform design algorithm with improved feasibility for spectral coexistence," in *IEEE Transactions on Aerospace and Electronic Systems*, vol. 51, no. 2, pp. 1029-1038, April 2015, doi: 10.1109/TAES.2014.140093.
- [52] E. Selvi, R. M. Buehrer, A. Martone, and K. Sherbondy, "On the use of Markov Decision Processes in cognitive radar: An application to target tracking," *2018 IEEE Radar Conference (RadarConf18)*, 2018, pp. 0537-0542, doi: 10.1109/RADAR.2018.8378616.
- [53] J. A. Kovarskiy, B. H. Kirk, A. F. Martone, R. M. Narayanan, and K. D. Sherbondy, "Evaluation of Real-Time Predictive Spectrum Sharing for Cognitive Radar," in *IEEE Transactions on Aerospace and Electronic Systems*, vol. 57, no. 1, pp. 690-705, Feb. 2021, doi: 10.1109/TAES.2020.3031766.
- [54] J. F. Sevic, R. Baeten, G. Simpson, and M. B. Steer, "Automated Large-Signal Load-Pull Characterization of Adjacent-Channel Power Ratio for Digital Wireless Communication Systems," *46th ARFTG Conference Digest*, 1995, pp. 64-70, doi: 10.1109/ARFTG.1995.327134.
- [55] C. Latham, A. Egbert, C. Baylis, L. Cohen, and R. J. Marks, "Joint Radar Amplifier Circuit and Waveform Optimization for Ambiguity Function, Power-Added Efficiency, and Spectral Compliance," in *IEEE Transactions on Aerospace and Electronic Systems*, vol. 55, no. 3, pp. 1190-1199, June 2019, doi: 10.1109/TAES.2019.2909725.
- [56] H.W. Bode, "*Network Analysis and Feedback Amplifier Design*, Van Nostrand, 1945.

- [57] R.M. Fano, "Theoretical Limitations on the Broad-Band Matching of Arbitrary Impedances," *Journal of the Franklin Institute*, Vol. 249, January 1950, pp. 57-83, and February 1950, pp. 139-154.
- [58] J. Roessler *et al.*, "Enhancing Frequency-Agile Radar Range over a Broad Operating Bandwidth with Reconfigurable Transmitter Amplifier Matching Networks," *2021 IEEE Radar Conference (RadarConf21)*, 2021, pp. 1-5, doi: 10.1109/RadarConf2147009.2021.9455307.
- [59] S. Perlow, "New Algorithms for the Automated Microwave Tuner Test System," *RCA Review*, Vol. 46, pp. 341-355, September 1985.
- [60] A.P. de Hek, "A Novel Fast Search Algorithm for an Active Load-Pull Measurement System," *GaAs Symposium*, 1998.
- [61] Dongjiang Qiao, R. Molfino, S. M. Lardizabal, B. Pillans, P. M. Asbeck, and G. Jerinic, "An intelligently controlled RF power amplifier with a reconfigurable MEMS-varactor tuner," in *IEEE Transactions on Microwave Theory and Techniques*, vol. 53, no. 3, pp. 1089-1095, March 2005, doi: 10.1109/TMTT.2005.843495.
- [62] G. Berghoff, E. Bergeault, B. Huyart, and L. Jallet, "Automated characterization of HF power transistors by source-pull and multiharmonic load-pull measurements based on six-port techniques," in *IEEE Transactions on Microwave Theory and Techniques*, vol. 46, no. 12, pp. 2068-2073, Dec. 1998, doi: 10.1109/22.739284.
- [63] J. Barkate, A. Tsatsoulas, C. Baylis, L. Cohen, and R. J. Marks, "Comparison of multidimensional circuit optimization techniques for real-time transmitter use," *2016 Texas Symposium on Wireless and Microwave Circuits and Systems (WMCS)*, 2016, pp. 1-7, doi: 10.1109/WMCaS.2016.7577485.
- [64] A. Dockendorf, E. Langley, C. Baylis, A. Martone, K. Gallagher, and E. Viveiros, "Faster Frequency-Agile Reconfiguration of a High-Power Cavity Tuner for Cognitive Radar Using Previous Search Results," *2019 IEEE Radio and Wireless Symposium (RWS)*, 2019, pp. 1-3, doi: 10.1109/RWS.2019.8714494.
- [65] J. Alcalá-Medel *et al.*, "Fast Frequency-Agile Real-Time Optimization of High-Power Tuning Network for Cognitive Radar Applications," *2019 IEEE MTT-S International Microwave Symposium (IMS)*, 2019, pp. 1466-1469, doi: 10.1109/MWSYM.2019.8701008.
- [66] A. Mokhtari, S. Shahrampour, A. Jadbabaie, and A. Ribeiro, "Online optimization in dynamic environments: Improved regret rates for strongly convex problems," *2016 IEEE 55th Conference on Decision and Control (CDC)*, Las Vegas, NV, 2016, pp. 7195-7201, doi: 10.1109/CDC.2016.7799379.

- [67] R. Dixit, A. S. Bedi, R. Tripathi, and K. Rajawat, "Time Varying optimization via Inexact Proximal Online Gradient Descent," *2018 52nd Asilomar Conference on Signals, Systems, and Computers*, Pacific Grove, CA, USA, 2018, pp. 759-763, doi: 10.1109/ACSSC.2018.8645323.
- [68] A. Goad, A. Egbert, A. Dockendorf, C. Baylis, A. Martone, and R. J. Marks, "Optimizing Transmitter Amplifier Load Impedance for Tuning Performance in a Metacognition-Guided, Spectrum Sharing Radar," *2020 IEEE International Radar Conference (RADAR)*, Washington, DC, USA, 2020, pp. 73-76, doi: 10.1109/RADAR42522.2020.9114669.
- [69] K. Miettinen, *Nonlinear Multiobjective Optimization*. New York, New York, USA: Springer, 1998, part II, ch. 1, pp. 61-63.
- [70] L. McBride and K. Narendra, "Optimization of time-varying systems," in *IEEE Transactions on Automatic Control*, vol. 10, no. 3, pp. 289-294, July 1965, doi: 10.1109/TAC.1965.1098164.
- [71] A. F. Martone, K. I. Ranney, K. Sherbondy, K. A. Gallagher, and S. D. Blunt, "Spectrum Allocation for Noncooperative Radar Coexistence," in *IEEE Transactions on Aerospace and Electronic Systems*, vol. 54, no. 1, pp. 90-105, Feb. 2018, doi: 10.1109/TAES.2017.2735659.
- [72] C. Baylis, L. Dunleavy, S. Lardizabal, R.J. Marks II, and A. Rodriguez, "Efficient Optimization Using Experimental Queries: A Peak-Search Algorithm for Efficient Load-Pull Measurements," *Journal of Advanced Computational Intelligence and Intelligent Informatics*, Vol. 15, No. 1, January 2011, pp. 13-20.
- [73] S. Kullback, and R. Leibler, "On information and sufficiency," *The Annals of Mathematical Statistics*, 22(1), pp.79-86.
- [74] Hyndman, R. and Koehler, A., 2006, "Another look at measures of forecast accuracy," *International Journal of Forecasting*, 22(4), pp.679-688.
- [75] Y. Rubner, C. Tomasi and L. J. Guibas, "A metric for distributions with applications to image databases," *Sixth International Conference on Computer Vision (IEEE Cat. No.98CH36271)*, 1998, pp. 59-66, doi: 10.1109/ICCV.1998.710701.
- [76] M. Allman, V. Paxson, and E. Blanton, *TCP Congestion Control*, RFC 5681, September 2009.
- [77] J. Kurose and K. Ross, "Principles of Congestion Control," in *Computer Networking: A Top-Down Approach*. Hoboken, NJ, USA: Pearson, 2017, ch. 3, sec. 6, pp. 261-269.

- [78] B.T. Polyak, "Some methods of speeding up the convergence of iteration methods," in *USSR Computational Mathematics and Mathematical Physics*, vol. 4, no 5, pp. 1–17, 1964.
- [79] Y.E. Nesterov, "A Method for Solving the Convex Programming Problem with Convergence Rate $O(1/k^2)$," in *Soviet Mathematics Doklady*, vol 27, no. 2, pp. 372-376, 1983.
- [80] I. Sutskever, J. Martens, G. Dahl, and G. Hinton, "On the importance of initialization and momentum in deep learning," in *Proc. Int. Conf. Mach. Learn.*, Atlanta, GA, USA, 2013, pp. 1139–1147.
- [81] L. Madden, S. Becker, and E. Dall'Anese, "Bounds for the Tracking Error of First-Order Online Optimization Methods," in *Journal of Optimization Theory and Applications*, 2021.
- [82] A. Egbert, A. Martone, C. Baylis, and R. J. Marks, "Partial Load-Pull Extrapolation Using Deep Image Completion," *2020 IEEE Texas Symposium on Wireless and Microwave Circuits and Systems (WMCS)*, 2020, pp. 1-5, doi: 10.1109/WMCS49442.2020.9172302.
- [83] A. Howard, "How to Setup and Run Load Pull Simulations: The Basics," *YouTube*, Jan. 27, 2015 [Video file]. Available from: <https://www.youtube.com/watch?v=34N-r5rPSzU> [Accessed 30 July, 2020].
- [84] I. Gulrajani, F. Ahmed, M. Arjovsky, V. Dumoulin, and A. Courville, "Improved training of Wasserstein GANs," in *Proceedings of the 31st International Conference on Neural Information Processing Systems (NIPS'17)*, 2017, pp. 5769–5779.
- [85] J. M. Ede and R. Beanland, "Partial Scanning Transmission Electron Microscopy with Deep Learning," in *Scientific Reports*, vol. X, no. 8332, May 2020, doi: 10.1038/s41598-020.65261.0.
- [86] G. Avolio, A. Raffo, M. Marchetti, G. Bosi, V. Vadalà, and G. Vannini, "GaN FET Load-Pull Data in Circuit Simulators: a Comparative Study," *2019 14th European Microwave Integrated Circuits Conference (EuMIC)*, 2019, pp. 80-83, doi: 10.23919/EuMIC.2019.8909451.
- [87] H. Kabir, L. Zhang, M. Yu, P. H. Aaen, J. Wood, and Q. Zhang, "Smart Modeling of Microwave Devices," in *IEEE Microwave Magazine*, vol. 11, no. 3, pp. 105-118, May 2010, doi: 10.1109/MMM.2010.936079.
- [88] I. Goodfellow *et al.*, "Generative Adversarial Nets," *Neural Information Processing Systems 2014 (NIPS'14)*, Montreal, 2014.

- [89] M. Arjovsky, S. Chintala, and L. Bottou, "Wasserstein Generative Adversarial Networks," in *Proceedings of the 34th International Conference on Machine Learning*, vol. 70, pp. 214-223, 2017.
- [90] D. Szurko, "TensorFlow 2.0 WGAN-GP," 2019. [Online]. Available from: <https://github.com/drewszurko/tensorflow-WGAN-GP>.
- [91] A. Bäuerle, C. van Onzenoodt, and T. Ropinski, "Net2Vis – A Visual Grammar for Automatically Generating Publication-Tailored CNN Architecture Visualizations," in *IEEE Transactions on Visualization and Computer Graphics*, vol. 27, no. 6, pp. 2980-2991, 1 June 2021, doi: 10.1109/TVCG.2021.3057483.
- [92] G. Gonzalez, *Microwave Transistor Amplifiers*, Second Edition, Prentice-Hall, 1997.
- [93] H. Li *et al.*, "Data Preprocessing" in *Fuzzy Neural Intelligent Systems: Mathematical Foundation and the Applications in Engineering*, CRC Press, 2000, ch. 15.
- [94] B. Amos, "Image Completion with Deep Learning in TensorFlow," 2016. [Online]. Available from: <http://bamos.github.io/2016/08/09/deep-completion/>.
- [95] D. P. Kingma and J. Ba, "Adam: A Method for Stochastic Optimization," *3rd International Conference for Learning Representations*, San Diego, 2015. [Online]. arXiv:1412.6980.
- [96] A. Egbert *et al.*, "The Effect of Real-Time Radar Transmitter Amplifier Impedance Tuning on Range and Doppler Detection Accuracy," *2019 IEEE Texas Symposium on Wireless and Microwave Circuits and Systems (WMCS)*, Waco, TX, USA, 2019, pp. 1-4, doi: 10.1109/WMCaS.2019.8732549.
- [97] B. Kirk, A. Martone, K. Sherbondy, and R. Narayanan, "Mitigation of target distortion in pulse-agile sensors via Richardson–Lucy deconvolution," in *Electronics Letters*, vol. 55, no. 23, pp. 1249-1252, November 2019, doi: 10.1049/el.2019.2650.
- [98] K. Van Caekenberghe, "RF MEMS on the radar," in *IEEE Microwave Magazine*, vol. 10, no. 6, pp. 99-116, Oct. 2009, doi: 10.1109/MMM.2009.933596.
- [99] G. D. Boyd and F. Heismann, "Tunable acoustooptic reflection filters in LiNbO₃ without a Doppler shift," in *Journal of Lightwave Technology*, vol. 7, no. 4, pp. 625-631, April 1989, doi: 10.1109/50.19088.

- [100] M.A. Zeidan, G. Banerjee, and J.A. Abraham, "Asynchronous Measurement of Transient Phase-Shift Resulting From RF Receiver State-Change," *IEEE Transactions on Circuits and Systems*, Vol. 60, No. 10, October 2013, pp 2740-2751.
- [101] C. Cook and M. Bernfeld, *Radar Signals*, 1967, pp. 385.
- [102] P. Rodriguez-Garcia, A. Egbert, C. Baylis, and R. J. Marks, "Spatial-Spectral Coexistence: Dual Approach to Search Radar Transmission Synthesis Using a Spatial Mask," *2019 IEEE Texas Symposium on Wireless and Microwave Circuits and Systems (WMCS)*, 2019, pp. 1-6, doi: 10.1109/WMCaS.2019.8732509.
- [103] C. Latham, A. Egbert, C. Baylis, L. Cohen, and R. J. Marks, "Joint Radar Amplifier Circuit and Waveform Optimization for Ambiguity Function, Power-Added Efficiency, and Spectral Compliance," in *IEEE Transactions on Aerospace and Electronic Systems*, vol. 55, no. 3, pp. 1190-1199, June 2019, doi: 10.1109/TAES.2019.2909725.
- [104] C. Calabrese, A. Dockendorf, A. Egbert, B. Herrera, C. Baylis, and R. J. Marks, "Fast Switched-Stub Impedance Tuner Reconfiguration for Frequency and Beam Agile Radar and Electronic Warfare Applications," *2020 IEEE International Radar Conference (RADAR)*, 2020, pp. 94-98, doi: 10.1109/RADAR42522.2020.9114834.